ISSN 1000-9620

海洋通报

Marine Science Bulletin

NATIONAL MARINE DATD AND
INFORMATION SERVICE OF CHINA

2015
Volume 17
Number 1

MARINE SCIENCE BULLETIN

Vol. 17 No. 1 May 2015

CONTENTS

Time series analysis of red tide's disaster characteristics in China seas ..... XU Hai-long et al. (01)

Influence of soil liquefaction on the vertical mechanical behavior of submarine pipeline under the wave loading ..... YOU Qi et al. (11)

Vertical distribution of the Kuroshio velocity in the Pollution Nagasaki section and its formative mechanism .....DENG Li-jing et al. (26)

Focal mechanism solution statistics of seismic tsunami sources ..... HOU Jing-ming et al. (40)

Research on the influence of ocean temperature on XCTD profiler single-mode fiber transmission ..... ZHENG Yu et al. (50)

Pollution status and potential ecological risk assessment in the surface sediments of the Yellow River estuary ..... ZHANG Ya-nan et al. (61)

A Study of impact of the reclamation and artificial island projects on tidal currents and sediment concentration in radial sand ridge field of the Soutth Yellow Sea .....ZHAO Qiang et al. (71)

Digital Ocean Information Framework of China and its application in the international marine cooperation..... YU Ting et al. (86)

LIBRARY
Pacific Islands Fisheries Science Center
NOAA Fisheries
Honolulu, Hawai'i

NOAA CENTRAL LIBRARY
JAN 27 2017
WITHDRAWN
National Oceanic & Atmospheric Administration
U.S. Dept of Commerce

Time series analysis of red tide's disaster characteristics in China seas

XU Hai-long[1, 2], GU De-xian[3], ZHANG Wen-liang[4], GAO Qi[1], QIAO Xue-tao[1]

1. *Key Laboratory of Aqua-ecology and Aquaculture, Tianjin Agricultural University, Tianjin* 300384, *China;*
2. *College of Marine Science, Shanghai Ocean University, Shanghai* 201306, *China;*
3. *Tianjin Fishery Institute, Tianjin* 300221, *China;*
4. *Department of Preparing of Tianjin Bohai Oceanic Monitoring & Surveillance Management Base, Tianjin Oceanic Administration, Tianjin* 300457, *China*

Abstract: The annual frequency of red tides from 1977 to 2012 and the monthly frequency of red tides from 2001 to 2012 in China seas were used to establish the time series of red tide annual frequency and monthly frequency, respectively. The annual frequency fit well with time segments revealed by piecewise linear regression analysis. The seasonal maximum of monthly frequency was in May (-18.22), and the stochastic volatility tended to increase gradually with time series, with peak values occurring from May to July. Holt exponential smoothing and Holt-winter exponential smoothing were used to predict red tide annual and monthly frequencies, which revealed that the annual frequency of red tides would rise slowly by one time from 2013 to 2020, and that red tides would mainly occur from May to July in 2013-2016 with a peak value of about 25 times in May.

Keywords: China seas, red tide, frequency, time series

Red tide, a naturally occurring phenomenon, is the water discoloration caused by the sudden bloom or rapid accumulation of some phytoplankton, protozoa, or bacteria under favorable environmental conditions [1]. It has been more frequent in more ocean regions with more damages, due to social and economic development, marine environment deterioration, global warming, and enhanced human activity in the ocean. Approximately 60% of the red tide events lead to direct economic losses in the aquaculture or fishing; half of them are catastrophic and cause 80% or more losses. Although the exact mechanism of red tides remains unclear[1, 2], many studies have been carried out to investigate the physical and chemical factors during red tides' occurrence, development, and termination[3-8], the changes in environmental parameters [9-17], and the establishment of prediction model of red tides using SeaWiFs visible light[18] or MODIS wave band[19, 20].

Received on Oct. 15, 2014

Corresponding author: beiji80@163.com

However, no studies on red tide time series analysis and prediction in China seas targeting red tide frequency have been reported. In this study, the frequency of red tides in China seas was investigated to quantitatively analyze the time series characteristics. Specifically, the annual frequency of red tides in 1977-2012 and the monthly frequency in 2001-2012 were analyzed through the time series method, followed by the prediction of 2013-2020's annual frequency and 2013-2016's monthly frequency.

1 Materials and methods

Red tide frequency data were collected from the 1977 - 2012 annual red tide statistical bulletins and the 1989 - 2012 State Oceanic Administration "China Marine Disaster Bulletin", and they are analyzed to establish the time series of red tide annual and monthly frequencies in China seas.

According to the trends of changes in red tide frequencies during 1977 - 2012, the relationship between the red tide annual frequency and years was established by using the piecewise linear fitting method; the monthly frequency of red tides from 2001 to 2012 was analyzed for the trend, seasonal and irregular components; two models were established based on the annual and monthly frequencies of red tides using the Holt exponential smoothing method and the Holt-Winters exponential smoothing method[21] to predict annual frequency from 2013 to 2020 and monthly frequency from 2013 to 2016, respectively, with data processing and plotting being done using "TTR" R (i386 3.0.1) package[22] and EXCEL.

2 Results and analysis

2.1 Trends of red tide annual frequency

Time series analysis of the changes in red tides from 1977 to 2012 revealed that the annual frequency was in an overall upward trend with 119 red tides at one higher peak in 2003 (the highest value on record) and with the other peak in 1992 for 50 red tides (Fig. 1). Based on the trend of changes, the annual frequencies were divided into five stages: one slowly increasing stage (1977 - 1988), two rapidly increasing stages (1989 - 1992 and 2000 - 2003), and two slowly decreasing stages (1993 - 1999, 2004 - 2012). All five stages were individually analyzed to obtain each stage's regression relationship between the frequency and time, and all three increasing stages showed good equation fitting results ($R>0.89$).

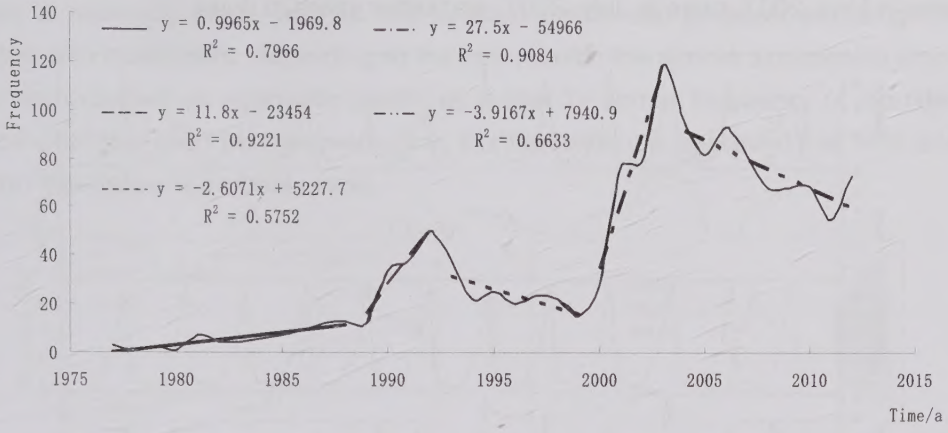

Fig. 1 Annual frequency of red tides from 1977 to 2012

The deviation characteristics of annual frequency of the two stages, 1989 - 1999 and 2000 - 2012, were compared. As shown in Fig. 2, these two stages had similar change trends although the values were not same. Both had a 3-year increasing period with the middle plateau, and the decreasing period was rapid at the beginning but then slowed down with volatility.

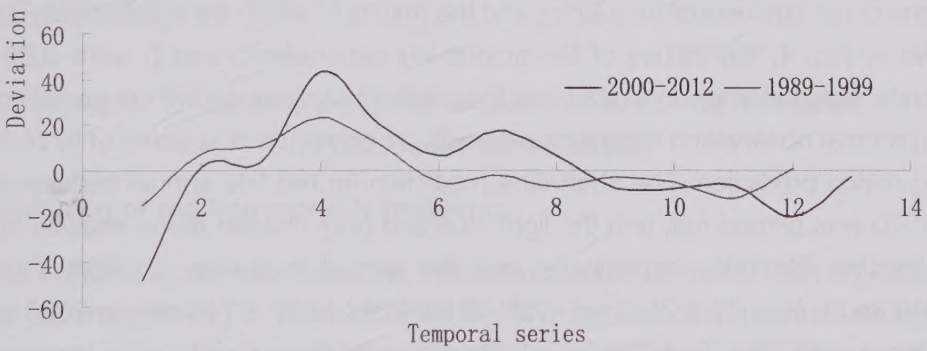

Fig. 2 Deviation of red tide frequency during 1989 - 1999 and 2000 - 2012

2.2 Patterns of red tide monthly frequency

The red tide monthly frequency was a seasonal time series, and its constituent components from 2001 to 2012 were separated into a trend component, a seasonal component and an irregular or a random component. As shown in Fig. 3, the trending component gradually decreased from 10 times in August, 2003 to 4.5 times in September, 2011; the maximum value and minimum value in seasonal component occurred in May (about 18.22 times) and in December (about -6.76 times), respectively; the random component was gradually increasing, and the peak fluctuations occurred from May to July,

with once in May, 2007, once in July, 2007, and other years in June.

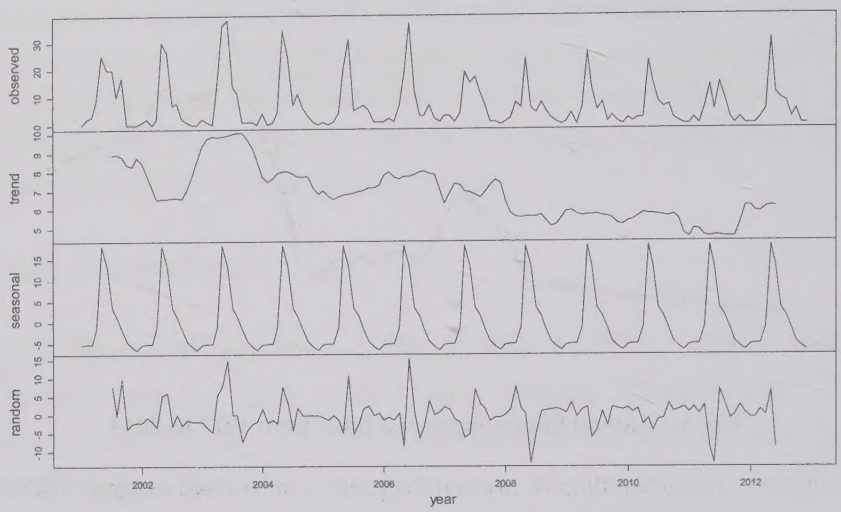

Fig. 3 Compositions of the monthly frequency of red tides during 2001 - 2012

2.3 Prediction of red tide annual frequency

Holt exponential smoothing method was used for sampling periods and short-term predictions of red tide annual frequency, and the results of which were statistically analyzed. As shown in Fig. 4, the values of the smoothing parameter α and β were 0.93 and 0, respectively, which strongly indicated that the prediction values during the sampling period were just normal observation variations, and with an error sum of squares of 6774 from the sampling period prediction. The short-time prediction for red tide annual frequency during 2013 - 2020 was carried out, and the light blue and gray shaded areas showed 80% and 95% prediction intervals, respectively, and the annual frequency showed a gradually increasing trend, from 73 ± 28 times (95% CI) in 2013 to 80 ± 74 times in 2020 with one time increase each year. To determine whether the predictive model can be improved upon, in other words, if there aren't correlations between forecast errors for successive predictions, a correlogram of the in-sample forecast errors for lags of 1 - 20 was obtained. It was seen from the sample correlogram that the autocorrelation at lag 7 and 10 was just touching the significance bounds. To test whether non-zero correlations at lags 1 - 20 were significant evidence, a Ljung-Box test was carried out. Here the p-value of Ljung-Box test is 0.6, so there is lack of evidence to draw a conclusion that the forecast errors at lags 1-20 are non-zero autocorrelations in the in-sample. To reassure that the predictive model cannot be improved upon, we also plot a histogram of the in-sample forecast errors with an overlaid normal curve that has the same standard deviation and mean zero. The figure shows that the forecast errors are roughly focused on zero and the distribution is more or less normally distributed. Although the plot seems to be slightly skewed to a normal curve,

the skew is relatively small, and so the forecast errors can be seen as being normally distributed with mean zero. According to the test results, the simple exponential smoothing method has provided an adequate predictive model for annual frequency of red tides, and the model probably can't be improved upon. Furthermore, it is approved that 80% and 95% prediction intervals are probably valid.

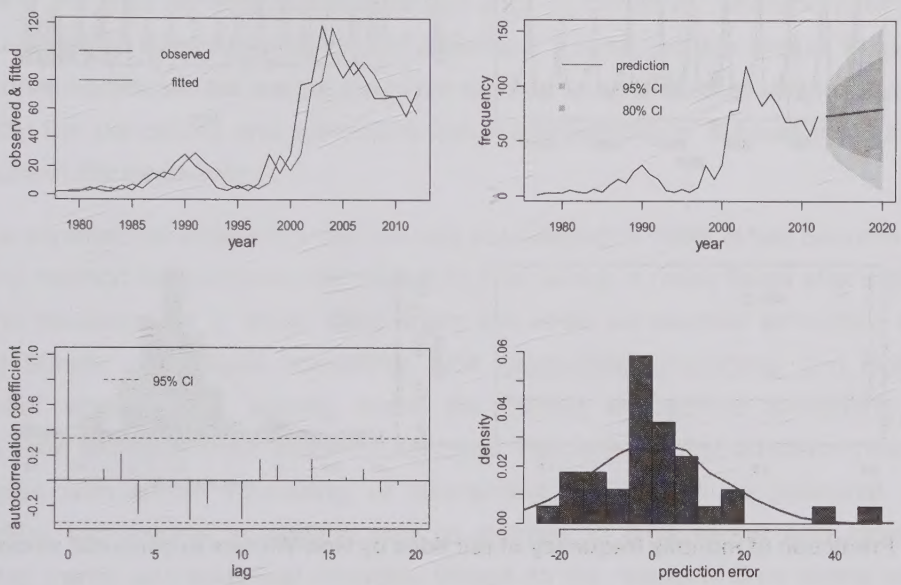

Fig. 4 Prediction of the annual frequency of red tides by the method of Holt Exponential Smoothing

2.4 Prediction of red tide monthly frequency

Holt-Winter exponential smoothing method was used to predict monthly frequency of red tides. As shown in Fig. 5, the estimated values of the smoothing parameter alpha, beta and gamma in predictive model with an error sum of squares of 3 085.52 were 0.039, 0.090, and 0.457, respectively. Both alpha and beta were smaller than 0.1, indicating that the estimate of the level at the current time point and slopes of trend component were rarely affected by recently happened events. This model predicted that 2013 - 2016's red tides would still mainly occur from May to July, peaking in May with about 25 times; December had the least red tides, almost none. The same as above mentioned, all of correlogram of the in-sample forecast errors for lags 1-20, a Ljung-Box test and a histogram of the in-sample forecast errors with an overlaid normal curve were obtained. The figure shows that the autocorrelations at lag 11 and 13 for the in-sample forecast errors exceed and touch the significance bounds for lags 1 - 20, respectively, and the p-value for Ljung-Box test is 0.362, and the forecast errors are normally distributed with mean zero according to the histogram of forecast errors. So, Holt-Winters exponential

smoothing method provides a suitable predictive model for the monthly frequency of red tide, which cannot be improved upon, and upon which the prediction is based, and it is probably valid.

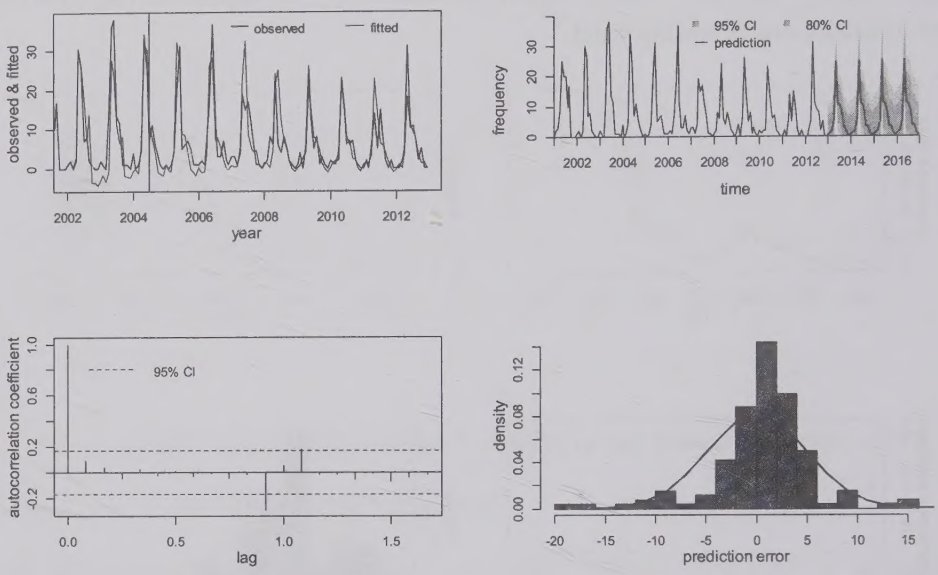

Fig. 5 Prediction of monthly frequency of red tides by Holt-Winters exponential smoothing

3 Discussion

The records of modern red tides in China started in 1933 with a *noctiluca scintillans* red tide that occurred in the former Zhejiang Fisheries Experimental Field (Zhenhai to Taizhou, Shipu, and nearby waters), and red tides in China were not continuously recorded until 1977. The records from then to 1990s still lacked the integrity and systematicness due to lagging research [1, 2], causing difficulties for the analysis of this period's red tide annual frequency and the accurate prediction of future events in this study. The deviations of red tide frequencies during the period of 1989-1999 and that of 2000 - 2012 were compared, which revealed that red tides were first gradually decreasing from 1989 - 1999, followed by rapid increases from 2000 - 2003. However, from 2000 - 2012, the lowest annual frequency in 2011 was followed by increases in 2012, indicating a trend of rapid increases in 2013 based on the similar deviation patterns of these two periods. This predicted annual frequency was similar to that during 2013 - 2020 by the Holt exponential smoothing method, although the Holt method predicted a relatively gradual increase (one time more annually). The prediction difference between two methods may be caused by the fact that the Holt method used the data of 1977 - 2012, which included data before 1990s when the information lacked integrity and systemicness, and predictions based on two periods'

deviations still need improvements in basic information quantity and prediction theory and method. As far as red tides is concerned, especially in the sea, there are many affected factors with unclear mechanisms so far, and even different factors may have different weights under different conditions, which makes it almost impossible to find a method to predict red tides perfectly. However, human activity is relatively periodic during a given phase, and red tides are apparently seasonal (Fig. 3), therefore, deviation patterns which can be used as an alternative method to effectively predict red tide annual frequency are feasible on the premise that more studies are needed to optimize such methods, especially to quantify the periodicity and determine the characteristics of fluctuations and intrinsic parameters in the periodicity.

The exponential smoothing method was established in 1958. It has become the most commonly method to predict events related to time series in many fields after statisticians' study and development in detail. Now, there are three exponential smoothing methods, including Simple exponential smoothing, Holt exponential smoothing, and Holt-Winters exponential smoothing[21]. Among them, the Simple exponential smoothing requires constant time series without seasonal changes; Holt exponential smoothing can handle time series with either increasing or decreasing trends but no seasonal changes; Holt-Winters exponential smoothing can be applied to time series with increasing or decreasing trends and seasonal changes. Based on the results of time series analysis of red tide annual frequency during 1977 - 2012 and that during 2001 - 2012, annual frequency during 1977-2012 had five stages with either increasing or decreasing trends without the seasonality, and monthly frequency during 2001-2012 had apparent seasonality, with a first increasing but later decreasing trend from month to month. Therefore, Holt exponential smoothing and Holt-Winters exponential smoothing were used for time series prediction of the annual and monthly frequencies, respectively.

The Holt exponential smoothing method was determined by two parameters: α was used to estimate the level at current time point, while β was used to estimate the slope of current time's trend component; both parameters were between 0 - 1; when they were closer to 0, most recent observation events became less important for the prediction of future values. In this study, β was determined as 0, which indicated that the annual frequency of red tides was unlikely to suddenly increase or decrease. This might be due to the relatively high ratio of 1990s' red tide data to the total data. The test of prediction errors revealed that they did not have non-zero autocorrelation in the lags of 1 - 20 but were normally distributed with zero means. It indicated that the prediction model of red tide annual frequency based on the Holt exponential smoothing method could not be further optimized.

The prediction using the Holt-Winters exponential smoothing method depended on three parameters: α, β, and γ corresponded to the level of the current time, the slope of the trend component, and the slope of the seasonal component, respectively. When Holt-Winters exponential smoothing was used to analyze the monthly frequency of 2001-2012's red tides, the values of α and β were both relatively low, indicating that the estimated values at sampling time points were mainly based on historical observations, with constant slopes of the trending parts in the whole time series; the value of γ was close to 0.5, indicating the estimation of the seasonality was based on the equal integration of early data and recent observation data. The predicted peak seasonal values by Holt-Winters exponential smoothing were almost the same as the observed values, while the monthly frequency's random fluctuation composition showed a gradually increasing trend, indicating that the effects of random factors on red tide monthly occurrence frequency were gradually increasing, probably due to increased random factors as a result of rapid development of the economy near the sea.

From the test of red tide monthly frequency prediction errors, the p value of Ljung-Box test was 0.362, indicating insufficient evidence to conclude the non-zero autocorrelation of prediction errors in the lags of 1 - 20. Therefore, it was likely to be an accident that 1/20 of the first 20 lags (the 11^{th}) exceeded the 95% significant bounds. Although the prediction errors showed a right-skew normal distribution in the density plot, the right deviation was relatively small. Therefore, the prediction errors could still be considered as mean zero value normal distribution, indicating that the Holt-Winters exponential smoothing method was an appropriate prediction model for red tide monthly frequency.

4 Conclusions

Red Tide is one of the world's top three offshore pollution problems and one of the major marine disasters in offshore area of China. In this study, the Holt exponential smoothing method and Holt-Winters exponential smoothing method were used to establish prediction models for red tide annual frequency during 1977 - 2012 in China seas and the monthly frequency during 2001 - 2012, respectively. Based on these models, we predicted that rapid increases or decreases in the annual frequency were unlikely, with an annual increase of only one time from 2013 (73 times) to 2020 (80 times). The effects of random factors on monthly frequency would be gradually increasing, with May-July of 2013 - 2016 as the high frequent period, among which, May is as the peak month (25 times), and December as the least month (close to zero). More detailed investigations should be carried out in the future due to China's highly spanning latitude and longitude, dramatically

different environments, and significantly different red tide algae compositions.

Acknowledgements

This work was financially supported by the Tianjin Marine Science and Technology Project (KJXH2011-05), local colleges and universities in Shanghai liberal arts academic programme (B5201120003).

References

[1] Zhao D Z, Zhao L, Zhang F S. Type of formation,distribution and temporal trend of red tides occurred in the China Sea [J]. Marine Environmental Science, 2003, 22(3): 1 - 5.

[2] Qi Y Z, Chu J H, Huang Y H. Environmental element impact on triggering off chattonella marina bloom [J]. Marine Science Bulletin, 1993, 12(2): 30 - 34.

[3] Lin F A, Lu X W, Luo H, et al. History , status and characteristics of red tide in Bohai Sea [J]. Marine Environmental Science, 2008, 27 (Z2): 1 - 5.

[4] Lin Z H, Liang S H. Study and forecasting on red tide caused by marine physical factors [J]. Marine Environmental Science, 2002, 21(2): 1 - 5.

[5] Liu Y H, Song X K, Jin Y, et al. Occurrence characteristics of akashiwo sanguinea bloom caused by land source rainwater [J]. Acta Ecologica Sinica, 2012,32(15): 4 836 - 4 843.

[6] Tu J B, Zhang Q F, Xu Y S, et al. Preliminary analysis of Phaeocystis globosa Scherffel red tide in Tianjin coastal sea areas of Bohai Bay [J]. Marine Science Bulletin, 2011, 30(3): 334 - 337.

[7] Wang S F, Tang D L. Analysis of harmful algal blooms associated with ocean environments in the South China Sea [J]. Marine Science Bulletin, 2010, 29(5): 577 - 583.

[8] Wei G Q, Wang H, Cai W X, et al. 10-Year restrospective analysis on the harmful algal blooms in the pearl river estuary [J]. Marine Science Bulletin, 2012, 31(4): 466 - 474.

[9] Chen G B. Automatic monitoring of Akashiwo sanguinea HAB Tong'an Bay, Xiamen [J]. Marine Environmental Science, 2012, 31(3): 391 - 394.

[10] Jiao X Y. Primary study on the transparency as a forecast parameter of red tide [J]. Marine Environmental Science, 2001, 20(1): 27 - 31.

[11] Li H, Gu S M. Approach to red tide prediction on RBF neural network. Computer Engineering and Applications [J]. Computer Engineering and Applications, 2012, 48(1): 228 - 230, 248.

[12] Ma Y M, Gao J Y, Wang Q H. Forecast model for red tide on artificial neural network [J]. Marine Forecasts, 2007, 24 (1): 38 - 44.

[13] Qi Y Z, Huang W J, Qiu X H. Population Dynamic Time Series Models of Noctiluca Scintillans in Da-Pong Bay South China Sea [J]. Journal of Jinan University, 1991, 12(3): 96 - 103.

[14] Wang Z F, Zhang Q, Lv H Y, et al. The Simple Method of Dissolved Oxygen about Red Tide

Forecast in the Changjiang Estuary [J]. Acta Oceanologica Sinica, 2000, 22(4): 125 - 129.

[15] Yang J Q, Luo X X, Ding D W, et al. A Preliminary Study on Artificial Neural Network Method for Predicting Red Tide [J]. Advances in Marine Science, 2003, 21 (3): 318 - 324.

[16] Zhang J F, Yu J L, Pang H L, et al. Forecast of Red Tide in the South China Sea by Using the Variation Trend of Hydrological and Meteorological Factors [J]. Marine Forecasts, 2006, 23(1): 9 - 19.

[17] Zhang L X, Zhao M, Jiang X S. The change trend of happened frequency and the R/S forecast of frequently happened year for red tide in China [J]. Marine Science Bulletin 2010, 29(1): 72 - 77.

[18] Ahn Y H, Shanmugam P. Detecting the red tide algal blooms from satellite ocean color observations in optically complex Northeast-Asia Coastal Waters [J]. Remote Sensing of Environment, 2006, (103): 419 - 437.

[19] Hu C M, Cannizzaro J, Carder K L, et al. Remote detection of Trichodesmium blooms in optically complex coastal waters: Examples with MODIS full-spectral data [J]. Remote Sensing of Environment, 2010, 114(9): 2 048 - 2 058.

[20] Kim Y, Byun Y. Detection of Cochlodinium polykrikoides red tide based on two-stage filtering using MODIS data [J]. Desalination, 2009, 249(3): 1 171 - 1 179.

[21] Liu L M. Application of Exponential Smoothing in Time Series Analysis [J]. Journal of Shenyang Normal University (Natural Science), 2009, 27(4): 416 - 418.

[22] Joshua U. TTR: Technical Trading Rules. R package version 0.22 - 0. http://CRAN.R-project.org /package = TTR. 2013.

基于时间序列的海洋赤潮灾害特征分析

徐海龙[1, 2]，谷德贤[3]，张文亮[4]，高 启[1]，乔秀亭[1]

（1. 天津农学院水产科学系 天津市水产生态及养殖重点实验室，天津 300384；2. 上海海洋大学海洋科学学院，上海 201306；3. 天津市水产研究所，天津 300221；4. 天津市海洋局 渤海海洋监测监视管理基地筹备处，天津 300457）

摘 要：以 1977-2012 年中国海赤潮的年发生频率及 2001-2012 年赤潮的月发生频率数据资料为基础，建立赤潮事件的年发生频率和月发生频率时间序列。赤潮的年发生频率与时间的分段回归拟合效果较好，月频率的季节性最大值在 5 月（约 18.22），随机波动的大小随时间序列逐步增加，波动峰值主要出现在 5-7 月。利用 Holt 指数平滑法和 Holt-Winter 指数平滑法分别对赤潮事件的年发生频率和月发生频率进行预测，结果表明 2013-2020 年赤潮的年发生频率呈年平均增加 1 次的缓慢趋势上升，2013-2016 年 5-7 月份为赤潮高发期，峰值出现在 5 月，基本稳定在 25 次左右。

关键词：中国海；赤潮；频次；时间序列

Influence of soil liquefaction on the vertical mechanical behavior of submarine pipeline under the wave loading

YOU Qi [1, 2], XU Guo-hui [1, 2*], WANG Xiu-hai [2], LV Chu-xiu [1, 2], LIU Zhi-qin [1, 2], MENG Qing-sheng [2]

1. *Key Laboratory of Marine Environment and Ecology, Ministry of Education, Qingdao* 266100, *Shandong province, China;*

2. *College of Environmental Science and Engineering, Ocean University of China, Qingdao* 266100, *Shandong province, China*

Abstract: In this paper, the influence of soil liquefaction on the vertical pressure of submarine pipeline was investigated under the wave loading through the wave flume test. The experiment was set with the same waves on the liquefied seabed and unliquefied seabed respectively, and the current pipeline vertical pressure was measured with the pressure transducers installed on the two opposite directions (i.e., straight up and straight down) at the same cross-section of the pipeline. The results showed that when the seabed was unliquefied, the two pressure curves varied periodically and overlapped completely, reaching the maximum and minimum at the same time respectively, and the resultant pressure fluctuated within a limited range. However, when the seabed was liquefied, the two pressure curves varied periodically, but they did not overlap completely. They did not reach the maximum (minimum) value at the same time either, and the resultant pressure fluctuated within a wider range. The experiment showed that the submarine stood higher resultant pressure in the vertical direction when the seabed was liquefied, which may cause the frequent sinking and floatation of the pipeline, leading to its fatigue damage.

Keywords: silty soil; liquefaction; the vertical pressure of pipeline; phase lag; flume experiment

1 Introduction

The ocean is abundant in fossil oil and natural gas. As the lifeline of marine oil and gas resources, submarine pipelines are of vital importance in the liquid and gas

Received on Jul. 26, 2014

*Corresponding author: xuguohui@ouc.edu.cn

transportation. Submarine pipelines are usually buried under the seabed, however, in the complex marine environment, and it may fail from time to time and cause huge losses. To prevent such accidents, it is essential to investigate the pressure conditions of pipelines buried under the seabed well.

For this purpose, many scholars at home and abroad have carried out some related researches. For example, Jothi Shankar et al. (1985) studied the wave force coefficients through the experiments on large diameter submarine pipelines. Sumer et al. (1991) also focused on the influence of plane boundary on the force coefficients. Anandkumar et al. (1995) had investigated the submarine pressure in different directions of the buried pipelines under different waves. YAN Shu-wang et al. (1998) had investigated the impact of water content of soil on the stability of the buried pipeline by the shaking table model experiment. B.M. Sumer et al. (1999) (2001) had researched the sinking depths of pipelines with different shapes, blocks and balls in the liquefied soil under the wave loading. And he also studied the scour process and the self-burial mechanism of pipelines, analyzed the influence of the KC value, shields parameters and the buried depth of pipeline on self-buried flushing depth. ZHU Ji-wei et al. (2001) had discussed the movement pattern of the buried pipeline when soil liquefaction occurred through the shaking table experiment in this paper. T. C. The et al. (2003) had investigated the changes of the pore pressure before and after the soil was liquefied by the flume experiment. And the influence of the pipeline specific gravity, the parameters of liquefied soil as well as the wave condition on the movement of pipeline in the liquefied bed were analyzed. Vijaya Kumar et al. (2003) researched how the consistency index of the soil affected the uplift forces around submarine pipeline in clayey soil. XU Ji-shang et al. (2010) had studied the scour depth and the pressure on the pipeline under the action of regular waves in different beds such as silty soil and sandy soil. GAO Fu-ping et al. (2012) had studied the stability of the pipeline on sloping seabed with a specially-designed experiment device. While ZHANG Zhi-yong et al. (2012) had conducted numerical simulation and model test to study the variation of pressure distribution and wave pressure on the pipeline with a spoiler added on the top when the pipeline was perpendicular to the direction of wave propagation. LIU Cheng-xiang et al. (2012) had investigated the angle α formed by the pipeline axis and the direction of wave propagation, and its impact on the vertical pressure of the pipeline under different flow rates and wave loading. ZHOU Xiang-lian et al. (2013)(2014) had investigated the effect of the bed permeability, the soil shear modulus and the burial depth of the pipeline on the vertical pressure, the pore pressure and the liquefaction potential of the soil in the cross-anisotropic seabed with the method of numerical simulation.

Among the above mentioned researches, some are about the stability of the buried

pipelines, while some surround the movement rules of pipelines in liquefied soil. However, the research about the pressure distribution along buried pipelines in liquefied soil (especially the liquefied silty soil) has not been done yet. The Yellow River Delta area is mainly covered by silty soil. And the oil pipelines in the region are usually buried underground as a routine procedure. However, despite the huge cost on the safe operation, accidents still occur here and there. For instance, in November 2003, the cable in the Cheng-Dao Oil Field failed suddenly. The shallow profile survey afterwards showed that the disturbance depth caused by seabed liquefaction amounted to more than 4 m. This accident had obvious correlation with soil liquefaction. Therefore, it is of great significance to explore the influence of soil liquefaction on the mechanical behavior of the pipeline.

2 Overview

Four soil pressure transducers were divided into two pairs and each pair was installed in reverse directions. The transducers were bound with the pipeline (d=40 cm) and installed in the groove. Both ends of the pipeline were fixed. The axis of the pipeline was 20 cm from the interface of water and soil. Two sets of the transducers were fitted to A and B respectively. The location of the pipeline is shown in Fig. 2.

After fixing the probe, the silty soil with a water content of 30-35% was poured into the groove to prepare the experimental seabed. Water was added into the system until it reached a level of 30 cm above the top of the bed. The system was left aside for 10 days of consolidation in the preparation for the test. There were two parallel trials in this experiment, i.e., Trial A and Trial B. Trial A adopted PVC pipelines while Trial B used steel pipelines. Apart from the difference in the pipe material, two trails were identical in the method and procedure.

Each trial contained two stages. In the first stage, waves of 11 cm and 14 cm in height were exerted to the seabed respectively. Wave parameters are shown in Tab. 1. The loading of the waves lasted for 1h, during which the current pressure values on the probe were collected by the acquisition system with a sampling frequency of 100 Hz. After the first stage, the bottom of the bed was struck with a steel hammer repeatedly to stir the soil till it was liquefied. In the second stage, the same waves as those in the first stage were applied to the liquefied bed with the same duration of 1 h. The pressure parameters from the two probes were collected, and at the same time, the record of liquefaction depth (h) was noted down.

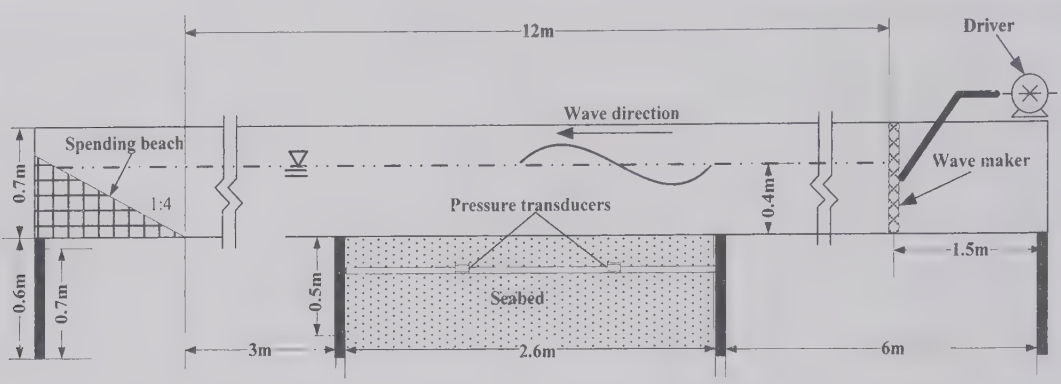

Fig. 1 Setup of the experimental flume

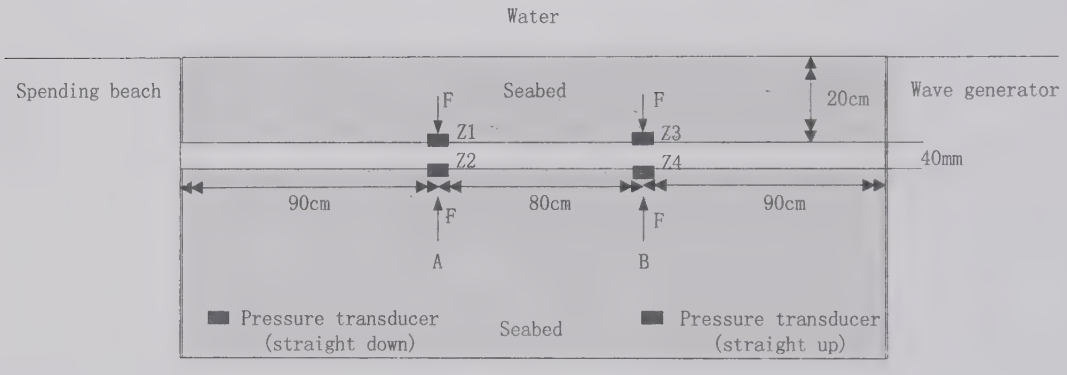

Fig. 2 Arrangement of pressure transducers

Tab. 1 Test conditions

Condition	Wave parameters	Duration
The seabed is not disturbed	H=11 cm	1h
	H=14 cm	1h
The seabed is disturbed	H=11 cm	1h
	H=14 cm	1h

3 Results and analysis

3.1 Analysis of phase differences of the pipeline pressure

According to the experimental records, current pressure figures of Trial A and Trial B were drawn showing the current pressure of the probe in different conditions. Specific conditions are shown below, where H represents the wave height and h represents the depth of liquefaction at which the probe was located. In each figure, the horizontal axis represents the relative time, and the vertical axis represents the pressure.

The experiment A with the PVC pipe is as the following:

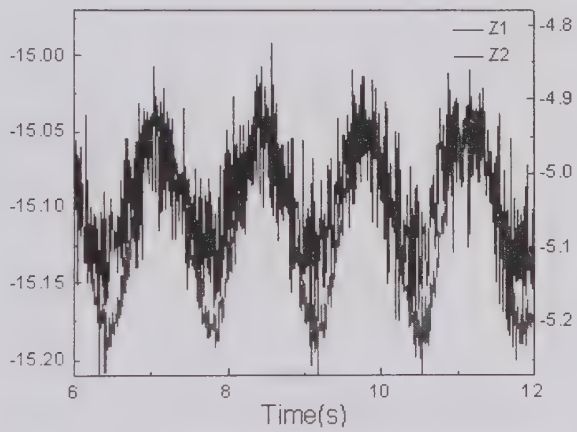

(a) The pressure of transducers Z1 and Z2, H=11 cm, and the soil is not liquefied.

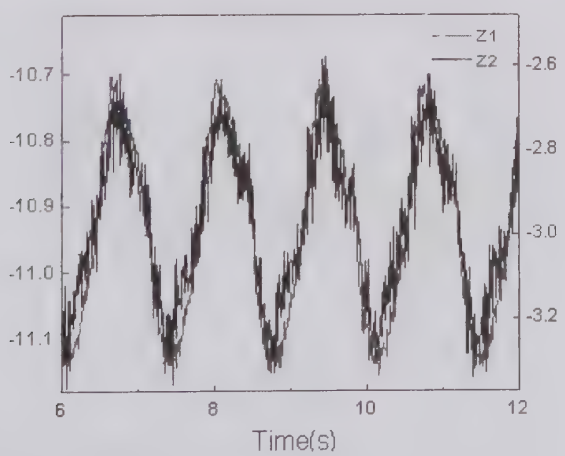

(b) The pressure of transducers Z1 and Z2, H=11 cm, h=26 cm

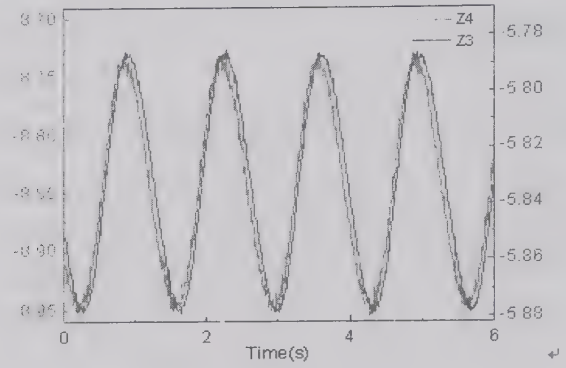

(c) The pressure of transducers Z3 and Z4, H=11 cm, and the soil is not liquefied.

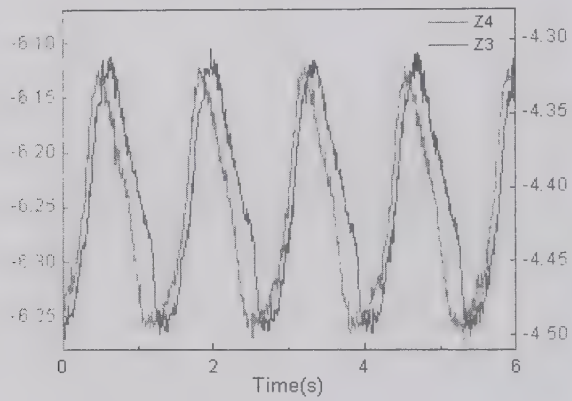

(d) The pressure of transducers Z3 and Z4, H=11 cm, h=29 cm

Fig. 3 The pressure of transducers at different stages in test A , H=11 cm

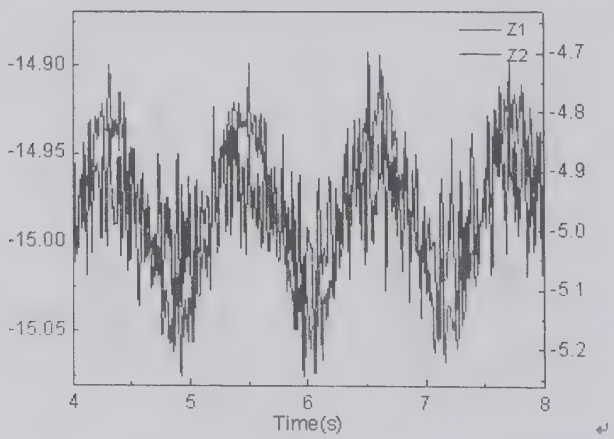

(a) The pressure of transducers Z1 and Z2, H=14 cm, and the soil is unliquefied

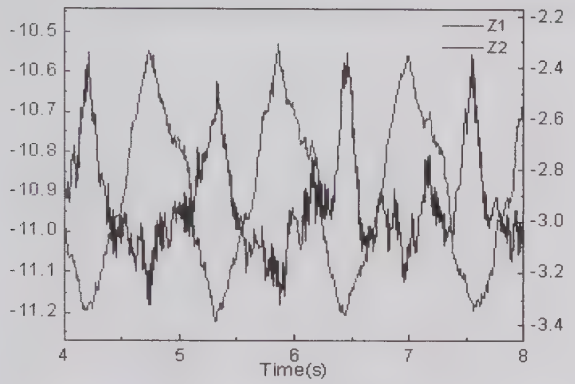

(b) The pressure of transducers Z1 and Z2, H=14 cm, h=37 cm

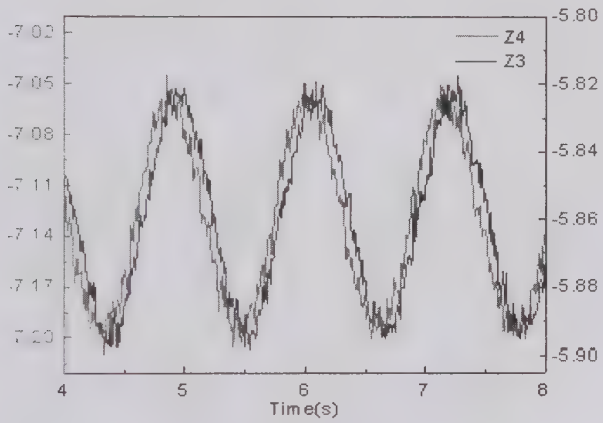

(c) The pressure of transducers Z3 and Z4, H=14 cm, and the soil is unliquefied

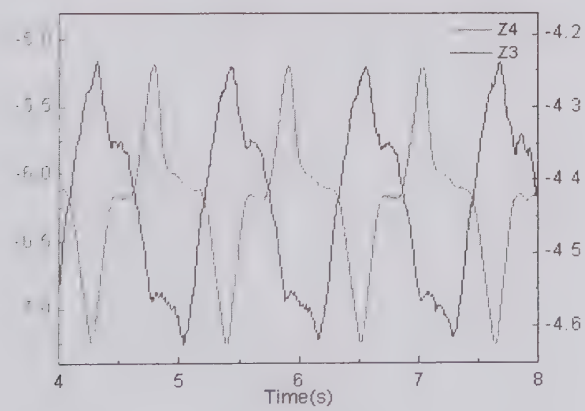

(d) The pressure of transducers Z3 and Z4, H=14 cm, h=36 cm

Fig. 4 The pressure of transducers at different stages in test A , H=14 cm

The experiment B with the steel pipe is as the following:

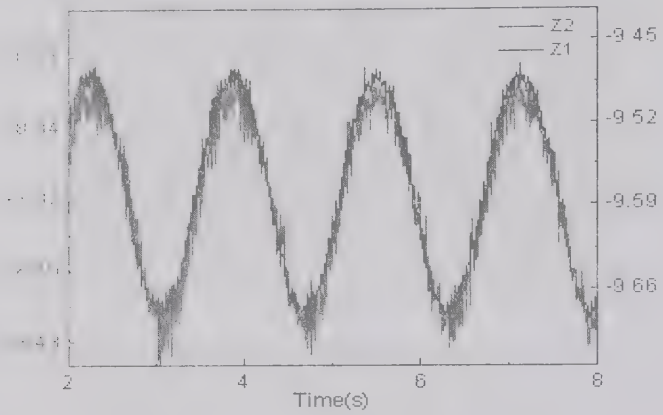

(a) The pressure of transducers Z1 and Z2, H=11 cm, and the soil is unliquefied

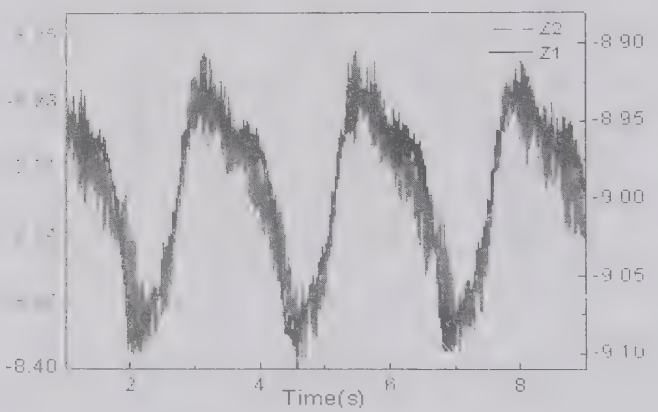

(b) The pressure of transducers Z1 and Z2, H=11 cm, h=27 cm

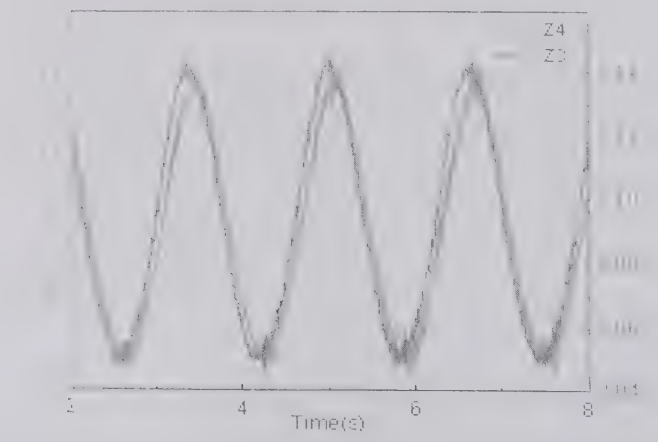

(c) The pressure of transducers Z3 and Z4, H=11 cm, and the soil is unliquefied

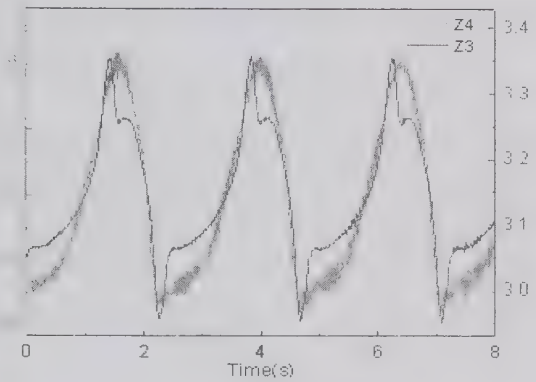

(d) The pressure of transducers Z3 and Z4, H=11 cm, h=37 cm

Fig. 5 The pressure of transducers at different stages in test B, H=11 cm

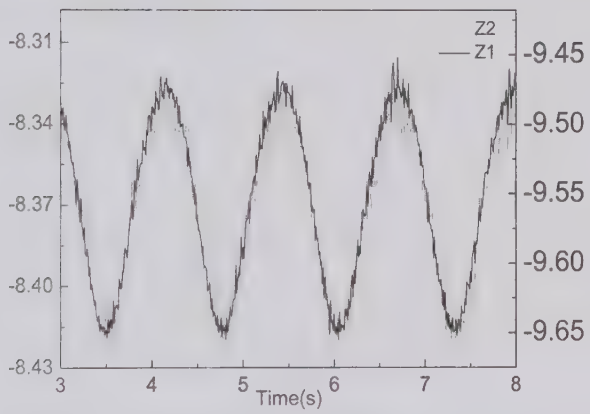

(a) The pressure of transducers Z1 and Z2, H=14 cm, and the soil is unliquefied.

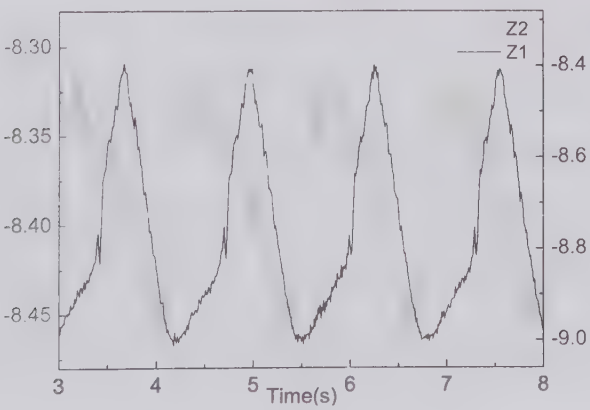

(b) The pressure of transducers Z3 and Z4, H=14 cm, h=42 cm

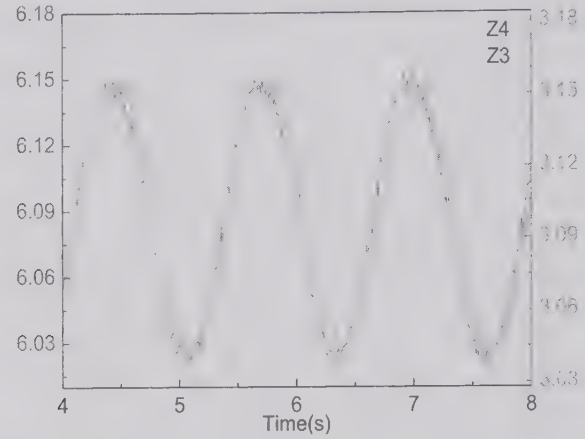

c. The pressure of transducers Z3 and Z4,H=11 cm, and the soil is unliquefied.

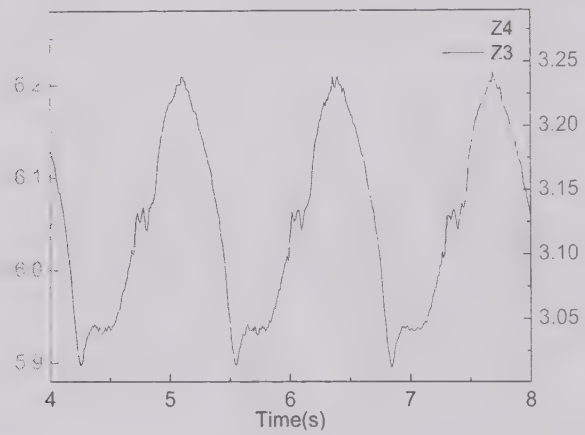

d. The pressure of transducers Z3 and Z4, H=14 cm, h=45 cm

Fig. 6 The pressure of transducers at different stages in test B , H=14 cm

In Trial A, it can be seen from Figure 3-a, 3-c, 4-a and 4-c, when the bed was unliquefied, the vertical upward and downward pressure that the buried pipeline stood were changing periodically. The curves overlapped completely and they reached a maximum value or a minimum value at the same time. However, Fig. 3-b，3-d, 4-b and 4-d show , when the bed was liquefied, especially the liquefaction depth reached the location below the pipeline, the vertical upward and downward pressures that the buried pipeline stood were also changing periodically. But the curves didn't overlap or reach the maximum or minimum value at the same time. As the wave height and the liquefaction depth increased, the phase difference between two pressure curves increased accordingly.

The result of Trial B was basically identical with that of Trail A. It proved that, whether using steel pipes or PVC pipes, the impacts of soil liquefaction on the pipe vertical pressure

were basically the same.

3.2 The resultant pressure amplitude at different stages

The sum of the current pressure values of the two probes is the vertical resultant pressure on the pipeline. Since the experiment collection system is broken down in Trial A, the related research in this paper was based on the data collected from Trial B. The vertical upward pressure on the pipeline was positive, while the vertical downward pressure was negative. The current pressure at each point in the various stages is shown in Fig. 8 and Fig. 9.

As the experiment moved on, the loss of soil happened due to the erosion under the wave loading, and the soil properties also changed to some extent. Therefore it couldn't be guaranteed that apart from wave height and the depth of liquefaction, all influencing factors e.g., the thickness of the overlying soil, were totally the same at the different stages of the experiments. This might result in several uncertain variables in the experiment. Therefore, it is inappropriate to study the impact of the wave height and the depth of liquefaction on the mechanical behavior of the pipeline with the resultant pressure.

This paper attempted to investigate the variation of resultant pressure value at the same point of the buried pipeline in different stages. The variation was reflected by the resultant pressure amplitude from one side in the experiments. The resultant pressure amplitude is shown in Fig. 7, and the value of the resultant pressure amplitude at different stages is shown in Fig. 10.

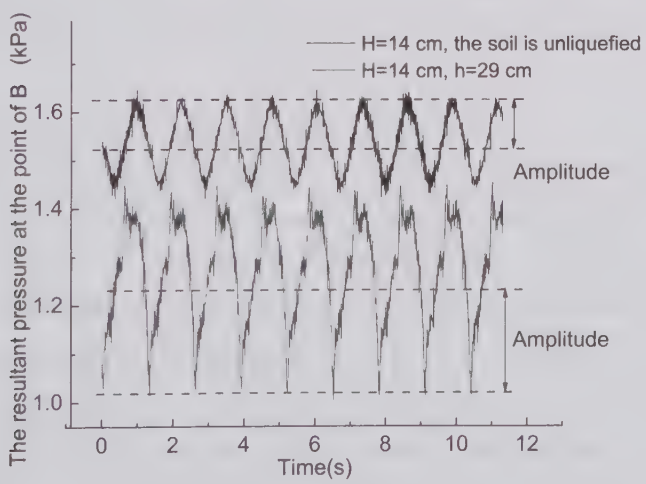

Fig. 7 Sketch map of the resultant pressure amplitude

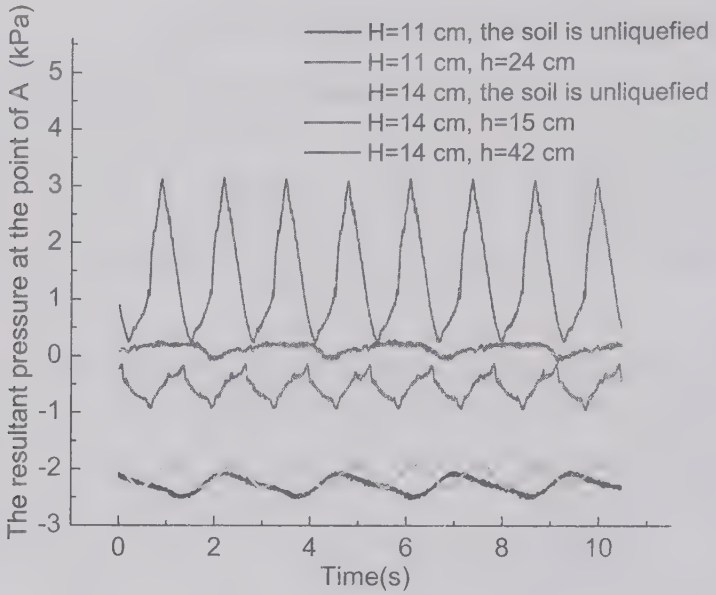
H=11 cm, the soil is unliquefied
H=11 cm, h=24 cm
H=14 cm, the soil is unliquefied
H=14 cm, h=15 cm
H=14 cm, h=42 cm
The resultant pressure at the point of A (kPa)
Time(s)

Fig. 8 Resultant pressure at the point A in the various stages

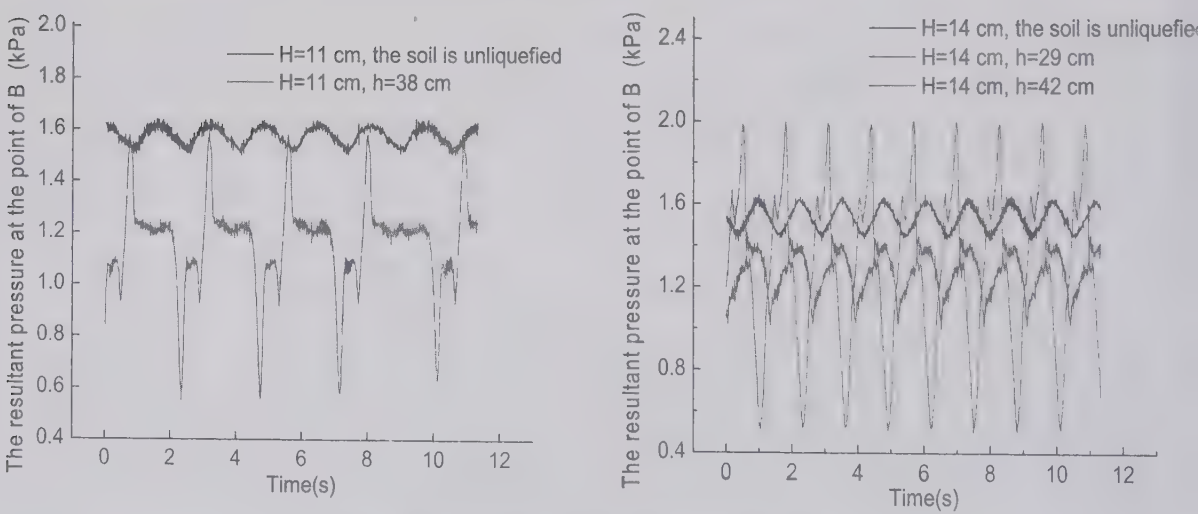
H=11 cm, the soil is unliquefied
H=11 cm, h=38 cm
The resultant pressure at the point of B (kPa)
Time(s)
H=14 cm, the soil is unliquefie
H=14 cm, h=29 cm
H=14 cm, h=42 cm
The resultant pressure at the point of B (kPa)
Time(s)

Fig. 9 Resultant pressure at the point B in the various stages

Fig. 7, Fig. 8 and Fig. 10 show that, when the bed was unliquefied, the higher the wave height was, the bigger the resultant amplitude on the pipeline was. But this change was not obvious. Under the same wave loading, when the bed was liquefied, the resultant pressure value was bigger than that when it was unliquefied, and the more the liquefaction of bed was, the bigger the resultant pressure value was. This situation was especially obvious when the liquefaction depth was beyond the buried depth (20 cm) of the pipeline.

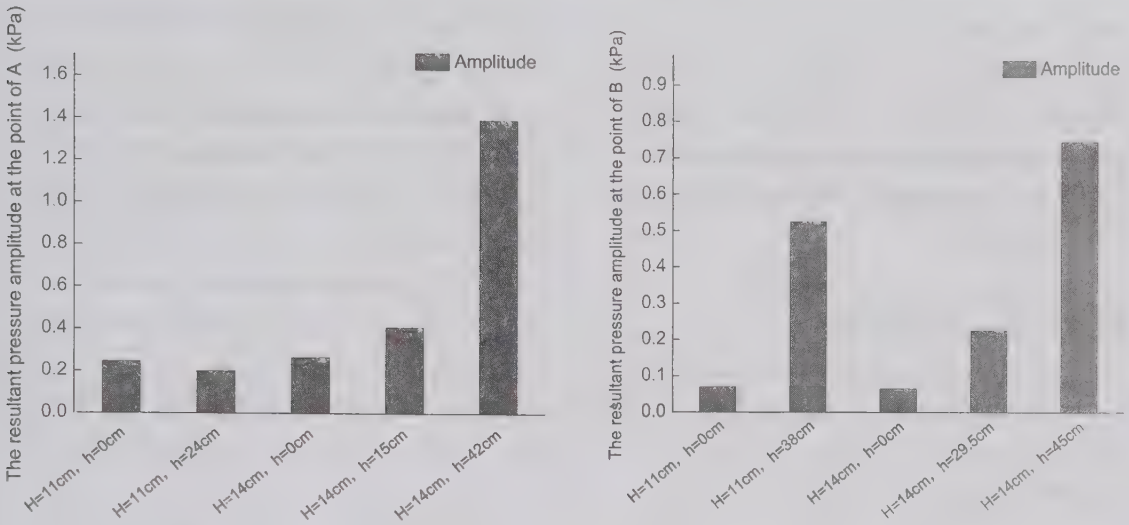

Fig. 10 Resultant pressure amplitude at each site in the various stages

4 Conclusions

This paper investigated the influence of soil liquefaction on the vertical mechanical behavior of submarine pipeline under the wave loading by wave flume tests. The conclusions are drawn as follows:

(a) When the bed is unliquefied under the wave loading, the vertically upward and downward pressure changes periodically and overlaps completely on the same cross section of pipeline. They reach a maximum value or a minimum value at the same time. Since the two pressures are on the opposite direction, the pressure on the vertical direction is relatively small.

(b) When the bed is liquefied under the wave loading, the vertically upward and downward pressure on the same cross section of the pipeline also changes periodically, but does not overlap. There is a phase difference between two pressure curves, and as the wave height increases, the liquefaction depth increases, while the phase difference increases accordingly. This research also shows that the vertically resultant pressure value of the pipeline obviously increases more than that when it was unliquefied. This makes the pipeline less steady.

(c) This paper investigated how the pressure changed at different situations from one side by the resultant pressure amplitude. The results show that:

As the wave height increases, the resultant pressure amplitude increases. When the

bed is unliquefied, exerting the same wave, the resultant pressure amplitude gets larger than that of the unliquefied bed. Under the same wave loading, when the bed is liquefied, the resultant pressure amplitude is bigger than that when it is unliquefied. When the bed gets liquefied, especially the liquefaction depth is beyond the burial depth of the pipeline, with the increasing of the liquefied depth, the resultant pressure amplitude increases simultaneously.

Acknowledgements

This work was supported by the grant from the National Natural Science Foundation of China (No. 41076021), and special gratitude is extended to Mr. Li Xiaoqian for his excellent assistance in English.

References

[1] Jothi Shankar N, Raman H, Sundar V. Wave forces on large offshore pipelines [J]. Ocean Engineering. 1985, 12 (2): 99 - 115.

[2] Sumer B M, Jensen B L, Fredsoe J. Effect of a plane boundary on oscillatory flow around a circular cylinder [J]. Journal of Fluid Méchanics, 1991, 225: 271 - 300.

[3] G Anandkumar, V Sundar, K U Graw et al. Pressures and forces on inclined cylinders due to regular waves [J]. Ocean Engineering, 1995, 22: 747 - 759.

[4] Yan shuwang, wang jinying. Research on instability of marine pipelines buried in soft clay under cyclic loading by model testing on the vibrating table [J]. The Ocean Engineering. 1998, 16 (4): 39 - 47.

[5] B M Sumer, J Fredsøe, S Christensen et al. Sinking/floatation of pipelines and other objects inliquefied soil under waves [J]. Coastal Engineering, 1999, 38: 53 - 90.

[6] B M Sumer, C Truelsen, T Sichmann et al. Onset of scour below pipelines and self-burial [J]. Coastal Engineering, 2011, 42: 313 - 335.

[7] Zhu Jiwei, Qiu changlin, Yan shuwang. The movement and forcing analysis on subsea pipeline under liquefied soil [J]. Petroleum Engineering Construction, 2002, 2(1): 11 - 13.

[8] T C The, A C Palmer, J S Damgaard. Experimental study of marine pipelines on unstable andliquefied seabed [J]. Coastal Engineering, 2003, 50: 1 - 17.

[9] Vijaya Kumar, A Neelamani, S Narasimha Rao. Wave pressures and uplift forces on and scour around submarine pipeline in clayey soil [J]. Ocean Engineering, 2003, 30 (2): 271 - 295.

[10] Jishang Xu, Guangxue Li, PingDong, et al. Bedform evolution around a submarine pipeline and its effects onwave-induced forces under regular waves [J]. Ocean Engineering, 2010, 37: 304 - 313.

[11] Fu-Ping Gao, Xi-TingHan, JingCao, et al. Submarine pipeline lateral instability on a sloping sandy

seabed [J]. Ocean Engineering, 2012, 50: 44 - 52.

[12] ZHANG Zhi-yong, SHI Bing, RUANXue-jing, et al. Study on the submarine pipeline with spoiler under wave action [J]. The Ocean Engineering, 2012, 30(4): 90 - 96.

[13] LIU cheng xiang. Research of the distributions of the flow field and pressure near the submarine pipeline under the action of oblique wave and current [D]. Master degree thesis, Changsha University of Science & Technology, Changsha, 2012.

[14] Xiang-Lian Zhou, Dong-Sheng Jeng, Yu-Guang Yan, et al. Wave-induced multi-layered seabed response around a buried pipeline [J]. Ocean Engineering, 2013, 72: 195 - 208.

[15] Xiang-Lian Zhou, Jian-Hua Wang, Jun Zhang et al. Wave and current induced seabed response around a submarine pipeline in an anisotropic seabed [J]. Ocean Engineering, 2014, 75: 112 - 127.

波浪作用下土体液化对埋置管线垂向受力的影响

游 启[1, 2]，许国辉[1, 2 *]，王秀海[2]，吕楚岫[1, 2]，刘志钦[1, 2]，孟庆生[2]

（1. 海洋环境与生态教育部重点实验室 山东 青岛，266100；
2. 中国海洋大学环境科学与工程学院，山东 青岛， 266100）

摘 要：本文通过室内波浪水槽试验，研究底床液化对埋置管线垂向受力的影响。试验中，在底床液化与底床未液化两种情况下施加相同的波浪，通过管线同一横截面上布置的两个反向（竖直向上、竖直向下）土压探头，测量管线垂直方向实时受力。结果表明，底床未液化时，两受力曲线都呈周期性变化且完全重合，它们将在同一时间达到最大值（最小值），管线的合力变幅较小；在底床液化时，两受力曲线也呈周期性变化但不完全重合，不会在同一时间达到最大值(最小值)，管线的合力变幅较大。这表明在底床液化时，埋置管线在垂直方向上所受合力比未液化时大，可能引起管道的下沉上浮乃至疲劳损坏。

关键词：土体；液化；管线垂向受力；相位滞后；水槽实验

Vertical distribution of the Kuroshio velocity in the Pollution Nagasaki section and its formative mechanism

DENG Li-jing[1], WEI Hao[2]*, WANG Jia-ning[3]

1. *National Marine Data & Information Service, Tianjin* 300171, *China;*
2. *School of Marine Science and Technology, Tianjin University, Tianjin* 300072, *China;*
3. *Institute of Oceanology, Chinese Academy of Sciences, Qingdao* 266071, *Shandong province, China*

Abstract: The seasonal and interannual variations of the vertical distribution of the Kuroshio velocity and its formative mechanism were studied by analyzing the Global Ocean Reanalysis Simulation 2 (GLORYS2) dataset in the Pollution Nagasaki (PN) section (126.0 °E–128.2 °E, at depths less than 1000 m). The results indicated that: 1) the maximum transport in the PN section occurs in summer, followed by spring, and the minimum transport occurs in fall and winter; the maximum velocities are located at the subsurface in both winter and summer and velocities are relatively larger and at a shallower depth in summer; and the velocity core is located at the surface in spring and fall. The isopycnic line has a clear depression around the Kuroshio axis in winter. The depth of maximum velocity and the zero horizontal density gradients both exhibit substantial seasonal and interannual variations, and the interannual variations are larger. 2) The distributions of velocity and density are in accordance with the thermal wind relation. Although Kuroshio transport is determined by the large-scale wind field and mesoscale motion in the Pacific Ocean; local heat flux and thermohaline circulation influence the density field, modify the vertical structure of the Kuroshio velocity, and adjust the allocation of water fluxes and nutrients transport. 3) Shelf-water offshore transport into the Kuroshio upper layer induced by southwest monsoons might contribute to the maximum velocity up to the surface in summer. Nonlinear and nongeostrophic processes are not considered in the present study, and the thermal wind relation accounts for part of the vertical structure of the Kuroshio velocity.

Keywords: Kuroshio, vertical distribution of velocity, thermal wind relation, PN section

The Kuroshio is the western boundary current in the North Pacific Ocean with large transports, a high temperature, and high salinity (Sun, 2008). It carries substantial nutrients (Nitani, 1972) and is the major nutrient source of the East China Sea (Liu et al., 1992; Chen

Received on Sep. 3, 2014

*Corresponding author: weihao@ouc.edu.cn

et al., 1995; Liang et al., 2003). The vertical structure of the Kuroshio velocity can affect nutrient transport in the East China Sea because of the large vertical discrepancy in nutrient concentration (Guo et al., 2012).

Numerous researchers have observed the vertical structure of the Kuroshio velocity and found that the maximum Kuroshio speed occurred around the subsurface in the PN section. Ichikawa and Beardsley (1993) found that the maximum velocity (approximately 1 m/s) occurred near a depth of 200 m in the PN section by using an acoustic Doppler current profiler (ADCP) and a geomagnetic electrokinetograph in August 1987. Ito et al. (1995) showed that the maximum velocity (approximately 0.8 m/s) occurred at a depth of 94 m along the F section (approximately 140 km north of the PN section) by using a ship-mounted ADCP in September 1991. Andres et al. (2008) studied the structure and transport of the Kuroshio in the East China Sea from October 2003 to November 2004 by using pressure probe plus inverted echo sounders and an ADCP along the PN section, and revealed that the maximum velocities (0.65 m/s and 0.68 m/s) occurred at the surface 30 km east of the shelf break and at the subsurface 70 km east of the shelf break.

In addition to in situ current observations, numerous researchers have also studied the vertical structure of the Kuroshio velocity by diagnosing dynamic height. Lin et al. (1993) calculated the Kuroshio velocity by using conductivity-temperature-depth (CTD) data from four cruises between 1988 and 1990, and showed that the maximum Kuroshio speed was mostly located at the subsurface in the northern Okinawa Trough. Yuan et al. (2006) analyzed hydrological data from five cruises and wind data from QuikSCAT in 2000 by using an inverse method, and found that the maximum Kuroshio velocity, 1.74 m/s, was at 30 m and an extreme value of 0.99 m/s occurred at 100 m in February. Based on the same method, Zhu et al. (2006) showed the structure of the Kuroshio velocity in the Tokara Strait between October and November 2000, and found that the maximum velocity of 0.89 m/s occurred at 460 m.

Subsurface maximum Kuroshio velocities have been revealed. However, a more in-depth analysis of the seasonal and interannual variations of the Kuroshio vertical structure is necessary. In this study, monthly three-dimensional fields of temperature, salinity, density, and velocity from January 1993 to December 2011 were acquired from Global Ocean Reanalysis Simulation 2 (GLORYS2). The PN section (126.0 °E - 128.2° E, at depths less than 1 000 m) was selected as the study area (Fig. 1). The seasonal and interannual variations of the vertical structure of the Kuroshio velocity were analyzed; this paper presents a preliminary discussion of its formative mechanism.

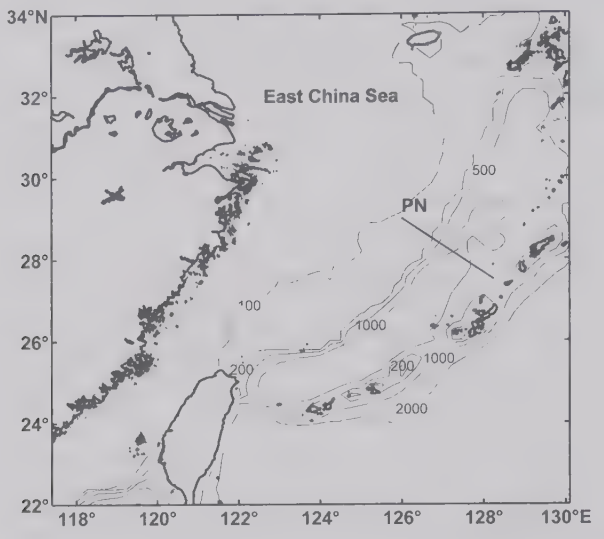

Fig. 1 Map of the study site with isobaths contoured in meters

(The location of the PN section is denoted by a solid line)

1 Data and methods

1.1 Introduction to GLORYS2

GLORYS2 is a global ocean reanalysis dataset provided by Mercator-Océan, France, that is based on the Nucleus for European Modeling of the Ocean, Ocean General Circulation Model; it is assimilated based on the in situ observed temperature, salinity, satellite sea surface temperature, and along-track sea-level anomaly by using the Mercator Assimilation System Version 2 (SAM2). SAM2 relies on a reduced order Kalman filter based on the SEEK formulation with a three-dimensional variable temperature and a salinity bias correction scheme, which is implemented to correct temperature and salinity biases when enough observations are obtained. GLORYS2 can effectively reflect the characteristics of large-scale circulation (Ferry et al., 2012a, 2012b). The dataset has a horizontal resolution of 0.25 × 0.25° and 75 vertical z-levels, and distances between the levels increase from 1 m at the surface to 200 m at the maximum depth of 5 902 m. The model is forced by ERA-Interim atmospheric parameters after calibration.

1.2 Validation of GLORYS2

The numerous validations of GLORYS2 that have been conducted by Mercator-Océan, France (Ferry et al., 2012a), are not repeated here. GLORYS2 has been used in the research on the Atlantic meridional overturning circulation (Ferry et al., 2012b)

and the Western Mediterranean deep-water formation in the Gulf of Lions (Beuvier et al., 2012). Thus, the notion that GLORYS2 can effectively reproduce global ocean dynamic processes is supported.

To evaluate the simulation of the Kuroshio around the PN section, the velocities normal in the PN section (V_n), temperatures, and salinities (126.0 °E - 128.2 °E, at depths less than 1000 m) obtained from GLORYS2 and from observations made by Andres et al. (2008; Fig. 2) and Oka (2000; Fig. 3) were compared. Data from GLORYS2 from October 2003 to November 2004 were averaged and were similar to those obtained from observations. The vertical structures of V_n, temperature, and salinity in the PN section from GLORYS2 and from observations exhibited favorable agreement. This indicates that GLORYS2 can represent the main features of the Kuroshio and the hydrography around the PN section.

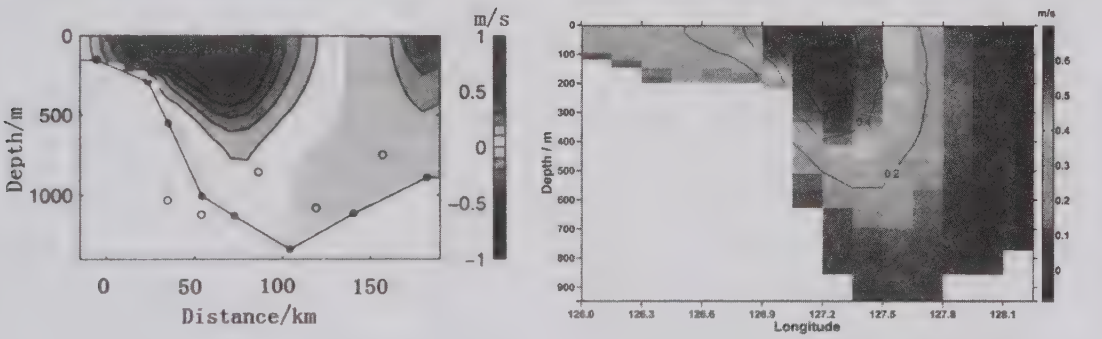

Fig. 2 Climatological velocity normal in the PN section (126.0 °E - 128.2 °E, at depths less than 1 000 m) obtained from observations (left; Andres et al., 2008) and GLORYS2 (right)

2 Seasonal variations in velocity and the density vertical structure in the PN section

Climatological velocities in spring, summer, fall, and winter were obtained by averaging the data of GLORYS2 in February, May, August, and November, respectively, over 19 years. Fig. 4 shows the longitude-depth variations of the northward Kuroshio velocity (v) in the PN section in spring, summer, fall, and winter. The Kuroshio flows northward with a velocity larger than 0.20 m/s along the shelf break and is concentrated within an area approximately 80 nautical miles in width and 800 m in depth. The transport of the Kuroshio across the PN section peaks in summer at 36 Sv, followed by spring at 35 Sv and fall at 33.3 Sv; it bottoms out in winter at 33 Sv. The seasonal variation of Kuroshio transport in the PN section is not substantial. Compared with the results of previous studies (Bai et al., 2010; Zhao et al., 2009), the seasonal variation determined in this study is

reasonable, although the value for transport is slightly larger. This might have been because the model grid resolution was insufficient for reproducing mesoscale processes (Li et al., 2011; Li et al., 2011). The vertical structure of the climatological velocity showed obvious seasonal variation. The strong current was distributed from 126.6 °E to 127.8 °E in the longitudinal direction and from the surface to a depth of 500 m. The range of the strong current was at its maximum in summer and its minimum in winter. In the region between 127.0 °E and 127.3 °E, the maximum velocity was located near 100 m at the subsurface both in winter and summer, with a maximum velocity of 0.56 m/s in winter and 0.63 m/s in summer. In contrast, the maximum velocity was located at the surface in spring and fall.

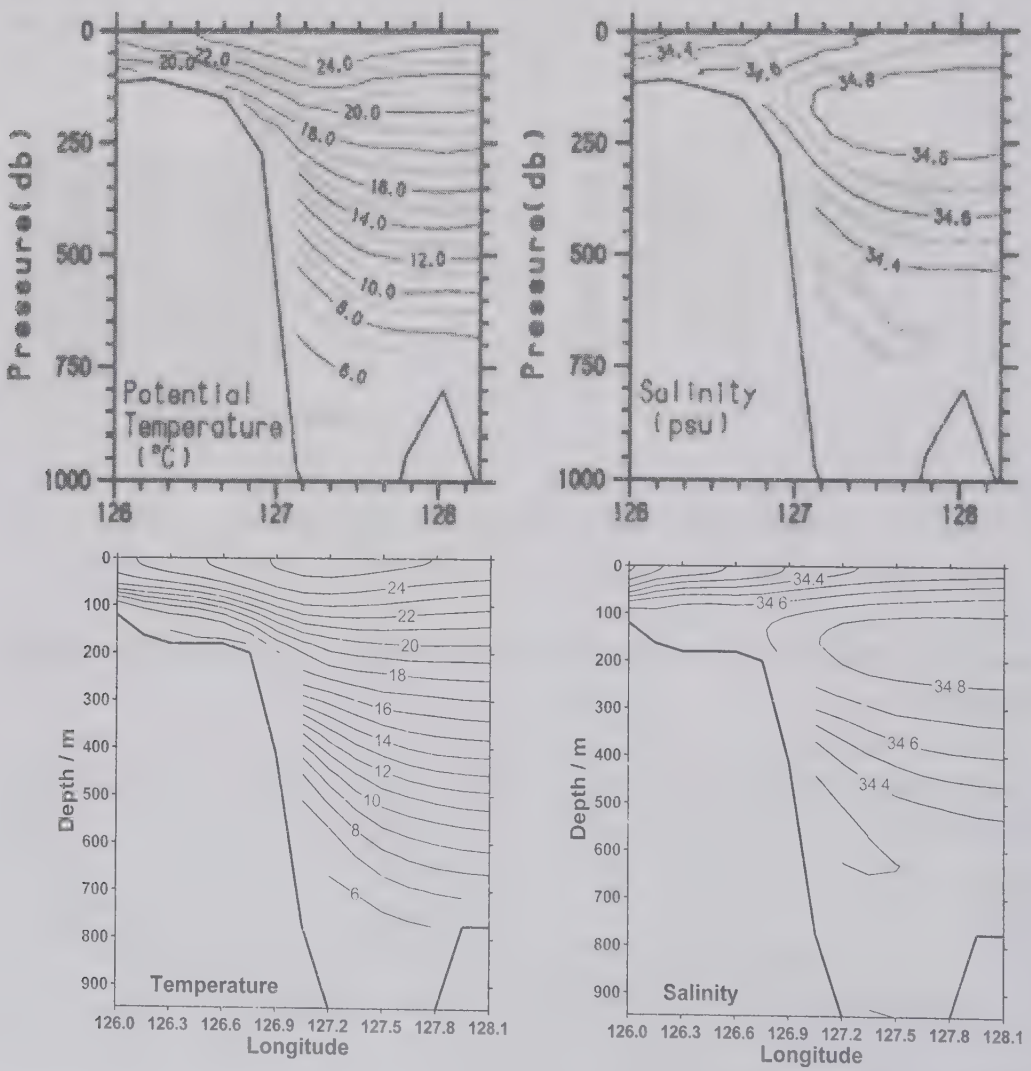

Fig. 3 Climatological temperature (left) and salinity (right) along the PN section (126.0 °E - 128.2 °E, at depths less than 1 000 m) obtained from observations (top; Oka, 2 000) and GLORYS2 (bottom).

To determine why the maximum velocity occurs at the subsurface, the density structure in summer and winter is analyzed. The distribution of climatological density in the PN section (Fig. 5) indicates that below 200 m, the isopycnics incline to deep water both in winter and summer; the density decreases from west to east, with high-density water upwelling to the shelf. Above 200 m, the density of the Kuroshio core (Fig. 5 left) is smaller than the densities of the east and west sides in winter, and isopycniclines sink in the Kuroshio main axis. Pycnoclines appear in summer (Fig. 5 right), and the difference in east-west density is small in the upper-mixed layer above 100 m, whereas under 100 m, the shelf water to the west of the Kuroshio axis has a high density; the density of the Kuroshio is similar to the east of the Kuroshio axis, but the Kuroshio water remains light. The reasons for density gradient formation can be drawn from the thermohaline distribution (Fig. 6 and Fig. 7) above 220 m in the PN section in winter and summer: the heat capacity of the water from the continental shelf is small; therefore, densification caused by cooling is remarkable in winter and causes the density of the shelf water to be greater than that of the Kuroshio at the same depth. The temperature of the Kuroshio is higher than that of the water to the east because of its constantly replenished calories from the lower latitudes, causing isopycnic lines to be concave at the axis; in other words, the density of the Kuroshio is lower than that of the water to the east. In summer, the entire section becomes warmer in the upper layer (at depths less than 100 m), and the salinity greatly decreases, leading to a density that is smaller than that in winter. Shelf-mixed water (salinity < 34) extends east in the upper layer to the area where the Kuroshio axis is located because of Ekman transport by the south wind. The Kuroshio subsurface water (at 18 °C and of maximum vertical salinity) stretches west to the shelf and can run along the 60 m isobaths (Yang et al., 2012). The intrusion of the Kuroshio subsurface water to the shelf (Li et al., 2013) makes the shelf bottom water denser than that of the Kuroshio at the same depth. In contrast, to the east of 127.0 °E (the position of the maximum velocity), at depths of 100 to 200 m, the Kuroshio water is higher in temperature and lower in salinity compared with water to the east of 127.0 °E, and the isopycnic lines tilt slightly upward from west to east (right, Fig. 5).

The horizontal density gradient is calculated from the climatological density in the PN section (Fig. 8); gradients above and below the contours of the zero gradient are considered positive and negative gradients, respectively. Near the high-velocity core position, the zero horizontal density gradient contour is deeper in winter than in summer. In the vertical direction, the position of the zero density gradients corresponds to that of the maximum velocity in Fig. 4 in both winter and summer.

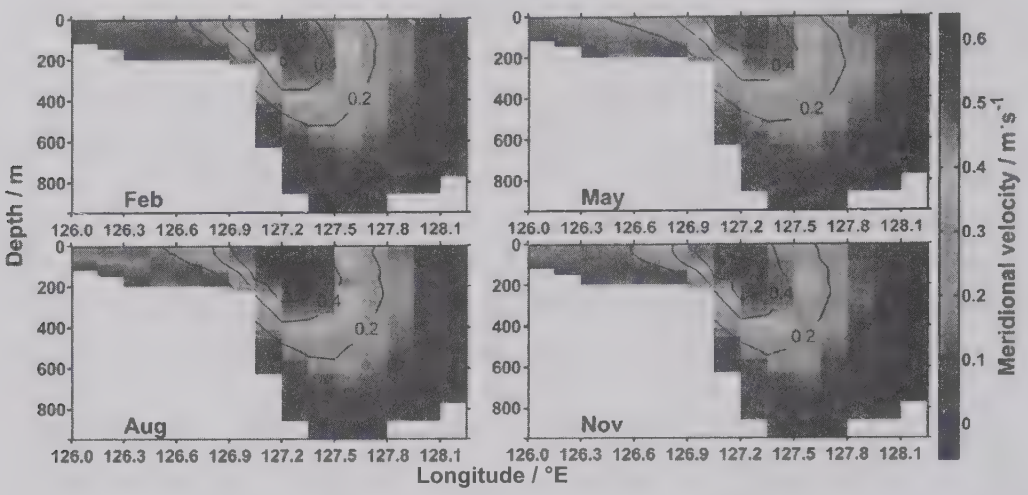

Fig. 4 Longitude-depth variation of the northward Kuroshio velocity (v) in the PN section (126.0 °E–128.2 °E, at depths less than 1 000 m) in February, May, August, and November, representing spring, summer, fall, and winter, respectively.

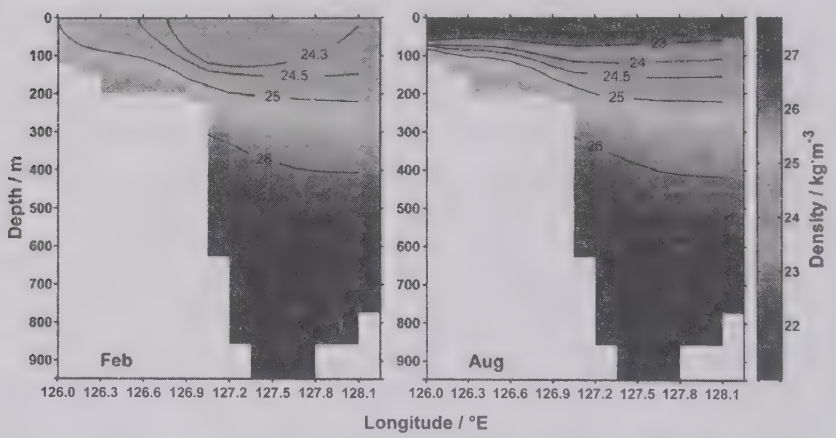

Fig. 5 Longitude–depth variation in density in the PN section (126.0 °E - 128.2 °E, at depths less than 1 000 m) in February (left) and August (right), representing winter and summer, respectively.

3 Interannual variations in velocity and density vertical structure in the PN section

The interannual variability of maximum velocity (V_{max}) in the profile from 1993 to 2011 at the Kuroshio axis (127.2 °E, at depths less than 500 m) was analyzed and the results are shown in Tab. 1. Over the 19 years, the V_{max} range was 0.58 ± 0.03 m/s; the minimum was 0.51 m/s and the maximum was 0.63 m/s.

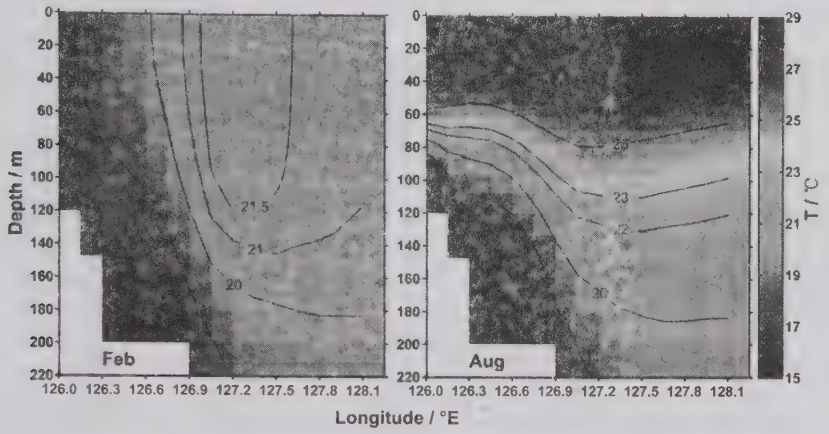

Fig. 6 Longitude–depth variation in temperature in the PN section (126.0 °E - 128.2 °E, at depths less than 220 m) in February (left) and August (right), representing winter and summer, respectively.

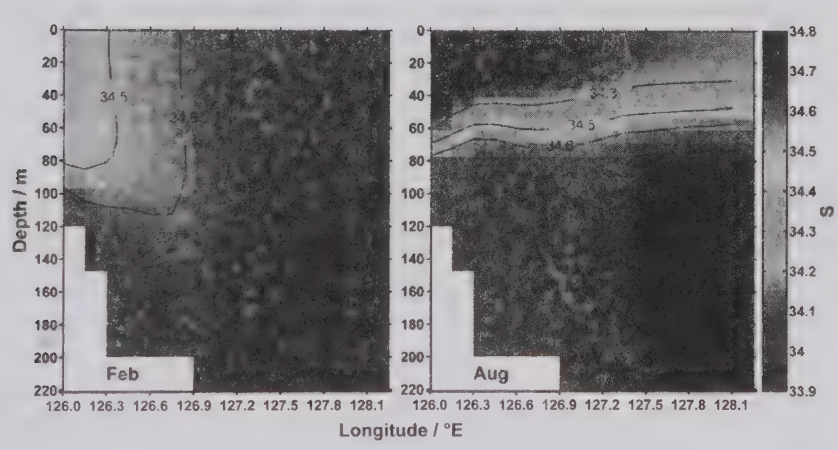

Fig. 7 Longitude–depth variation in salinity in the PN section (126.0 °E - 128.2 °E, at depths less than 220 m) in February (left) and August (right), representing winter and summer, respectively.

The vertical distribution of the velocity in the PN section differed in winter and summer over the 19 years, and the depth of maximum velocity (D_{vmax}) also varied. In winter (Fig. 9), the velocity ranged from 0.02 to 0.68 m/s and the V_{max} range was approximately 0.58 ± 0.07 m/s (Tab. 1); the maximum value was 0.68 m/s and the minimum value was 0.45 m/s. V_{max} occurred at 50 to 250 m at the subsurface. In summer (Fig. 10), the velocity was in the range of 0.02 to 0.72 m/s and the V_{max} range was 0.65 ± 0.06 m/s; the maximum was 0.72 m/s and the minimum was 0.51 m/s. D_{vmax} occurred above 150 m in most years, whereas V_{max} occurred at the surface in certain years (i.e., 1995, 1997, 2001, 2003–2005, 2007, and 2010). The interannual variability of V_{max} in winter was more substantial than that in summer. Such changes in velocity vertical structure greatly affected Kuroshio

calories and nutrient transport.

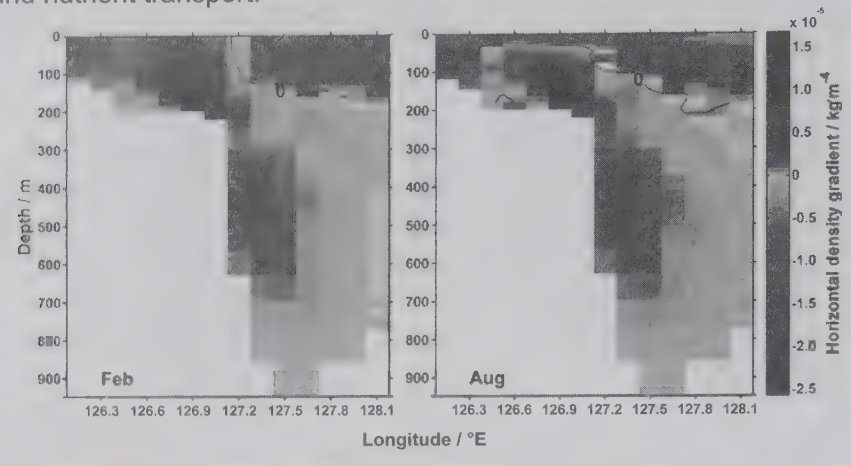

Fig. 8 Longitude–depth variation in horizontal density gradient in the PN section (126.0 °E - 128.2 °E, at depths less than 1 000 m) in February (left) and August (right), representing winter and summer, respectively. Zero contours are denoted with black curves.

In winter, the scope of the horizontal density gradient was between -1.70e-5 and 0.60e-5 kg/m^4, and the depth of zero horizontal density gradients ($D_{0\nabla\rho}$) was above 300 m. In years when D_{vmax} was deep (i.e., 1999 and 2005), the location of the zero horizontal density gradient was also deep. In summer, the scope of the horizontal density gradient was between -1.40e-5 and 1.04e-5 kg/m^4. The interannual variabilities of $D_{0\nabla\rho}$ and D_{vmax} corresponded to each other in winter and summer.

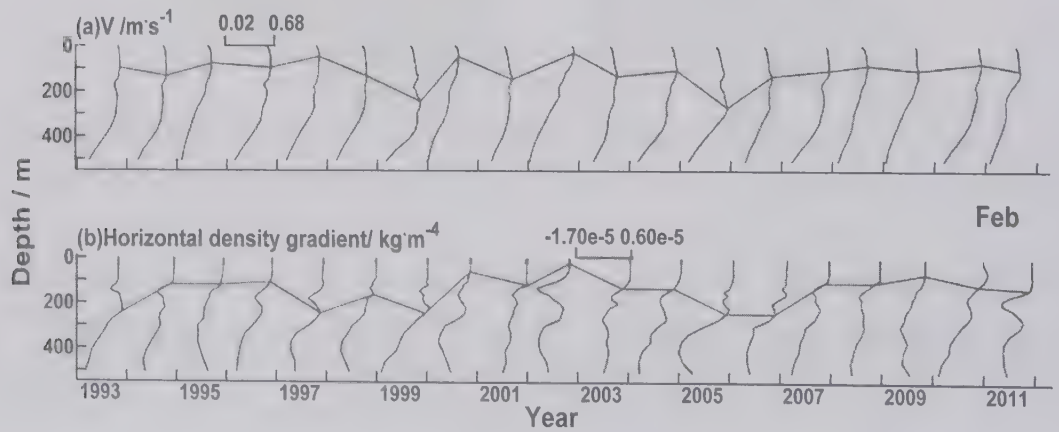

Fig. 9 Profiles of the flow speed (a) and the horizontal density gradient (b) in February from 1993 to 2011 in the PN section (127.2 °E)

(Top lines indicate the maximum flow speed and zero horizontal density gradient in each profile. The flow speed and horizontal density gradient range from 0.02 to 0.68 m / s and -1.70e-5 to 0.6e-5 kg/m^4, respectively.)

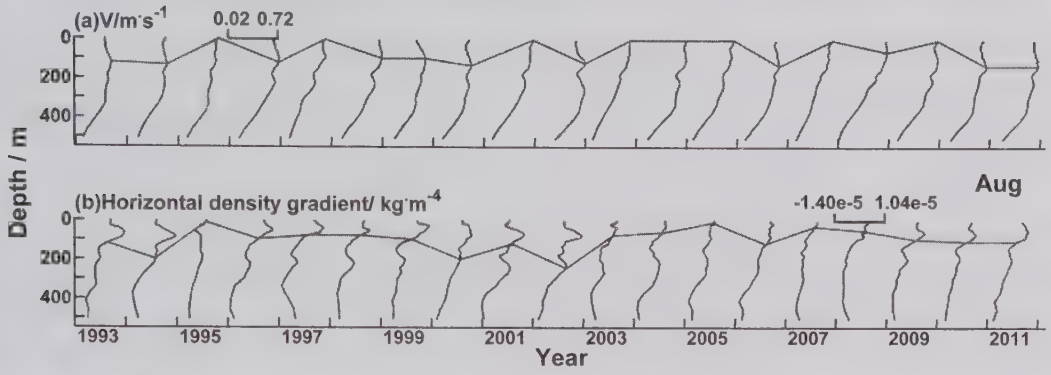

Fig. 10 Profiles of the flow speed (a) and the horizontal density gradient (b) in August from 1993 to 2011 in the PN section (127.2 °E)

(top lines indicate the maximum flow speed and zero horizontal density gradient in each profile. The flow speed and horizontal density gradient range from 0.02 to 0.72 m s-1 and -1.40e-5 to 1.04e-5 kg/m^4, respectively)

Tab. 1 Statistics on normal Kuroshio speed in the PN section at 127.2 °E (at depths less than 500 m) from 1993 to 2011 (m / s)

	Minimum	Maximum	Annual average	Standard deviation
Annual average V_{max}	0.51	0.63	0.58	0.03
V_{max} in February	0.45	0.68	0.58	0.07
V_{max} in August	0.51	0.72	0.65	0.06

Note: V_{max} is the maximum velocity in each vertical profile

4 Formative mechanism of the velocity vertical structure

The Kuroshio is a western boundary current that satisfies geostrophic balance. It is mainly composed of a northward current. Thermal wind relations described in (1) can be used to explain why the Kuroshio maximum velocity occurs at the subsurface:

$$\frac{\partial v}{\partial z} = -\frac{g}{f\rho_0}\frac{\partial \rho}{\partial x} \tag{1}$$

where v is the meridional velocity, f represents the Coriolis parameter, ρ is the density, and ρ_o is the reference density.

Equation (1) shows that the vertical velocity shear is caused by the horizontal density gradient. Density varies layers in the regions of the shelf, the Kuroshio, and east of the Kuroshio, resulting in a vertical variation in the northward current. Where zero horizontal density gradient are located, the velocity shear is zero and the velocity is at its extreme.

The distributions of climatological velocity and density (Fig. 4 and Fig. 5) show that to the east of 127.0 °E in the PN section, the density decreases toward the east in the middle layer and the horizontal density gradient is negative; in other words, if $\partial\rho/\partial x < 0$, then $\partial v/\partial z > 0$, causing a positive shear in the south-north direction and increasing the northward velocity in the shallower layer. In the surface layer, the density slightly increases toward the east and the horizontal density gradient is positive; in other words, if $\partial\rho/\partial x > 0$, then $\partial v/\partial z<0$; v increases under the surface. At the position of the zero hortizontal density gradients, the northward velocity reaches its maximum, and therefore, the maximum velocity occurs at the subsurface.

From the seasonal (Fig. 4 and Fig. 8) and interannual variation (Fig. 9 and Fig. 10) of velocity and horizontal density gradient in the PN section, it can be concluded that $D_{0\nabla\rho}$ corresponds with D_{vmax}, which satisfies the thermal wind relation.

The interannual variation of D_{vmax} and $D_{0\nabla\rho}$ at 127.2 °E in the PN section showed that the two depths were highly correlated in winter and summer. The correlation coefficient R was 0.61 in winter and 0.64 in summer (confidence level > 99.50%). The results of further statistical analysis of D_{vmax} and $D_{0\nabla\rho}$ are shown in Tab. 2. The average illustrates the climatological state and the standard deviation reflects the interannual variation. In winter, the range of $D_{0\nabla\rho}$ was 144.41 m ± 68.72 m, and the range of D_{vmax} was 115.24 m ± 59.80 m. In summer, $D_{0\nabla\rho}$ was in the range of 100.73 m ± 61.35 m, and D_{vmax} was in the range of 67.61 m ± 61.22 m. Overall, the average D_{vmax} was smaller than the average $D_{0\nabla\rho}$; this is also true of the standard deviation. D_{vmax} and $D_{0\nabla\rho}$ were deeper in winter than in summer; though the changes in D_{vmax} were smaller in winter. The standard deviations of the two depths were close in both winter and summer, and the difference in standard deviation was much smaller than their own value. Therefore, the interannual variability of the two depths was much larger than the climatological seasonal variation in winter and summer.

According to the thermal wind relation, the vertical velocity shear equals zero at the depth of the zero horizontal density gradient. Thus, the position of zero shear is the most likely location for the velocity to reach its maximum. Nonlinear and nongeostrophic processes are not considered in the thermal wind relation; therefore, $D_{0\nabla\rho}$ and D_{vmax} are inconsistent.

Tab. 2 Statistics of $D_{v\max}$ and $D_{o\nabla p}$ in the PN section

Month	Correlation coefficient R of $D_{v\max}$ and $D_{o\nabla p}$	Average of $D_{o\nabla p}$ / m	Standard deviation of $D_{o\nabla p}$ / m	Average of $D_{v\max}$ / m	Standard deviation of $D_{v\max}$ / m
February	0.61	144.41	68.72	115.24	59.80
August	0.64	100.73	61.35	67.61	61.22

Note: $D_{v\max}$ is the depth of the maximum northward velocity; $D_{o\nabla p}$ is the depth of the zero horizontal density gradient.

5 Conclusions

The seasonal and interannual variations in the vertical distribution of the Kuroshio velocity and its formative mechanism were studied by analyzing the GLORYS2 (Global Ocean Reanalysis Simulation 2) dataset in the PN section (126.0 °E - 128.2 °E, at depths less than 1 000 m). The main results are as follows:

(1) Climatologically, transport in the PN section does not substantially change seasonally; however, the maximum occurs in summer, followed by spring, and the minimum occurs in fall and winter. The maximum velocities occur at the subsurface both in winter and summer. In summer, the velocity is larger and occurs at a shallower depth. The velocity core is located at the surface in spring and fall. The isopycnicline has a clear depression around the Kuroshio axis in winter. The depths of the maximum velocity and the zero horizontal density gradients both have substantial seasonal and interannual variations, and interannual variations are larger.

(2) The distribution of the vertical velocity and the horizontal density gradient are highly correlated seasonally and interannually. The distributions of the velocity and density are in accordance with the thermal wind relation; in other words, the maximum velocity occurs at the depth at which the horizontal density gradient is zero. Although Kuroshio transport is determined by the large-scale wind field and mesoscale motion in the Pacific Ocean; local heat flux and circulation influence the density field, modify the vertical structure of the Kuroshio velocity, and adjust the allocation of water fluxes and nutrient transport.

(3) Shelf-water offshore transport into the Kuroshio upper layer induced by the southwesterly monsoon can reduce the horizontal density gradient. The zero density gradient becomes relatively uplifted, which in turn raises the position of the maximum velocity in summer.

Nonlinear and nongeostrophic processes are not considered in the present study. The high correlation of $D_{0\nabla\rho}$ and D_{vmax} analyzed in this study reveals that the thermal wind relation accounts for part of the vertical structure of the Kuroshio velocity.

References

[1] Andres M, Wimbush M, Park J H, et al., 2008. Observations of Kuroshio flow variations in the East China Sea [J]. Journal of Geophysical Research: Oceans (1978 - 2012), 113(C5): 1 - 14.

[2] Bai Z P, Gao S, Wang H T. A HYbrid Coordinate Ocean Model (HYCOM) for simulating the climatological Kuroshio in the East China Sea [J]. Marine Science Bulletin, 2010, 29(2): 121 - 129.

[3] Beuvier J, Béranger K, Lebeaupin Brossier C, et al. Spreading of the Western Mediterranean Deep Water after winter 2005: Time scales and deep cyclone transport[J]. Journal of Geophysical Research: Oceans (1978 - 2012), 2012, 117(C7): 1 - 26.

[4] Chen C T A, Ruo R, Paid S C, et al. Exchange of water masses between the East China Sea and the Kuroshio off northeastern Taiwan [J]. Continental Shelf Research, 1995, 15(1): 19 - 39.

[5] Ferry N, Parent L, Garric G, et al. GLORYS2V1 Global Ocean Reanalysis of the Altimetric Era (1993 - 2009) at Meso Scale [J]. Sletter, 2012a.

[6] Ferry N, Barnier B, Garric G, et al. NEMO: The modeling engine of global ocean reanalysis [J]. Mercator Ocean Quarterly Newsletter, 2012b.

[7] Guo X Y, Zhu X H, Wu Q S, et al. The Kuroshio nutrient stream and its temporal variation in the East China Sea [J]. Journal of Geophysical Research: Oceans (1978 - 2012), 2012, 117(C1): 1 - 17.

[8] Ichikawa H, Beardsley R C. Temporal and spatial variability of volume transport of the Kuroshio in the East China Sea [J]. Deep Sea Research Part I: Oceanographic Research Papers, 1993, 40(3): 583 - 605.

[9] Ito T, Kaneko A, Furukawa H, et al. A structure of the Kuroshio and its related upwelling on the East China Sea shelf slope [J]. Journal of Oceanography, 1995, 51(3): 267 - 278.

[10] Li J X, Wei H, Zhang Z H, et al. A modelling study of inter-annual variation of Kuroshio intrusion on the shelf of East China Sea [J]. Journal of Ocean University of China, 2013, 12(4): 537 - 548.

[11] Li J X, Zhang R, Liu C Z, et.al. Ocean mesoscale eddy modeling and its application in studying the effect on underwater acoustic propagation. Marine Science Bulletin, 2011, 30(1): 37 - 46.

[12] Li W, Wang Q, Ma J R, et al. Study on the meso-scale process of the Kuroshio front to the east of Taiwan[J]，Marine Science Bulletin, 2011, 30(5): 518 - 528.

[13] Liang W D, Tang T Y, Yang Y J, et al. Upper-ocean currents around Taiwan[J]. Deep Sea Research Part II: Topical Studies in Oceanography, 2003, 50(6): 1 085 - 1 105.

[14] Lin K, Shu L H, Haruo Ishii，et al. The current structure and volume transport of the Kuroshio in the northern east china sea. Kuroshio research papers (five) [M]. Beijing: Maritime Press, 1993, 42:51.

[15] Liu K K, Gong G C, Shyu C Z, et al. Response of Kuroshio upwelling to the onset of the northeast monsoon in the sea north of Taiwan: Observations and a numerical simulation [J]. Journal of Geophysical Research, 1992, 97(C8): 12 511 - 12 526.

[16] Nitani H. Beginning of the Kuroshio [J]. Kuroshio, its physical aspects, 1972, 129 - 163.

[17] Oka E. Characteristic of variations of water and dynamic properties of the Kuroshio in the East China Sea[D]. Ph. D. thesis, Grad. Sch. of Sci., Univ. of Tokyo, Tokyo. 2000.

[18] Sun X P. China Regional Seas [M]. Beijing: Navy Press, 2008, 111 - 118.

[19] Yang D Z, Yin B S, Liu Z L, et al. Numerical study on the pattern and origins of Kuroshio branches in the bottom water of southern East China Sea in summer [J]. Journal of Geophysical Research: Oceans (1978 - 2012), 2012, 117(C2).

[20] Yuan Y C, Yang C J, Wang Z G. Variability of the Kuroshio in the East China Sea and the currents east of Ryukyu Islands: I Variability of the Kuroshio in the East China Sea and the meso-scale eddies near t`he Kuroshio in 2000 [J]. Acta Oceanologica Sinica, 2006, 28(2): 1 - 13.

[21] Zhao J, Wu D X, Chen X E, et al. Simulation of Kuroshio with eddy resolution model[J]. Marine Science Bulletin, 2009, 28(5): 13 - 20.

[22] Zhu X H, Park J H, Kaneko I. Velocity structures and transports of the Kuroshio and the Ryukyu Current during fall of 2000 estimated by an inverse technique [J]. Journal of Oceanography, 2006, 62(4): 587 - 596.

PN 断面黑潮流速垂直分布特征及机制分析

邓丽静[1]，魏 皓[2*]，汪嘉宁[3]

（1. 国家海洋信息中心，天津 300171；2. 天津大学 海洋科学与技术学院，天津 300072；
3. 中国科学院海洋研究所，山东 青岛 266071）

摘 要：本文基于全球海洋再分析模拟 GLORYS2(Global Ocean Reanalysis Simulation 2)结果，分析了 PN 断面（126.0°E-128.2°E，1 000 m 以浅）黑潮流速垂直结构的季节和年际变化，探讨了黑潮流速垂直结构形成的动力学机制。结果表明：1）PN 断面黑潮夏季流量最大，春季次之，秋、冬季节最小；气候态平均的冬、夏季流速最大值都位于次表层，春、秋季节流速最大值位于表层；夏季相对流速较大、最大值深度较浅；等密线在黑潮主轴区下凹，冬季更为明显。流速最大值深度和密度水平梯度为零的深度均表现出了较大的年际差异，该年际变化甚至超过季节差异；2）流速与密度符合热成风关系。黑潮通量由太平洋大尺度风场及中尺度运动两者共同决定，但局地的热通量和环流对温盐的输运共同影响密度场，调节黑潮流速的垂直分布，影响水通量的分配及营养盐输运；3）有些年份夏季流速最大值出现在表层，可能是夏季西南季风诱导陆架水离岸输运进入黑潮上层导致的结果。非线性、非地转物理过程的影响没有考虑在本研究中，热成风关系能够解释黑潮流速垂直分布形成的部分原因。

关键词：黑潮；流速垂直分布；热成风关系；PN 断面

Focal mechanism solution statistics of seismic tsunami sources

HOU Jing-ming, XU Zhi-guo

National Marine Environmental Forecasting Center, Beijing 100081, *China*

Abstract: In recent years, tsunami happens frequently in the world, which caused huge losses. In order to find objective features of tsunamigenic source, global CMT data from 1976 to 2010 and tsunami data from NOAA are analyzed statistically, tsunami is compared with bigger tsunamis. At last, some features of seismic tsunami sources are concluded.

Keywords: tsunamigenic earthquake, focal mechanism solution, feature

The tsunami is a kind of ocean wave with huge wavelength and period, occurring in the ocean. Tsunami waves can be generated by sudden vertical displacements of large-scale water resulting from underwater earthquakes, landslides, volcanic eruptions, icebergs, and meteorites. Such events can disturb the ocean's surface, displace water, and generate destructive tsunami waves (Yang Gangsheng et al., 2000). The term "tsunamigenic earthquake" refers to the earthquake which could trigger a tsunami. The undersea earthquake is the main cause of the tsunami (Bao Chenglan, 2005), but not all the undersea earthquake could trigger a tsunami. Generally speaking, most of the undersea earthquakes do not trigger a tsunami. Chen Yong and Chen Qifu think that the occurrence of seismic tsunamis is generally controlled by three conditions (Chen Yong et al., 2005), including deep water, large earthquake and shallow coastal condition. Considering Chen Yuntai's point of view (Chen Yuntai et al., 2005), the tsunami occurrence conditions can be summarized as the following three points:

Seismic fault condition: Tectonic earthquake is the main type to generate the tsunami. The earthquake must cause significant vertical deformation of the seafloor for the tsunami to occur;

Water depth condition: The earthquake in the deep water is more prone to trigger the tsunami;

Magnitude, focal depth conditions: Tsunamis are more likely to happen from shallower and larger earthquakes than deeper or smaller ones.

Received on Aug. 7, 2014

Corresponding author: houjingming1982@126.com

From the point of the fault condition, there may be some similar features in terms of faults which can generate the tsunami, while focal mechanism solution can directly reflect the characteristics of crustal fault activity (Zheng Zhonghua et al., 2006). Therefore, this paper collects the global CMT data and tsunami event data from America's National Oceanic and Atmospheric Administration (NOAA), compares and statistically analyzes the seismic source parameters of tsunami events from 1976 to 2010.

1 Data information

The CMT centroid moment tensor data from the Harvard University began to be published in the late 1970s, providing global earthquakes whose magnitude is above 5. The CMT data is primarily obtained from the long-period teleseismic body wave data and mantle wave information. After analyzing the global earthquake catalogs from Harvard, USGS and ERI, Helffrich considered that the integrity of the CMT catalog was the best (Helffrich, 1971). The CMT data is in the NDK (ASCII) format, with each seismic event in 5 rows, each row of 80 characters. The data provides the parameters including the seismic moment and magnitude, fault plane parameters, stress axis, focal depth, centroid depth and moment tensor, and so on, covering a total of 33866 seismic events from 1976 to 2010.

The tsunami data, an excerpt of the tsunami event database from 1976 to 2010, are from the global tsunami database of U.S. National Geophysical Data Center (World Data System, 2012). The data include the year of tsunami disaster, latitude and longitude information, the tsunami wave height, tsunami type, tsunami credibility grade and other information.

2 Data statistical analysis

This article screens the highly credible tsunami disasters from the data, removes the uncertain events and any data in the conflict. A total of 278 tsunami events are shown in Fig. 1, and the black line in the figure is on behalf of the plate boundary.

In order to discover the similar characteristics of the tsunamigenic earthquake sources, this paper not only counts the focal mechanism solutions of 278 tsunami earthquakes, at the same time also statistics of the focal mechanism solutions of tsunamis with the wave height of 1 meter above are made. According to the "storm surge, waves, tsunamis and sea ice disaster contingency plans" issued by the State Oceanic Administration, tsunami warning has four levels. Level 1 corresponds to particularly

significant tsunami disaster, and the other three respectively correspond to major tsunami alert, large tsunami disaster and general tsunami disaster. When tsunami of more than 1 m occurs, larger tsunami disaster may appear. 75 larger tsunamis are counted, shown in Fig. 2.

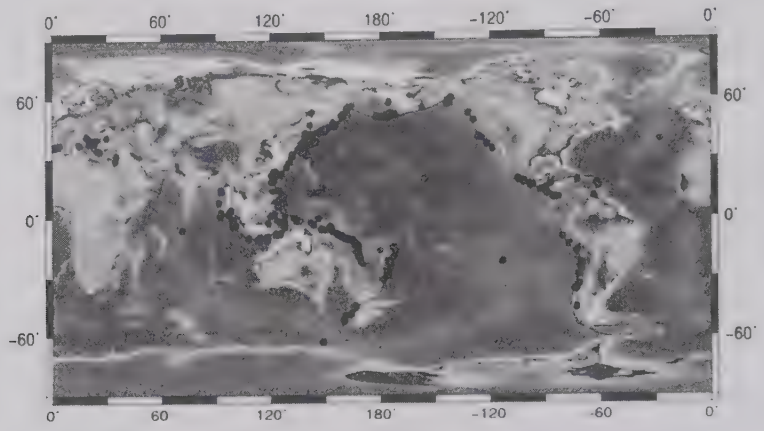

Fig. 1 Distribution of tsunami events

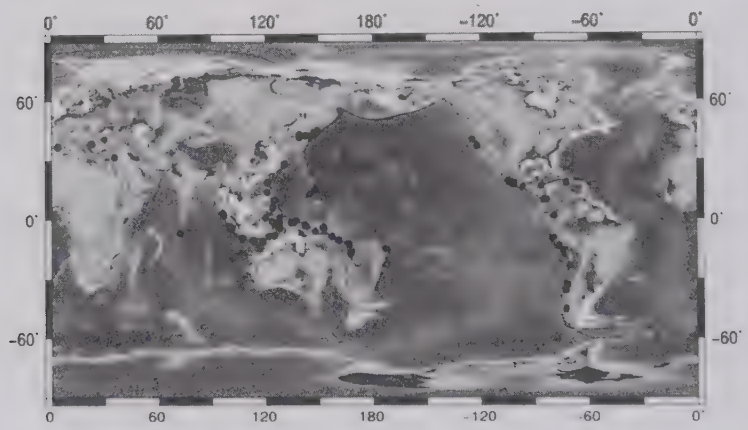

Fig. 2 Distribution of larger tsunami events

As you can see from Fig. 1 and Fig. 2, the tsunami event occurs mostly near the border of the sea and land plates, because the earth's crust of these regions is active. This paper compares and statistically analyzes the magnitude, the fault plane, principal stress axes, focal depth, the seismic moment tensor and regional characteristics, et al.

2.1 Magnitude

The CMT seismic moment tensor data contain three parameters related to the magnitude, body wave magnitude (M_b), surface wave magnitude (M_s), and the seismic moment (M_0). Seismic moment M_0 can be used to calculate the moment magnitude M_w, and the calculation formula is as follows:

$$M_W = (2/3)\log_{10} M_0 - 10.7$$

The moment magnitude is a new magnitude scale, which reflects the earthquake fault area and dislocation size. Body wave magnitude, surface wave magnitude, and other several magnitude scales only measure the energy of seismic waves, while seismic wave energy is often the only part of the total energy released by an earthquake. Starting from the seismic fault, the moment magnitude directly responses to the total energy released by an earthquake, and the so-called magnitude saturation problem does not exist. For the tsunami, the tsunami energy is from the total energy released by an earthquake fault. Therefore, moment magnitude is more suitable for the tsunami research than others.

After statistics, the moment magnitudes of larger tsunami events are between 5.3 and 9.0, and the superiority distribution are between 6.5 and 8.5. In the tsunami database, the smallest tsunamigenic earthquake magnitude is M_S 3.7 (Ye Lin et al., 2006). It's generally believed that earthquakes more than 6 can trigger tsunamis, and the statistics prove that earthquakes more than 3.7 can trigger tsunamis.

2.2 Fault plane

Displacements caused by undersea earthquakes are usually calculated based on faults elasticity theory. The theory was put forward by the Mansinha and Smylie (Mansinha et al., 1971) in 1971, assuming a rectangular fault plane buried under a semi-infinite elastic surface. When an earthquake occurs, with the stress beyond the maximum elastic of earth's crust, the crust will fracture along the fault plane, and the release of the accumulated stress will make the formation of an earthquake. The main parameters that describe the fault plane are strike, dip and slip angle, shown in Fig. 3. Fault plane is assumed as a rectangular area of plate interface on the foot block and the top and bottom edges of the fault plane are parallel to the mean Earth surface. Strike angle is the angle measuring clockwise from the local north to the strike direction, and the range is from 0 to 360 degrees. Dip angle is the angle between the mean earth surface and the fault plane, measured from the mean earth surface down to the fault plane, and its range is 0-90 degrees. Slip direction is described as the direction in which the hanging block moves relative to the foot block on the fault plane. Slip angle is the angle measured counter-clock-wise from strike direction to slip direction on the fault plane with the range from -180 to 180 degrees.

The CMT data provide two P-wave nodal plane, but do not tell which one is the actual fault plane. To identify which is the fault plane, other relevant information of source is

needed, such as surface rupture data, spatial distribution of aftershocks. Because there is not enough data, both of the two nodal planes are studied in this paper. After statistics, we find that strike angle distributes in every angle domain, and this is due to the earthquake distribution in different faults. Dip and slip angle are plotted in four quadrants and listed in the Tab. 2. It can be seen from the table the slip angle within the range of 0 to 360 degrees, dip angle distributes in the range of 0 to 90 degrees, and there are no obvious features.

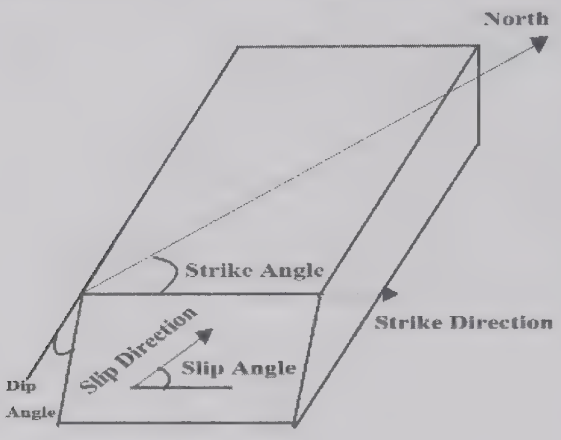

Fig. 3 Sketch of fault parameter definitions

Tab. 1 Statistics of slip angle and dip angle

	Fault plane 1	Fault plane 2	Fault plane 1 of larger tsunami	Fault plane 2 of larger tsunami
Slip angle (-180°to 180°)				
Dip angle (0°to 90°)				

2.3 Principal stress axes

According to the way of the fault rupture, earthquake fault can be classified as three main types, normal faults, reverse faults and strike-slip fault. Different types reflect different seismic stress states, and the earthquake is triggered by the dynamic stress of fault movement, therefore, the stress state is an important aspect of earthquake research studies. In the focal mechanism solutions, P, T and N axis are used to describe the stress state of faults. In the CMT data, each axis contains three parameters, eigenvalue, plunge and azimuth. We can classify these faults by these three parameters, according to Wang Hui's fault type classification method (Wang Hui et al., 2005).

Tab. 2 Statistics of fault types

Fault types	Ratio of tsunamis	Magnitude range	Ratio of larger tsunamis	Magnitude range of larger tsunamis	Runup of tsunami (m)
Strike-slip fault($P_{plunge}<45°$, $T_{plunge}<45°$)	21%	(5.3,8.1)	20%	(5.3,8)	(1,7.6)
Normal fault($P_{plunge}>45°$)	16%	(4.9,8.3)	16%	(6.3,8.3)	(1,22.35)
Reverse fault($T_{plunge}>45°$)	63%	(5.4,9)	64%	(5.7,9)	(1,54)

As can be seen from Tab. 2, the reverse fault type is the main type, accounting for 63% of the total. Reverse faults in magnitude and tsunami wave run-up height are slightly superior to strike-slip faults and normal faults, and this results from that the reverse type earthquakes release larger energy. The proportion of normal fault type is 16%. Existing theory suggests that the earthquakes which have the vertical displacement can trigger tsunamis, but the statistics show that strike-slip earthquakes also can trigger tsunamis, even bigger tsunamis, and this type accounts for 20%. This shows that pure strike-slip faults also can produce seafloor uplift and fall, which may be not stronger than the pure dip-slip faults, but it is still possible to stimulate tsunamis.

2.4 Centroid depth and focal depth

Focal depth is one of the basic parameters of the seismic source, which is of great importance to understand the tectonic background of seismic energy gathering and release. It is generally believed that shallow undersea earthquakes can trigger tsunamis more likely. The CMT data provides two depths, namely centroid depth and focal depth. The Centroid depth, which is from the waveform inversion, is equivalent to the depth of the fault plane center. The focal depth is determined by the Seismic phase positioning, equivalent to the depth of the fault rupture starting point. In this paper, these two depths are studied, the statistical results are shown in Tab. 3.

Tab. 3 Statistics of depth

Depth	Ratio	
	tsunamis	Larger tsunamis
centroid depth (<60km)	96%	99%
focal depth (<60km)	95%	97%

As can be seen from the Tab. 3, the tsunamigenic earthquakes are mostly shallow earthquakes (less than 60 kilometers), accounting for 97% of the total, mostly concentrated

in the distribution of 10 to 40 kilometers. The proportion of Shallow earthquake triggering larger tsunami reaches 99%, the advantage distribution concentrated in 10 to 35 kilometers.

2.5 Seismic moment tensor Mrr

The CMT data provide six seismic moment tensors, and Mrr is the first component of the seismic moment tensors. Physically speaking, compared with other components of the seismic moment tensors, Mrr is special because it contains the vertical movement information. The information of vertical movement reflects the change of potential energy, and potential energy changes can reflect the state of stress. Positive Mrr value is on behalf of compression, while negative Mrr value is on behalf of the state of tension (Wu Zhongliang et al., 2003). After statistics, about 70% of the seismic moment tensor Mrr is positive, and about 69% of the seismic moment tensor Mrr is positive in larger tsunami data.

Tab. 4 Statistics of moment tensor Mrr

	Tsunamis			Larger tsunamis		
	Reverse fault	Normal fault	Strike-slip fault	Reverse fault	Normal fault	Strike-slip fault
Mrr range	(0.32,9.55)	(-0.01,-9.96)	(-3.1,1.74)	(0.27,9.33)	(-1,-8.64)	(-1.07,1.74)

As can be seen from the table, reverse faults Mrr are positive, reflecting the compressed state, while normal faults Mrr are negative, on behalf of the state of tension. From the perspective of size, reverse faults Mrr are larger, reflecting the greater potential energy, corresponding to a possible larger tsunami.

2.6 Regional features

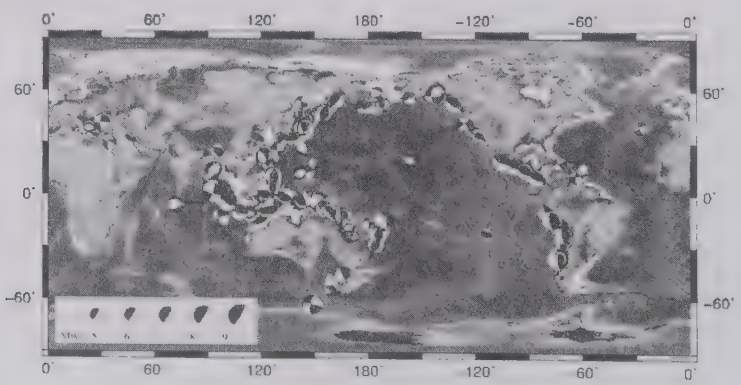

Fig. 4 Beach balls of focal mechanism solutions

Fig. 4 shows beach balls of focal mechanism solutions. It can be seen from the figure, beach balls of some areas are very similar, such as the west coast of South America, the West Coast of Central America. And there are areas showing beach balls kind of "messy" appearance, such as the coast of Japan and the Indian Ocean coast. Let's take the west coast of South America and the coast of Japan for example, to discuss regional characteristics of the tsunamigenic earthquake focal mechanism solutions.

As can be seen from Fig. 4, the strike angles, dip angles and slip angles of the west coast of South America are very close, indicating the direction of plate motion relatively fixed in these areas. In Tab. 5, the reverse fault is the main type in this area, very different from its natural probabilistic earthquake. These results can be used as an important basis to determine whether the tsunami can take place in the region.

Tab. 5 Statistics of fault types along the west coast of South America

Fault types	Ratio	
	Natural probabilistic earthquake	Tsunamigenic earthquake
Strike-slip fault($P_{plunge}<45°$, $T_{plunge}<45°$)	18%	7%
Normal fault($P_{plunge}>45°$)	41%	7%
Reverse fault($T_{plunge}>45°$)	41%	86%

Tab. 6 Statistics of fault types along the coast of Japan

Fault types	Ratio	
	Natural probabilistic earthquake	Tsunamigenic earthquake
Strike-slip fault($P_{plunge}<45°$, $T_{plunge}<45°$)	17%	13%
Normal fault($P_{plunge}>45°$)	21%	12%
Reverse fault($T_{plunge}>45°$)	62%	75%

It can be seen from Tab. 6, the reverse faults are also the majority in the Japanese coast, but the difference with its natural probabilistic earthquake is smaller. And the strike angle, dip and slip angles differ from one another, indicating the region's complex plate motions. Thus, to judge whether the tsunami can take place along the coast of Japan only from focal mechanism solutions is difficult.

3 Summary

This article statistically analyzes the worldwide tsunamis and focal mechanism

solutions from 1976 to 2010 in 25 years, from the perspective of whether the earthquake can trigger the tsunami. Statistics found that there exist some statistical features in focal mechanism solutions, such as the minimum magnitude of tsunamigenic earthquake of M_S 3.7; in the aspect of fault type, the reverse fault earthquake is the majority, 63%, and the percentage of strike-slip is not small, 21%; tsunamigenic earthquakes are mostly shallow earthquakes. Larger tsunami events have the similar statistical characteristics in terms of the source parameters, there is no big difference. In addition, the mechanism solution of tsunamigenic earthquakes in different regions has their own statistical characteristics. A detailed analysis of the focal mechanism solutions on a particular area can help to judge whether the earthquake could trigger a tsunami, and has the guiding significance to the tsunami disaster prevention and mitigation.

References

[1] Bao Chenglan. Tsunami Disaster and Its Pre-warning System [J]. Recent Developments in world seismology, 2005, (1): 14 - 18.

[2] Chen Yong, Chen Qifu. Sumatra earthquake tsunami and its related geophysical phenomena [J]. Progress in Geophysics, 2005, 20(1):112 - 117.

[3] Chen Yuntai, Yang Zhixian, Xu Lisheng. Tsunamis, earthquake-generated tsunamis and tsunamigenic earthquakes [J]. Physics，2005, 34(12): 864 - 871.

[4] Wang Hui, Zhang Guomin, Ma Hongsheng, et al. Seismicity of global tectonic systems obtained from Harvard CMT catalogue [J]. Seismology and Geology, 2005, 27(1): 44 - 54.

[5] Wu Zhongliang, Huang Jing, Zhang Dongning, et al. Seismic moment tensor element Mrr as a simplified representation of crustal potential energy change: its spatial distribution pattern and relation to the continental tectonic blocks in China[J]. Seismology and Geology, 2003, 25(1): 33 - 38.

[6] Yang Gangsheng, Zhao Genmo, Qiuhu. Oceanic Earthquake Disaster and Progress in its Research in China [J]. Marine Science Bulletion, 2000, 19(4): 74 - 85.

[7] Ye Lin, Wang Xinian, Bao Chenglan. Tsunami in the China seas and its warning service[J].Journal of natural disasters, 1994, 3(1): 100 - 103.

[8] Zhang Chaojun, Zhang Xiaodong, Miao Chunlan, et al. The analysis of the theoretical error of the accuracy of measuring the focal depth of near earthquake [J]. Earthquake research in China，2010, 26(2): 156 - 163.

[9] Zheng Zhonghua, Chen Yongshun. A tectonic stress of China and adjacent regions from earthquakes occurred during 2000-2004 [J]. Acta Seismologica Sinica, 2006, 28(3): 323 - 328.

[10] Helffrich G R. How good are routinely determined focal mechanisms Empirical statistics based on a comparison of Harvard, USGS and ERI moment tensors [J]. Geophys Jour Int, 1971,131: 741 -

750.

[11] Mansinha L, Smylie D E. The displacement fields of inclined faults [J]. Bull. Of the seismological Soc. of America, 1971, 61: 1 433 - 1 440.

[12] World Data System. Global Historical Tsunami Database. Boulder, CO, USA: National Geophysical Data Center, [2012-8-19]. http://www.ngdc.noaa.gov/hazard/tsu_db.shtml

海啸地震震源机制解统计

侯京明，徐志国

（国家海洋环境预报中心，北京，100081）

摘　要：近年来，全球海啸灾害频发，给人们带来了巨大损失。为了探索海啸地震发震时的规律，本文统计分析了 1976-2010 年的美国全球 CMT 地震矩心矩张量数据，并结合美国海洋与大气局的海啸灾害数据库，从海啸事件和较大海啸事件两个方面对震源机制解展开了对比统计分析，给出了海啸地震在震源方面的统计特征。

关键词：海啸地震；震源机制解；特征

Research on the influence of ocean temperature on XCTD profiler single-mode fiber transmission channel

ZHENG Yu [1], FU Xiao-hong [1], GAO Yu [1], FANG Jing [1], WANG Jin-hai [1]*, LI Hong-zhi [2], LIU Ning [2]

1. *Tianjin Polytechnic University, Tianjin* 300387, *China*

2. *National Ocean Technology Center, Tianjin* 300112, *China*

Abstract: XCTD, as one of the most important instruments for the deep sea exploration, is an important device for deep-sea hydrological data acquisition. But some difficult technical problems of traditional metal enameled wire channel have become the major bottleneck for XCTD development. Aiming at this problem, this paper puts forward with using single-mode fiber as the transmission channel of XCTD. Firstly, this paper makes a brief analysis on the problems of using enameled wire as transmission channel faces. Secondly, it analyzes the advantages of the single mode fiber technology. Finally, it makes theoretical research and experimental verification of the influence of seawater temperature change on the optical fiber transmission channel. The experimental results show that the error rate at the transmission rate of 10 MB/S is 0, and the loss can be negligible when the single-mode fiber channel is used in the sea water and the seawater temperature changes from 0 to 20℃. This method will greatly increase the rate of signal transmission and the transmission stability. And this paper shows that using the single-mode fiber as the transmission channel of XCTD has certain feasibility.

Keywords: XCTD profiler, signal-mode optical fiber, effect of ocean temperature, transmission performance

1 Introduction

XCTD(Expendable Conductivity Temperature Depth)probe, is one of the most important instruments for deep sea exploration. It falls at a speed of 3 - 5 m/s, and collects the real time information of conductivity, temperature and depth, and then transmits the collected information to the ocean parameter measuring instruments aboard the boat in the real time by means of wire transmission to complete the drawing of water conductivity,

Received on Aug. 7, 2014

*Corresponding author: wangjinhai@tjpu.edu.cn

temperature and depth profile. The ocean hydrological data measured by XCTD is widely concerned because of its importance for marine science as well as the military.

The transmission channel of XCTD data is a single enameled line which is wrapped around the spool with two-wire insulation coating layer. The enameled wire is unfolding with the sinking of probe gradually and transmitting the electrical signal. The simplified working process is shown in Fig.1. The signal channel is a complex filter system with dynamic changes, because of the distributed capacitance of channel and the dynamic performance of winding inductance as well as some parasitic parameters induced by ocean environment. So the transmission rate of system and the transmission accuracy of signal are limited.

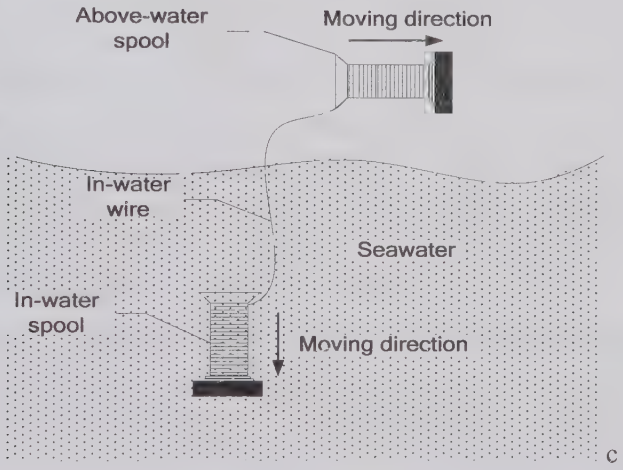

Fig. 1 Simplified schematic diagram of the XCTD process

Firstly, the weak conductance of the sea and the coupling capacitance effect of transmission line attached to the channel make the channel more complicated. At the same time, with the unfolding of the transmission line, the distributed capacitance and inductance parameters change in the real time. All of these make the signal transmission difficult to achieve by using the method of impedance matching.

Besides, in consideration of the change of channel parameters, if a single frequency sine signal is used for transmission, the signal will be filtered completely at the stop band. If digital transmission is used, there will be some signal that cannot be filtered and will be transported, since the digital signal can be seen as a sum of basic frequency and high-order harmonics. But different time channels have different phase delays for the signal, thus the superposition signal cannot be used to demodulate information correctly

when arriving at the terminal. Secondly, XCTD as an expendable measuring instrument cannot provide high power, and the signal transmission power of the channel cannot be improved by joining the repeater, so the signal of terminal is very week. Moreover, the existence of the ocean ambient noise and induction electromotive force induced by coil cutting magnetic in the falling process will also reduce the signal transmission quality. These reasons make the final signal be unidentified. Combined with these reasons, it is difficult to realize high speed and stable transmission of XCTD data by using enameled wire, which is the main bottleneck in the process of the development of XCTD currently.

Aiming at the limitations and problems that enameled wire channel has faced in the XCTD work environment, this paper presents a new transport channel-single-mode fiber. The basic idea is to replace the metal wire with the single mode fiber and change the electrical signal into the optical signal, which can avoid some of the electrical signal transmission problems. Compared with the traditional metal enameled wire, the single-mode fiber has many advantages, such as ultra high bandwidth in hundreds of GHz, only 0.3 to 0.6 dB/km losses in normal transmission, light weight, and strong anti-interference ability. In terms of price, according to the survey of Infostone Communication Consultant Ltd, the average price of the single mode fiber G652 produced by domestic major manufacturers in 2010 was about 74 yuan / km, about 71 yuan / km in 2011, about 69 yuan / km in 2012, and about 68 yuan / km in 2013. The price decreases year by year, and will be lower when it comes to the prime cost. The price of basic optical receiving and transmitting module, such as TOSA/ROSA, is only 5 to 20 yuan. Applying the fiber channel will not cause too much increase in the cost of XCTD device and will make the transmission distance and rate greatly improved. It has the extremely vital significance to the development prospect of XCTD. Therefore, using the single-mode optical fiber instead of the metal enameled wire as a transmission channel of XCTD has certain feasibility.

This new transmission mode could also face some new problems, such as the effects of seawater and temperature focused on in this paper to the single-mode fiber transmission. First of all, many studies have shown that hydrogen loss, which is mainly due to hydrogen ions and hydroxide ions, is one of the main causes for the fiber loss. When the H^+ or OH^- crosses the cladding of fiber and penetrates into the core area, they may combine with the cracked bonds of $Si\text{-}O$ or $Ge\text{-}O$ and generate $Si\text{-}OH$, $Si\text{-}H$ or $Ge\text{-}OH$ molecular structure which will absorb light energy to generate vibration and result in the loss of light. Different molecular structures have different absorption in the range and size of optical wavelength. The maximum absorption of $Si\text{-}OH$ in light is at the wavelength of 1 383 nm and $Ge\text{-}OH$ is at 1440nm. When it comes to $Si\text{-}H$, the wavelength is 1 530 nm. The

great existence of H^+ and OH^- in sea-water environment is bound to affect signal transmission in the single mode fiber. Secondly, along with the increase of water depth in the marine environment, water temperature is the ladder type distribution and the temperature change is generally in the range from 0 °C to 30 °C. With the continuous increase in water depth, the temperature would decrease gradually. Under normal circumstances, below the water depth of 100 meters, water temperature will not exceed 20 °C. But at the depth 1000 m, the water temperature will gradually approach to 0 °C and will tend to be stable. Therefore, this paper discusses these two keys.

2 Mechanism of the effect of temperature on the fiber channel signal transmission

Only one mode of signal can be transmitted in the single-mode fiber, namely the basic mode signal LP_{01}.It can be considered as the fundamental mode which is composed of two mutually orthogonal polarized signals. In the ideal case, these two polarized mode signals have the same transmission characteristics, namely the mode-degeneracy. But some objective external factors will destroy this degeneracy, which make the transmission constant of two polarized mode signals no longer the same and eventually lead to PMD(polarization mode dispersion) in the single mode fiber. PMD will produce error in the transmission of information. Many literatures indicate that PMD, which is sensitive to temperature, is a function of temperature. And temperature changes will lead to the loss of the fiber changes.

Assuming that the linearly polarized light incident to single-mode fiber is $E(0)$, it can be regarded as two mutually orthogonal polarized components $E_x(0)$ and $E_y(0)$ .Their relationships are shown in Eq. (1).

$$\begin{cases} E_x(0)=E(0)\cos\varphi \\ E_y(0)=E(0)\sin\varphi \end{cases} \tag{1}$$

where φ is the angle between the incident light and the *X* axis. Through a length of single-mode fiber *L*, two polarized components can be obtained at the output terminal shown in Eq. (2).

$$\begin{cases} E_x(L)=aE_x(0)\exp(j\beta_x L)+bE_y(0)\exp(j\beta_y L) \\ E_y(L)=aE_y(0)\exp(j\beta_y L)+bE_x(0)\exp(j\beta_x L) \end{cases} \quad (2)$$

where *a* and *b* are coefficients of polarization components at the output as the incident light through the length *L* of single mode fiber. β_x and β_y are the change rates of polarized angle of incident light on the X and the Y axis through unit length fiber. The field strength detected in the output is as follows:

$$E(L)=E_x(L)\cos\gamma+E_y(L)\sin\gamma \quad (3)$$

The output light intensity is described in Eq. (4).

$$I(L)=E(L)\times\dot{E}(L)=A+B\cos(\Delta\beta L) \quad (4)$$

$$\Delta\beta=\beta_x-\beta_y=n_x k-n_y k=(n_x-n_y)k=2\pi\Delta n/\lambda \quad (5)$$

$$A=[\alpha\cos\gamma+b\sin\gamma]^2E(0)^2\cos^2\varphi+[\alpha\sin\gamma+b\cos\gamma]^2E(0)^2\sin^2\varphi \quad (6)$$

$$B=[2ab-4ab\sin^2\gamma+2(a^2-b^2)\sin\gamma\cos\gamma]\times E(0)^2\cos\varphi\sin\varphi \quad (7)$$

Generally, the PMD coefficient is used to measure the polarization mode dispersion in the fiber. It can be calculated through Eq.(8).

$$PMD=\frac{\Delta\tau}{\sqrt{L}}(ps/\sqrt{km}) \quad (8)$$

where *L* is the transmission distance and its unit is km. $\Delta\tau$ is the transmission delay of two polarization components in single mode fiber. Its unit is ps and the expression is shown in Eq. (9).

$$\Delta\tau=\frac{\Delta v\quad L}{v^2} \quad (9)$$

where v is the transmission speed of light in the fiber:

$$v=\frac{c}{n} \quad (10)$$

c is the speed of light in vacuum, and n is the refractive rate of optical fiber core. Their relationship can be obtained by the calculation of Eq.(11).

$$\Delta v = \frac{c\Delta n}{n^2} \tag{11}$$

The changes of polarized mode constant β_x and β_y that accompany the single-mode temperature changes will cause the variation of difference of two polarized mode constant $\Delta\beta$. By the Eq.(4) we can infer that the changes of $\Delta\beta$ will change the output light intensity and the fiber loss. And from the Eq.(5), it can be seen that the change of $\Delta\beta$ will make Δn changes. The followed changes of Δv and $\Delta\tau$ will result in PMD coefficient change.

3 Test of effects of seawater on the single-mode fiber channel signal transmission

In the research of the influence of sea-water temperature change on the single-mode optical fiber transmission, it mainly uses the experimental method to test. In order to ensure the test process to be real, instead of putting fiber into the temperature control box directly and changing the air temperature, the experiment puts fiber in the sea and through the sea-water temperature control method to measure. So it needs to test the optical signal transmission capability of single-mode fiber in the seawater to learn the effect of seawater immersion on the single-mode fiber.

This paper uses the Corning SMF-28 single-mode optical fiber current widely used as the experimental object. The 3 km long single mode fiber is selected, with one terminal connected with the light source (AV38126A) and the other terminal connected with optical power meter (FDD-1205), immersed in 25 °C water .The 1 310 nm wavelength and 1 550 nm wavelength are the most frequently used in single-mode fiber communication to experiments. Taking into account the actual maximum measured depth of XCTD from 2 000 to 3 000 m and the falling speed from 3 to 5 m/s, the XCTD maximum working time is less than 30 min.

The light source is turned on to get stable light output 2 hours later and data are recorded every 5 mins. Experimental results of 1 310 nm wavelength (Fig. 2a) and 1 550 nm wavelength (Fig. 2b) are obtained as shown in Fig. 2 by several experiments for the average to remove the random errors. When the fiber isn't immersed in the water, the optical power output of 1 310 nm is -2.343 dBm, and 1 550 nm is -4.228 dBm.

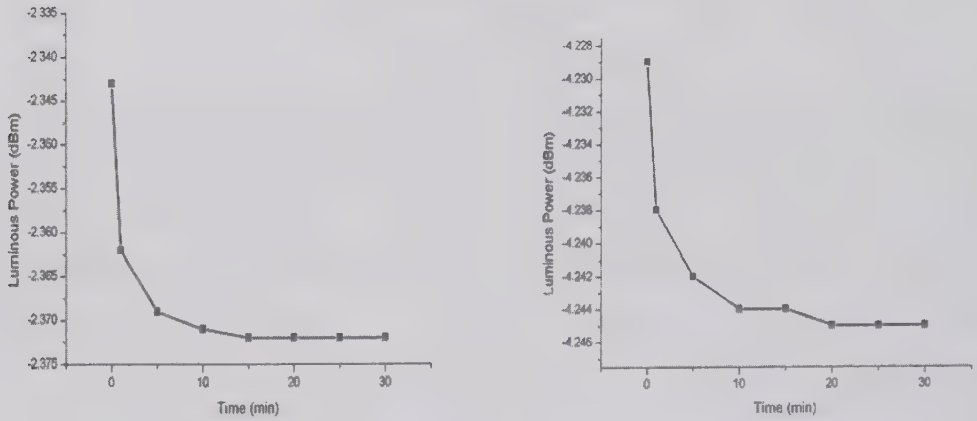

Fig. 2 Single-mode fiber immersion test results

(a) Output of 1310 nm, (b) Output of 1 550 nm

To be able to clearly see the power change trend after the fiber is immersed into the water, the output optical power uses the dBm as the unit of measurement. Their conversion is shown in Eq. (12), where P is the luminous power and its unit is mW.

$$dBm = 10\log P \tag{12}$$

The experiment results show that, in the first 10 mins after immersing the fiber in water, it will cause slight loss due to the factor of water. After 10 mins later, the receiving optical power is basically stable and almost no longer increases. While the water will cause the loss of optical fiber transmission, but this loss is very small. The optical power of 1310nm changes from the initial -2.343dBm (582.9 μ W) to -2.371dBm (579.2 μ W), and the change rate is only 0.63%.When it comes to 1550nm,with the optical power changing from the original -4.229 dBm (377.6 μ W) to -4.244 (376.3 μ W), the change rate is only 0.34%. From these negligible changes, the conclusion can be drawn that the immersion of water in single temperature conditions almost can't directly impact the transmission of single-mode fiber.

4 Test of different temperature on single-mode fiber channel signal transmission

Based on the above analysis, the test system, which is shown in Fig. 3, has been set up to test the influence of ocean environment temperature on the single-mode fiber transmission performance. The 3 km length fiber spool is put into high-precision, fluctuation amplitude smaller than 0.05%, and temperature can be controlled in the water

tank. It is filled up with South China Sea sample solution and be measured in the real time way by the temperature measuring bridge AT-1B. The temperature control system of water tank automatic closed loop controls its temperature in a specified temperature range according to the measurement of temperature measuring bridge. Because the temperature range of deep sea water concentrates in 0 to 20 °C, this experiments measure data transmission and the optical power loss of the fiber in every 1℃ increase from 0 to 20 °C.

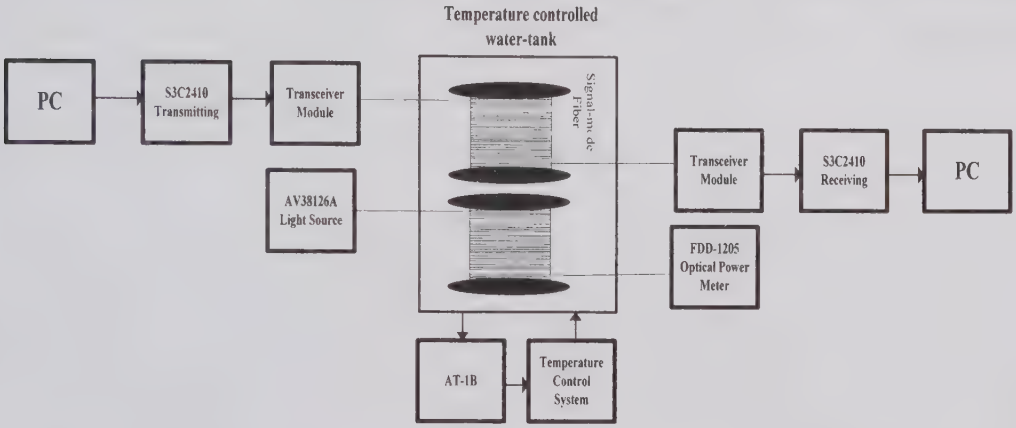

Fig. 3 The experimental device for testing temperature influence on single-mode fiber

In order to learn the effect of temperature on single-mode fiber optical power loss, at each temperature measurement point, 1 310 nm and 1 550 nm wavelength continuous light is sent in one terminal of single-mode fiber spool through light source AV38126A, and output luminous power in the other terminal is measured through optical power meter FDD-1205.The measurement results are shown in Fig. 5.

Experimental results show that, at the abyssal temperature concentration ranging from 0 to 20 °C, the luminous power loss of fiber caused by temperature is slight. Only in the situation of selecting μW as a luminous power unit, the slight difference can be seen. But the maximum change value of 1 310 nm wavelengths light in different temperature points is 0.087 μW, which is about equal to 1.3% of the minimum output power. To 1 550 nm wavelengths light, it is 0.035 μW, which is about equal to 0.6% of the minimum output power. The loss of luminous power in the fiber due to temperature changes almost can be ignored.

For the immediate consequence of signal-mode fiber PMD due to the factor of temperature has few errors, the method of measuring bit error is used to learn about the effect of temperature changes on the dispersion of single-mode fiber. In each of the temperature measuring point, S3C2410 is used as control CPU to send 100 groups of fixed

data (approximately 146 MB) which consist of 1500 Byte in each group, through the web interface in the rate of 10 MB/S(the enameled wire is 800 to 1000 bit/s) to detect the error. Finally, PC calculates the error number by comparing the obtained data and the original data and displays it on the screen. In the actual test, there is no error code been detected in the process of temperature rising from 0℃ to 20℃. So, the conclusion can be drawn that, in the actual situation of XCTD work, the influence of water temperature change on the dispersion of the single-mode is almost neglected.

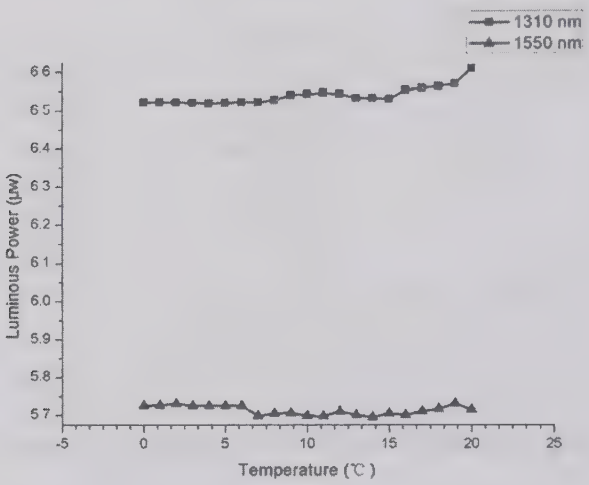

Fig. 4 The experimental results of temperature influence on the optical fiber

5 Conclusions

XCTD as one of the most important instruments of deep-sea measurement plays an important role in marine surveying. But for the complexity of the marine environment and the dynamic impedance characteristics of varnished wire spool in the falling process, the signal transmission becomes a key problem. This paper puts forward to selecting the single-mode fiber, whose diameter approximates enameled wire, as the transmission channel of XCTD and does some theoretical and experimental researches for the influence of temperature change on the single-mode fiber channel. The results show that in the temperature range of deep ocean environment, the influence of temperature change on dispersion and loss of the single-mode fiber is slight, and using the single-mode fiber instead of the enameled wire as the transmission channel of XCTD is feasible. In the follow-up research, we will perform further in-depth analysis of the influence of the XCTD working environment on the single-mode fiber transmission and make it really used in XCTD R & D to solve the existing channel problems. The method provides a new idea for

XCTD data transmission, and also has reference significance for similar products such as XBT and XCP. The new channel provides a broader development space for the high speed, large depth and high stability development of XCTD.

Acknowledgments

This research was supported by the Research Program of Application Foundation and Advanced Technology of Tianjin (No. 14JCYBJC16300), the National Natural Science Foundation of China (No. 41206031).

References

[1] JiaZhicheng, Yu X S, et al. Design and implementation of data transmission circuit for XCTD profiler[J]. Ocean Technology, 2010, 29(22):1-4.

[2] Wu Yuhua. Research on XCTD calibration method[J]. Ocean Technology, 2007, 26(2):14-16.

[3] Zheng Yu, Li H Z, et al. Modeling and calculation of distributed capacitance between the transmission lines of underwater XCTD profiler[J]. Marine Science Bulletin, 2013, 3(32):332-337.

[4] Zheng Yu, Zhao X, et al. The analysis of time-varying channel effects on transmission performance of deep-sea abandoned measuring instrument[J].Acta Phys. Sin, 2014, 64(4):1-8.

[5] Zhang Zili. Theory research and application of ocean electromagnetic field[D].Beijing: China University of Geosciences, 2009.

[6] Zhang Qisheng. Development of the expendable current profiler[J]. Chinese Journal of Geophysics, 2013, 56(11):3769-3707.

[7] Tao Zhiyong, Cai J. The periods of optical fiber technology development in China[J]. Optical Communication Technology,1(3):59-61.

[8] Zhao Yong, Meng Q Y. Effect of physical and chemical reactions between hydrogen and optical fiber on permanent downhole measurement[J]. Opto-Electronic Engineering, 2007, 34(9): 55-65.

[9] Wang Qiang, Song Jun, et al. Evaluation of low water peak fiber life in hydrogen loss[J]. Jiangsu: Chinese Communication Association, 2006, 31(2):139-146.

[10] B W Hakki. Polarization Mode Dispersion in a Signal Mode Fiber[J]. Journal of Lightwave Technology, 1996, 14(10):2202-2207.

[11] Shi Huiping, Cheng S L. Effect of temperature on polarization mode dispersion in signal mode optical fiber[J]. Optical Communication Technology, 2000, 24(1):37-39

水温对 XCTD 剖面仪单模光纤传输信道影响的研究

郑 羽[1]，付孝洪[1]，高 宇[1]，方 静[1]，王金海[1*]，李红志[2]，刘 宁[2]

（1. 天津工业大学 电信学院，天津 300387；2. 国家海洋技术中心，天津 300112）

摘 要：XCTD 作为深海探测的一种最为重要的仪器，是深海水文数据获取的重要手段，但传统的金属漆包线信道存在一些难以解决的技术问题，成为 XCTD 发展的主要瓶颈。针对这一问题，本文提出采用单模光纤作为 XCTD 的传输信道。本文首先对使用漆包线作为传输信道所面临的难题进行了简要的分析；其次，分析了单模光纤技术优势；最后，针对 XCTD 工作环境中海水温度变化对光纤传输信道带来的影响进行了理论研究和实验验证，实验结果表明，单模光纤信道在海水介质及 0 ～ 20° 海温变化下，以 10 MB/S 的传输速率传输数据时误码率为 0，且损耗变化几乎可以忽略，大大提高了信号传输的速率和传输稳定性，实验结果说明采用单模光纤作为 XCTD 的传输信道具有一定的可行性。

关键词：XCTD 剖面仪，单模光纤，海洋温度效应，传输性能。

Pollution status and potential ecological risk assessment in the surface sediments of the Yellow River estuary

ZHANG Ya-nan[1, 2], HE Qing [2], JI Wei-dong [2], ZHANG Qi [1*]

1. *Institute of Seawater Desalination and Multipurpose Utilization, SOA, Tianjin* 300192, *China;*

2. *Third Institute of Oceanography, SOA, Xiamen 361005, China*

Abstract: Based on the "Project 908" survey data in 2006–2007 on surface sediments of the sea area adjacent to the Yellow River estuary, the research was conducted on the concentration distribution characteristics of heavy metals in surface sediments of the estuary, which show that the mean contents of seven heavy metals (Cu, Pb, Zn, Cd, Cr, Hg, As) in the Yellow River estuary and its surrounding areas all comply with the Level-I of National Marine Sediments Quality Standard of China. Statistically significant correlation between the elements Cu-Cd, Pb-Cr and Cr-As in sediments indicates that the two heavy metals in each group may respectively have similar geochemical properties and sources. By using the Potential Ecological Risk Index (PERI) proposed by Hakanson, the assessment shows that the potential ecological risks in the estuary surface sediments are mainly attributed to Cd and Hg. The biological toxicity effects are assessed with the biological effects of concentration method, resulting in a conclusion that the adverse effects of As on organisms in the estuary marine environment occasionally occur, in contrast, Cu, Pb, Zn, Cd, Cr and Hg will not generate adverse biological effects on a short and medium time scale.

Keywords: Yellow River estuary, heavy metals, pollution risk assessment

1 Introduction

As a result of long-term accumulation and enrichment through absorption and precipitation, the concentrations of heavy metals in sediments are relative stable. Therefore, the study on the distribution of heavy metals in sediments and their pollution assessment is more representative. Assessment of the pollution level of heavy metals in sediments functions as the major reference for river basin environmental quality assessment and for the prevention and control of environmental pollution. As the second largest river in China, the Yellow River ranks top in silt concentration level in the world,

Received on Jun. 19, 2014

*Corresponding author: zqhaoyun@163.com

known as “less water and heavy load of silt”（Pang and Si, 1979）. According to *2012 Bulletin of Marine Environmental Quality of China* (State of Chinese marine environment, 2012), in 2012 1166 t of heavy metal pollutants were discharged into the Yellow River.

Currently, there are many methods used to analyze and assess heavy metal pollution in sediments. Among them, direct comparison with marine sediment quality criteria is the most simple and intuitive way. In accordance with *Marine Sediment Quality* (GB18668-2002), the impacts of heavy metals in surface sediments in the Yellow River estuary are assessed in this paper. Besides, the potential ecological risks of the sediments are studied by using the Potential Ecological Risk Index (PERI) method proposed by Swedish scholar Hakanson in 1980(Hakanson, 1980). Through the analysis and calculation on the contents of heavy metal pollutants in sediments, it is feasible to obtain a certain metal’s pollution level and potential ecological risk in the sea area, as well as a variety of metals’ comprehensive pollution level and comprehensive potential ecological risk in the sea area.

Assessment on biological toxicity effects is conducted using the biological effects of concentration method which is built between the pollutant concentration in sediments and the biological effects produced under the concentration. The method is measured through two thresholds: respectively "effect range low" (ER-L) and "effect range median" (ER-M) (Long and Morgan, 1990). If the pollutant concentration is less than ER-L, the negative effects of the contaminant on organisms will not happen. Negative effects occasionally happen if the concentration is between the two thresholds. When the concentration is over ER-M, negative effects occur very often. The integrated utilization of the three evaluation means can bring about a clearer understanding on the heavy metal pollution conditions in sediments of the Yellow River estuary.

Based on the analysis of the “National Project: Offshore Marine environmental evaluation of China” (Project 908) survey data in 2006–2007 on seven heavy metal elements (Cu, Pb, Zn, Cd, total Cr, Hg, As) in surface sediments of the Yellow River estuary and its adjacent sea area, study and assessment were carried out on the distribution characteristics and pollution status of heavy metals in the estuary sediments, with the correlation between heavy metals revealed and discussed through mathematical statistic methods. The main potential ecological risks in the surface sediments were assessed with the use of the Hakanson PERI method, and the biological toxicity effects were evaluated with the biological effects of concentration method, thus providing a scientific basis for preventing heavy metal pollution in the Yellow River estuary and protecting the safety and health of marine ecological environment.

2 Materials and methods

2.1 Sampling locations

According to the "Project 908" offshore marine chemical survey, 23 sampling sites were selected for study in the sea area adjacent to the Yellow River estuary. Fig. 1 illustrates the layout of survey sites. Ball valve samplers were used for seawater collection and frog-style samplers for sediment collection. All samples were collected, preserved and pretreated in accordance with *the Specification for Marine Monitoring* (GB 17378-2007).

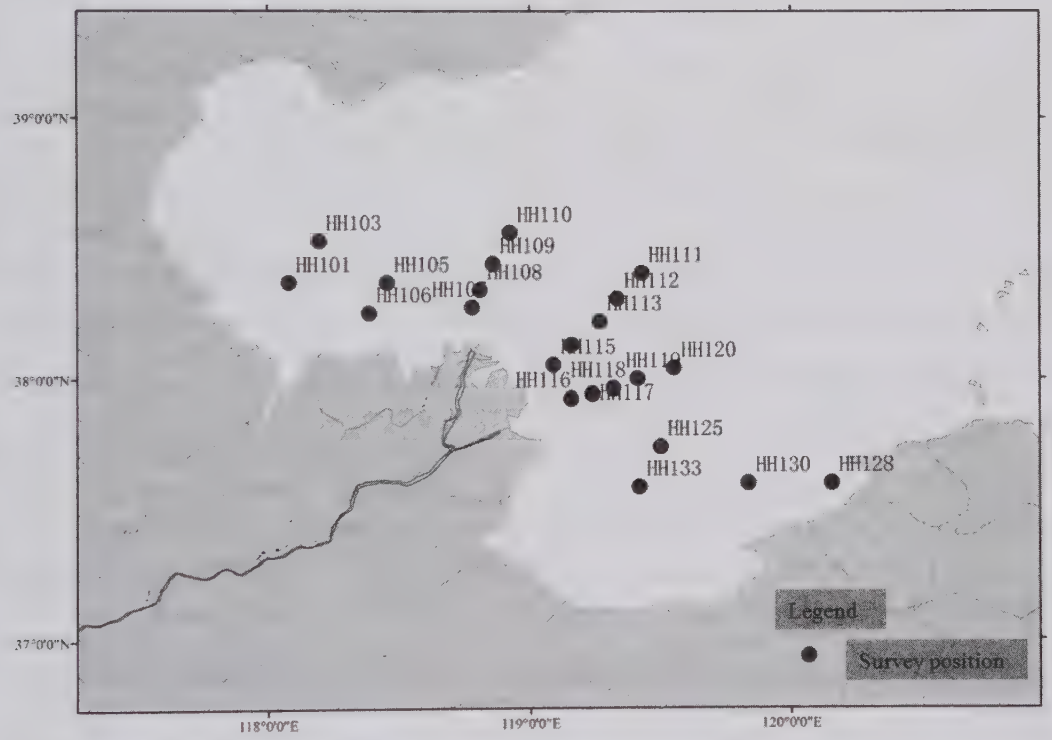

Fig. 1 Layout of survey sites

2.2 Analytical methods

The sediment monitoring program focuses on 7 kinds of heavy metal elements, including Cu, Pb, Zn, Cd, Cr, Hg and As. Among them, the contents of Cu, Pb, Zn, Cd and Cr are determined by the SOLAAR M6 atomic absorption spectrophotometer, while the contents of Hg and As are determined by the XGY-1012 atomic fluorescence spectrophotometer. All methods comply with *the Specification for Marine Monitoring* (GB

17378-2007).

2.3 Assessment methods

The impacts of heavy metals in marine sediments are assessed in accordance with the *Marine Sediment Quality* (GB 18668-2002); the potential ecological risks are estimated using the Potential Ecological Risk Index (PERI) method proposed by Hakanson; and the biological toxicity effects are evaluated with the biological effects of concentration method.

3 Results and analysis

3.1 Impact assessment of heavy metals in surface sediments

The impacts of heavy metals in marine sediments are assessed in accordance with the *Marine Sediment Quality* (GB 18668-2002). The results show that the contents of Pb, Zn, Cd, Cr, Hg and As in all 23 sites meet the Level-I of *National Marine Sediments Quality Standard of China* (NMSQSC); the contents of Cu in 3 sites (HH106, HH107, HH120) meet the Level-II of NMSQSC, with an over standard rate of 13.04%. The average contents of all kinds of heavy metals in the sediments of the Yellow River estuary comply with Level-I of NMSQSC, indicating the fact that heavy metal pollution is not serious in the estuary area.

3.2 Ecological risk assessment on heavy metal pollution in surface sediments

The estuarine sediments are the research subject in this paper. Under the condition of incomplete background data of estuarine sediments, the average background abundance in the river basin is selected as the background value of pollutants (Zhao and Yan, 1994). The 7 kinds of main pollutants, including Cu, Pb, Zn, Cd, Cr, Hg and As, are chosen as pollution parameters.

The calculation formula for the single pollutant's pollution parameter is as follows:

$$C_f^i = C^i / C_n^i$$

where C_f^i —— the pollutant's pollution parameter;

C^i —— the measured concentration of the pollutant in the substrate sludge;

C_n^i —— the background value of the pollutant in sediments;

The comprehensive pollution level C_d is the sum of a variety of pollutants' parameters,

and its calculating formula is: $C_d = \sum_{i=1}^{7} C_f^i$.

In this paper's study, relevant values raised by Hakanson are directly used as the toxicity coefficients of pollutants, for the reason that the coefficients derived through normalization processing according to the principle of abundance objectively reflect the impacts of pollutants on the environment.

Tab. 1 Pollutants' toxicity coefficients

Pollutants	Zn	Cr	Cu	Pb	As	Cd	Hg
Toxicity coefficients T_r^i	1	2	5	5	10	30	40

To quantitatively express the potential ecological risk of the single pollutant, the potential ecological risk parameter can be defined as: $E_r^i = T_r^i \bullet C_f^i$.

Where E_r^i—— potential ecological risk parameter;

T_r^i ——single pollutant's toxicity coefficient.

The potential ecological risk index *RI* is defined as the sum of potential ecological risk parameters of multiple pollutants.

$$RI = \sum_{i=1}^{7} E_r^i = \sum_{i=1}^{7} T_r^i \bullet C_f^i$$

In view of the potential ecological risk parameter of the single pollutant, the E_r^i of Cu, Pb, Zn, Cr, As is less than 40, which can be classified as the low risk level, with Zn and Cr having the lowest average E_r^i of around 1.0. In contrast, the potential ecological risk of Cd is obviously higher, and the E_r^i of 14 survey sites ranges from 40 to 80, accounting for 60.9%, which can be classified as the medium risk level; the E_r^i of 6 sites ranges from 80 to 160, accounting for 26.1%, which can be classified as the high risk level. The average E_r^i of Cd is 64.6, classified as the medium risk level. Moreover, the potential ecological

risk of Hg is even higher than Cd, and the E_r^i of 13 sites ranges from 80 to 160, accounting for 56.5%, which can be classified as the high risk level; the E_r^i of 6 sites ranges from 160 to 320, accounting for 26.1%, which can be classified as the very high risk level.

Tab. 2 E_r^i and *RI*

Index Type	Threshold Interval of the Single Pollutant	Potential Ecological Risk Level Classification
Eri	$E_r^i < 40$	LOW potential ecological risk
	$40 \le E_r^i < 80$	MEDIUM potential ecological risk
	$80 \le E_r^i < 160$	HIGH potential ecological risk
	$160 \le E_r^i < 320$	VERY HIGH potential ecological risk
	$E_r^i \ge 320$	CRITICAL HIGH potential ecological risk
RI	Threshold Interval of Seven Pollutants	Potential Ecological Risk Level Classification
	$RI < 130$	LOW potential ecological risk
	$130 \le RI < 260$	MEDIUM potential ecological risk
	$260 \le RI < 520$	HIGH potential ecological risk
	$RI \ge 520$	VERY HIGH potential ecological risk

In view of the comprehensive potential ecological risk index of multiple pollutants, the *RI* of 15 survey sites ranges from 130 to 260, accounting for 65.2%, which can be classified as the medium risk level; the *RI* of the rest 8 sites ranges from 260 to 520, accounting for 34.8%, which can be classified as the high risk level. The overall *RI* is mainly attributed to the potential ecological risks of Cd and Hg. Although the pollution level of Cu is also significant, its potential ecological risk is not prominent, owing to the fact that the toxicity coefficient of Cu is much lower than that of Cd or Hg.

3.3 Assessment on biological toxicity effects

The biological effects of concentration method are developed to assess the risks of heavy metals in sediments by using two thresholds: ER-L and ER-M. The United States Environmental Protection Agency (USEPA) has established a comprehensive database containing the biological effects of heavy metals in sediments, based on which the assessment is conducted in this paper to investigate whether the concentrations of heavy metals in regional sediments pose toxicity effects on environmental organisms. The ER-L/ER-M (mg/kg, dry weight) of Cu, Pb, Zn, Cd, Cr, Hg and As are 34/270, 46.7/218,

1.2/9.6, 150/410, 81/370, 0.15/0.71 and 8.2/70, respectively. Tab. 4 illustrates the average concentration of every heavy metal and the threshold concentrations of biological toxicity effects in the study area's sediments.

Tab. 3 E_r^i and *RI* in sediments

Survey Site	Eri Cu	Pb	Zn	Cd	Cr	Hg	As	RI	Potential Ecological Risk Classification
HH101	3.1	4.7	0.3	24.7	0.8	99.1	5.2	137.8	MEDIUM potential ecological risk
HH103	14.1	13.0	0.9	102.5	1.8	100.9	15.5	248.8	MEDIUM potential ecological risk
HH105	11.4	7.5	0.5	54.7	1.5	76.2	9.7	161.5	MEDIUM potential ecological risk
HH106	12.1	3.3	0.4	85.2	0.6	57.7	9.8	169.1	MEDIUM potential ecological risk
HH107	13.6	8.3	1.2	90.4	1.3	94.0	10.2	218.8	MEDIUM potential ecological risk
HH108	9.6	7.4	0.9	61.0	0.9	45.4	19.3	144.5	MEDIUM potential ecological risk
HH109	9.4	7.0	1.1	79.2	1.1	154.5	19.7	272.1	HIGH potential ecological risk
HH110	7.5	6.2	0.8	85.2	1.1	126.7	22.4	249.8	MEDIUM potential ecological risk
HH111	11.3	8.7	1.3	70.6	1.0	171.9	20.2	285.1	HIGH potential ecological risk
HH112	4.4	6.7	1.0	42.4	1.0	118.8	12.9	187.2	MEDIUM potential ecological risk
HH113	9.1	10.0	0.9	63.1	0.9	110.2	22.2	216.5	MEDIUM potential ecological risk
HH114	6.9	5.9	0.9	59.1	1.5	236.2	11.6	322.2	HIGH potential ecological risk
HH115	15.2	8.6	1.6	85.0	1.9	155.6	16.3	284.2	HIGH potential ecological risk
HH116	4.7	4.9	0.8	35.3	0.6	95.8	15.7	157.7	MEDIUM potential ecological risk
HH117	9.8	6.9	0.8	58.4	1.2	189.8	8.0	274.9	HIGH potential ecological risk
HH118	7.8	5.1	0.9	42.9	0.9	208.4	15.8	281.7	HIGH potential ecological risk
HH119	9.1	5.0	0.9	58.9	1.0	254.5	20.0	349.4	HIGH potential ecological risk
HH120	19.3	6.6	1.5	113.3	2.1	279.6	14.5	437.0	HIGH potential ecological risk
HH122	10.8	7.4	0.6	53.9	1.3	62.8	15.3	152.1	MEDIUM potential ecological risk
HH125	9.0	6.3	0.7	39.5	1.1	146.0	10.0	212.7	MEDIUM potential ecological risk
HH128	8.8	1.9	0.7	49.1	0.3	119.6	7.9	188.3	MEDIUM potential ecological risk
HH130	9.2	7.0	0.7	53.2	1.0	150.6	6.4	228.1	MEDIUM potential ecological risk
HH133	11.7	3.0	1.0	79.2	0.7	131.8	13.1	240.5	MEDIUM potential ecological risk

Tab. 4 Assessment on biological toxicity effects in surface sediments

Elements	Cu	Pb	Zn	Cd	Cr	Hg	As
ER-L	34	46.7	150	1.2	81	0.15	8.2
ER-M	270	218	410	9.6	370	0.71	70
Yellow River estuary	24.81	18.62	33.08	0.16	30.95	0.049	9.63

Tab. 4 illustrates that the average contents of Cu, Pb, Zn, Cd, Cr and Hg in the

sediments of the Yellow River estuary are less than ER-L, respectively, indicating that these heavy metals will not generate adverse biological effects on the Yellow River estuary on a short and medium time scale. In contrast, the average content of As is between ER-L and ER-M, indicating that As occasionally has adverse impact on organisms in the Yellow River estuary environment.

3.4 Assessment on the correlation between heavy metals

Currently, it is generally recognized that heavy metal contents in sediments are comprehensively affected by environment background values, human activities, as well as various biological, physical and chemical factors of the ocean. Table 5 illustrates that the correlation between the elements Cu-Cd, Pb-Cr and Cr-As is extremely significant, respectively, which indicates that heavy metals in each group are translocated following similar rules. In sediments, the contents of these heavy metals have a common changing trend. They are accumulated in sediments through coprecipitation or adsorption, showing that they respectively have similar geochemical properties and sources. The correlation coefficient of Cu and Cd is over 0.80, meaning homology and highly significant positive correlation between the two elements. In comparison, the correlation between Hg and other heavy metals is least significant, which may be associated with the enrichment of Hg under the action of microorganisms and algae.

Tab. 5 Correlation analysis of heavy metals in sediments

(Significance Level α=0.05)

Elements	Cu	Pb	Zn	Cd	Cr	Hg	As
Cu	1.000	0.136	0.412	0.840	0.356	0.130	-0.185
Pb		1.000	-0.011	0.047	0.625	-0.202	-0.130
Zn			1.000	0.336	0.113	0.411	0.125
Cd				1.000	0.211	0.005	-0.020
Cr					1.000	0.154	-0.445
Hg						1.000	-0.322
As							1.000

4 Conclusions

a) The average contents of all heavy metals in sediments of the Yellow River estuary comply with the Level-I of NMSQSC, which suggests that heavy metal pollution is not serious in the Yellow River estuary.

b) Cu, Pb, Zn, Cr and As in sediments of the Yellow River estuary are at low potential ecological risk level. The potential ecological risks of sediments of the estuary are mainly attributed to the *RI* of Cd and Hg.

c) As occasionally leads to adverse effects on organisms in the Yellow River estuary and its surrounding sea area, while Cu, Pb, Zn, Cd, Cr and Hg in sediments of the Yellow River estuary will not generate adverse biological effects on a short and medium time scale.

d) In the sediments of the Yellow River estuary, the correlation between the elements Cu-Cd, Pb-Cr and Cr-As is extremely significant, respectively, indicating that they respectively have similar geochemical properties and sources.

Acknowledgements

This paper was supported by the Research Funds Projects of The Institute of Seawater Desalination and Multipurpose Utilization(No. K-JBYWF-2015-G09) and Public Science and Technology Research Funds Projects of Ocean (No. 201105015).

References

[1] Pang Jiazhen, Si Shuheng. The estuary changes of Huanghe River:changes in modern time [J]. Oceanologia et timnologia sinica, 1979 (02): 136 - 141.

[2] State oceanic administration people's republic of China. State of Chinese marine environment in 2012 [R]. Beijing: State oceanic administration people's republic of China, 2013.

[3] National standards of PRC, GB 18668-2002 Marine sediment quality [S], Beijing: Standards press of China, 2002.

[4] Hakanson L. An ecological risk index for aquatic pollution control: a sedimentological approach [J]. Water Research, 1980, 14(8): 975 - 1 001.

[5] Long E R, Morgan L G. NOAA, Technical memorandum NOS OMA 52. The potential for biological effects of sediment-sorbed contaminants tested in the national status and trends program, 1990: 8 - 60.

[6] National standards of PRC, GB 17378-2007 Marine monitoring specification [S], Beijing: Standards press of China, 1999.

[7] Zhao Yiyang, Yan Mingcai. Shallow-sea sediments geochemistry in China [M]. Beijing: Science press, 1994.

黄河口表层沉积物污染现状及潜在生态污染风险评估

张亚南[1,2]，贺 青[2]，暨卫东[2]，张 琦[1*]

（1. 国家海洋局天津海水淡化与综合利用研究所，天津 300192；

2. 国家海洋局第三海洋研究所，福建 厦门 361005）

摘 要：根据2006年到2007年，908专项黄河口附近海域表层沉积物的调查资料，研究黄河口海域表层沉积物中重金属含量分布特征；沉积物中Cu-Cd、Pb-Cr、Cr-As 3组元素间具有显著的相关性，表明它们分别具有相似的元素地球化学性质和来源；运用Hakanson潜在生态危害系数法对其潜在生态危害程度进行评估，黄河口沉积物的潜在生态风险的来源是镉和汞占据主要权重；运用生物效应浓度法对其生物毒性效应进行评价，结果表明，As对黄河口海域环境中生物的负面效应偶尔发生，Cu、Pb、Zn、Cd、Cr和Hg暂时不会产生不良生物效应。

关键词：黄河口；重金属；污染风险评估

A study of impact of the reclamation and artificial island projects on tidal currents and sediment concentration in radial sand ridge field of the South Yellow Sea

ZHAO Qiang[1, 2], LONG Shao-qiao[1], YANG Yao-fang[1], HE Qin-yan[1]

1. *Ningbo Marine Environment Monitoring Center, SOA, Ningbo* 305040, *Zhejiang province, China*;

2. *Laboratory of Physical Oceanography, Ocean University of China, Qingdao* 266003, *Shandong province, China*

Abstract: The two-dimensional hydrodynamic model, MIKE21, is applied to simulate the tidal currents and sediment concentration in the radial sand ridges of the South Yellow Sea. Results are in accordance with in situ observations. Then the variations of tidal currents and suspended sediment concentration caused by reclamation and artificial islands projects are simulated. The results show that the impacts are limited around the project areas. After the projects, the fan-shaped, Jianggang centered tidal current pattern would be replaced by a pattern which is formed by two tidal paths. One locates at the Xiyang channel in north-south direction, and the other locates at the Huangshayang channel in east-west direction. The reclamation of Tiaozini separates the waters into south portion and north portion. The changes of sediment concentrations coincide with those of currents. Both the sediment concentrations and tidal currents increase at the northwest of Dongsha and the south of Gaoni, while both decrease at the north and south of Tiaozini, and the east and southwest of Dongsha.

Keywords: radial sand ridges; reclamation; artificial island; tidal currents; suspended sediment concentration; numerical modeling

1 Introduction

The South Yellow Sea radial sand ridge (SYSRSR) field is located on the continental shelf of the South Yellow Sea off the Jiangsu coast. The SYSRSR field ranges from Sheyang estuary to the north bank of the Yangtze (Changjiang) River. It extends approximately 200 km from north to south, and 140 km from east to west. Centered on the coastal city of Jianggang, more than 70 sand ridges and tidal channels are radially

Received on Jun. 18, 2014

Corresponding author: qiangzhao.cn@gmail.com

distributed in a fan-shaped feature. Each sand ridge is from ten to more than a hundred kilometers long and about ten kilometers wide. The SYSRSR system is a unique geomorphological feature in the Yellow Sea (Li, et al., 2001; Wu, 2004).

In the SYSRSR field, the progressive tidal wave system propagating from the East China Sea encounters with the rotational tidal wave system approaching from the South Yellow Sea, which constitutes a convergent-divergent tidal current system with an apex at Jianggang. Flood tidal currents converge to the apical area from north, northeast, east and southeast directions, while ebb tidal currents diverge offward from Jianggang in the fan-shape with a central angle of about 150° (Li et al., 2001).

Measurements show that the SYSRSR field is characterized by high suspended sediment concentrations (SSCs), especially in winter. The tidal-averaged SSCs range from 0.2 to 1.0 $kg \cdot m^{-3}$ with the maximum of 1.3 $kg \cdot m^{-3}$ in winter. In summer, the range of SSCs usually is 0.1-0.7 $kg \cdot m^{-3}$, but in some nearshore areas, the value can exceed 1.0 $kg \cdot m^{-3}$ (Yang et al., 2010; Huang et al., 2011). Satellite images (Xing et al., 2010; Pan et al., 2013) and model results (Yang et al., 2010; Xing et al., 2012) indicate that SSCs are high in shallow waters, especially in the coastal water off Jianggang and the abandoned Yellow River mouth, and decrease seaward with water depths increasing.

With the population increasing and economic development, sea reclamation becomes one of the most important methods to relieve the pressure on the limited land resources. In the SYSRSR region, eight sand ridges partly expose above water during ebb tide and each one includes 5 to 12 sandbars of different sizes (Lu et al., 2002), which are valuable potential beach resources. Mentioned by Jiangsu Coastal Beach Reclamation and Utilization Plan, the reclamation area off Jiangsu coast will be up to 1 800 km^2 by 2020, and the reclamation and utilization of the radial sand ridges are the major focus. Some projects are planned to reclaim about 267 km^2 at Tiaozini and build two artificial islands at Dongsha and Gaoni with areas of 213 km^2 and 187 km^2 respectively. The positions of the projects and the topography around are shown in Fig.1.

In this paper, the two-dimensional hydrodynamic model, MIKE21, was applied to simulate tidal currents and SSCs in the SYSRSR field. In situ observations were used to calibrate the model. Then the variations of the tidal currents and SSCs caused by the reclamation project were analyzed.

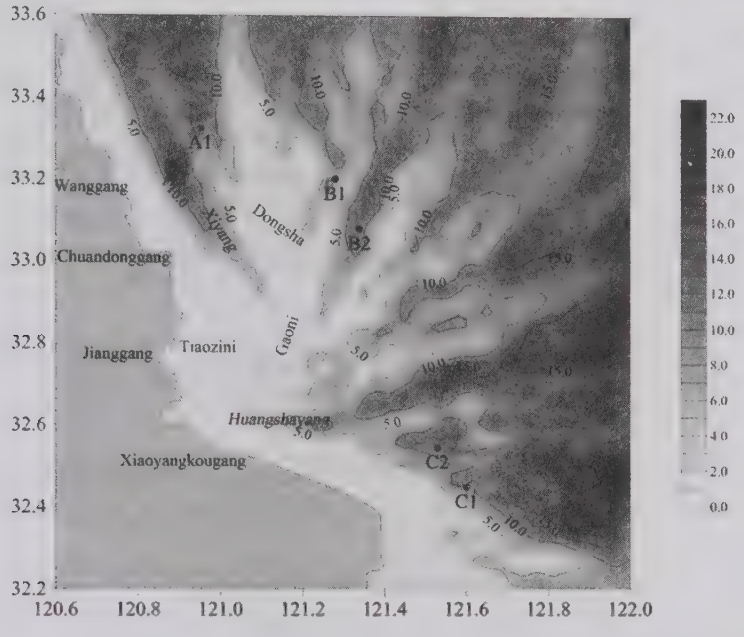

Fig. 1 Location and topography of the SYSRSR field showing sample stations (black dot). Water depth is in meter. Dash lines indicate the positions of the reclamation projects in the plan.

2 Model setup

2.1 The governing equations

The numerical model MIKE21 by DHI (2009) was used to simulate the hydrodynamics and SSCs in the SYSRSR region. The governing equations in hydrodynamic model in Cartesian coordinates are written as follows:

$$\frac{\partial \eta}{\partial t}+\frac{\partial p}{\partial x}+\frac{\partial q}{\partial y}=\frac{\partial d}{\partial t}$$

$$\begin{aligned}&\frac{\partial p}{\partial t}+\frac{\partial}{\partial x}\left(\frac{p^2}{h}\right)+\frac{\partial}{\partial y}\left(\frac{pq}{h}\right)+gh\frac{\partial \eta}{\partial x}+\frac{gp\sqrt{p^2+q^2}}{C^2\cdot h^2}\\&-\frac{1}{\rho_0}\left(\frac{\partial}{\partial x}(hs_{xx})+\frac{\partial}{\partial y}(hs_{xy})\right)-\Omega_q-fVV_x+\frac{h}{\rho_0}\frac{\partial}{\partial x}(p_a)=0\end{aligned},$$

$$\begin{aligned}&\frac{\partial q}{\partial t}+\frac{\partial}{\partial y}\left(\frac{q^2}{h}\right)+\frac{\partial}{\partial x}\left(\frac{pq}{h}\right)+gh\frac{\partial \eta}{\partial y}+\frac{gq\sqrt{p^2+q^2}}{C^2\cdot h^2}\\&-\frac{1}{\rho_0}\left(\frac{\partial}{\partial y}(hs_{yy})+\frac{\partial}{\partial x}(hs_{xy})\right)+\Omega_p-fVV_y+\frac{h}{\rho_0}\frac{\partial}{\partial y}(p_a)=0\end{aligned},$$

where x and y are coordinates in space, and t is time; h is water depth; and $h=\eta - d$, η is surface elevation; p and q are flux densities in x- and y-directions; Ω is latitude dependent

Coriolis parameter, and g is acceleration due to gravity; C is Chezy resistance, which increases with water depth, ranging from 50 to 90 $m^{1/2}/s$ in the model; $f(V)$ is the wind friction factor, and V, V_x and V_y are wind speed and components in x- and y- directions; p_a is atmospheric pressure; ρ_0 is density of water; s_{xx}, s_{yy}, s_{xy} are components of effective shear stress.

The transport equation of suspended sediments, so-called advection-dispersion equation, is expressed as:

$$\frac{\partial S}{\partial t}+u\frac{\partial S}{\partial x}+v\frac{\partial S}{\partial y}=\frac{1}{h}\frac{\partial}{\partial x}\left(hD_x\frac{\partial S}{\partial x}\right)+\frac{1}{h}\frac{\partial}{\partial y}\left(hD_y\frac{\partial S}{\partial y}\right)-\frac{F_s}{h},$$

where S is depth-averaged SSC. D_x and D_y are dispersion coefficients. F_s is deposition /erosion term, which is determined by bed shear stress:

$$F_s=\begin{cases}\omega_s c_b(1-\tau/\tau_d) & \tau\le\tau_d\\ 0 & \tau_d<\tau<\tau_e\\ E(1-\tau/\tau_e)^n & \tau\ge\tau_e\end{cases},$$

where ω_s is settling velocity; c_b is near bed concentration; τ is bed shear stress; τ_d is critical bed shear stress for deposition; τ_e is critical bed shear stress for erosion; and E is erodibility of bed. After the calibration, the parameter values of ω_s, τ_d, τ_e and E are set to 0.000 5 m/s, 0.2 $N\cdot m^{-2}$, 0.6 $N\cdot m^{-2}$ and 0.000 1 $kg\cdot m^{-2}/s$, respectively.

2.2 Meshes and boundary conditions

The model area (Fig. 2) ranges from the south coast of Shandong Peninsula to the north of the Yangtze River mouth, including most part of western and central Yellow Sea. The water depths are digitized from Marine Atlas of Bohai Sea Yellow Sea East China Sea. To keep high spatial resolution and computational efficiency, unstructured triangular meshes are used, and the project areas are refined. There are 20 683 elements in the model. The time step is 30 s.

The land boundary condition is the full slip boundary condition, that is, the normal velocity component is zero:

$$V_n=V\times n=0.$$

The open boundary condition is water level condition:

$$\eta=\eta_{OBC}(t),$$

where $\eta_{OBC}(t)$ is tide level at the open boundary, which is calculated by harmonic

constants of nine major constituents (Q1, O1, P1, K1, N2, M2, S2, K2, Mf).

In the coastal and sand ridge areas, sandbars expose and submerge following the water flooding onto the inter-tidal zone and draining out of it. The wet/dry point treatment method is used to treat the so-called moving boundaries. When the depths are very small, the elements/cells are removed from the calculation and the momentum fluxes are set to zero. When the depths are greater than a critical depth again, the momentum fluxes are calculated.

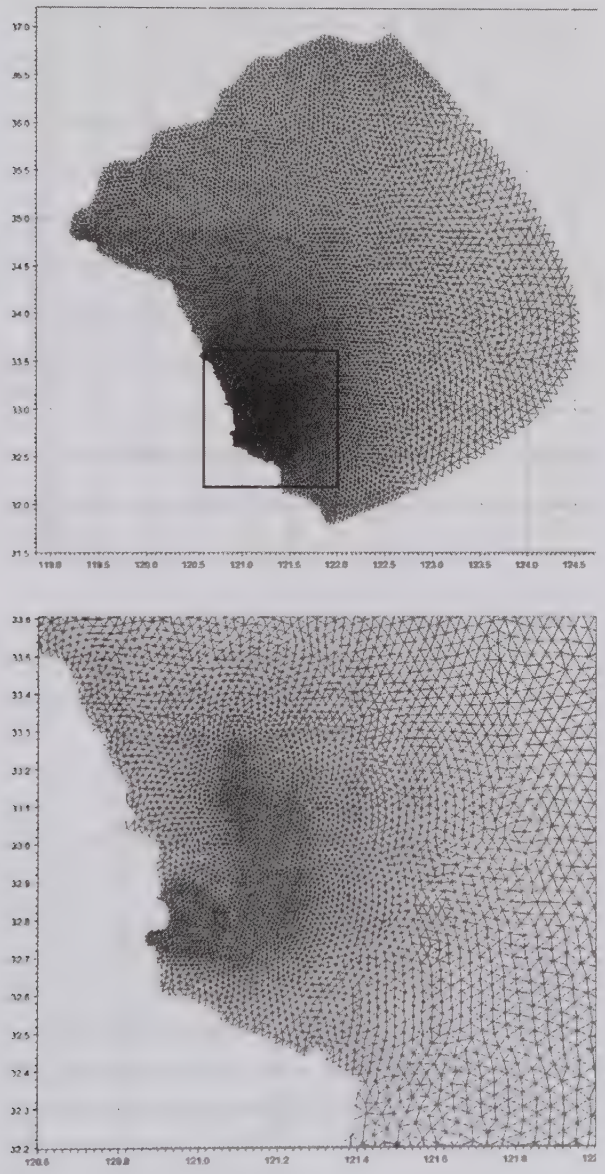

Fig. 2 Meshes of the simulation area

3 Model results

3.1 Model calibration

The in situ observations during 15-16 May (spring tide) and 20-21 May (neap tide) in 2010 are used to calibrate the model. There are 6 current velocity and suspended sediment sample stations (A1, A2, B1, B2, C1, C2) and 1 water level station (C2). The locations of the stations are shown in Fig.1. The model results and corresponding observations are shown in Fig.3-5 (not all results are shown because of the paper length). The comparison indicates the modelled water level, tidal current velocities and SSCs are basically agree with the observations, and the model is well calibrated and capable of reproducing the current and SSC patterns in the study area.

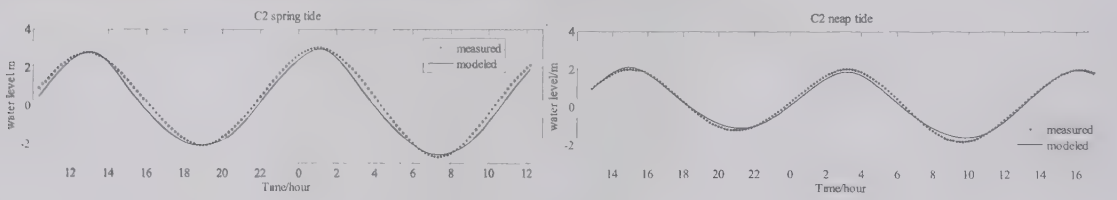

Fig. 3 Calibration of water level at Station C2

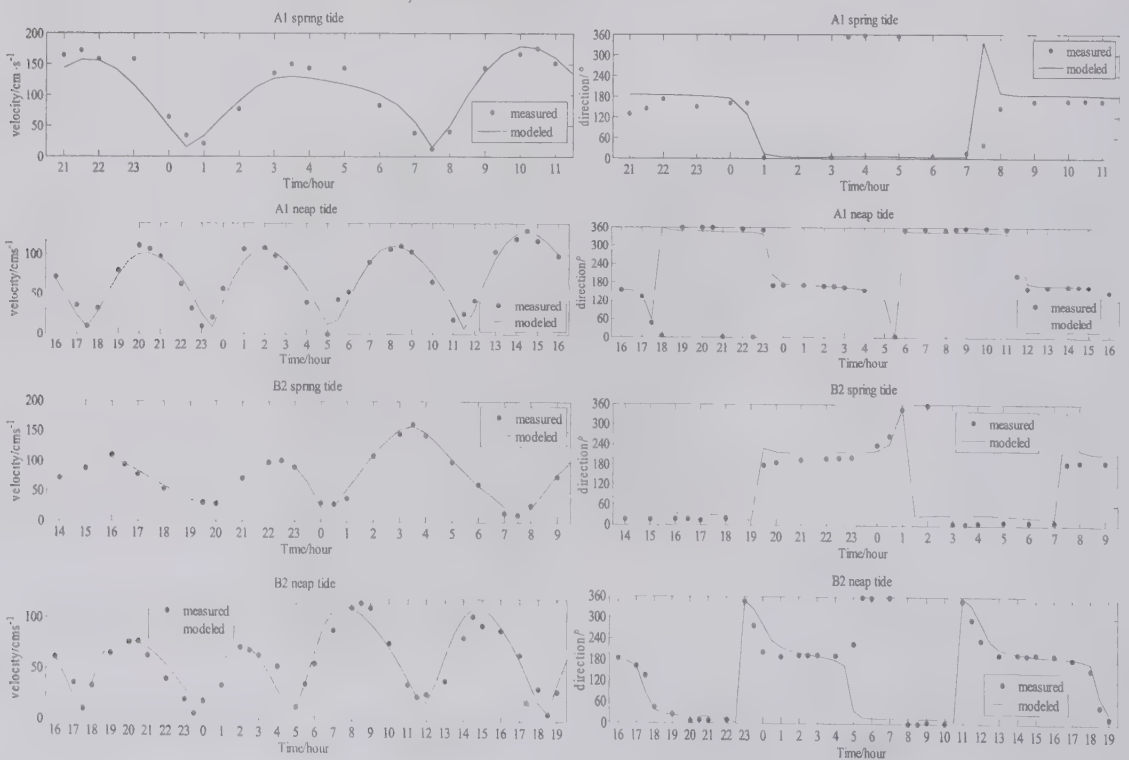

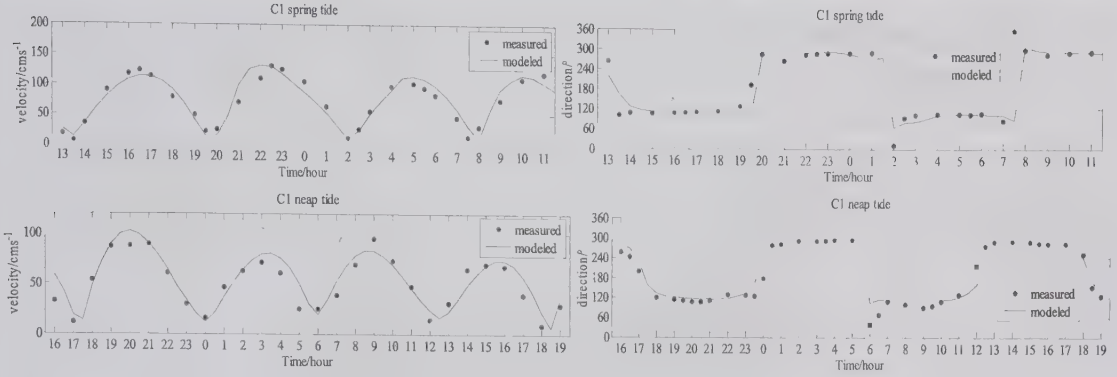

Fig. 4 Calibration of tidal current velocities

(Left column is velocity in cm/s, and right column is direction in degree)

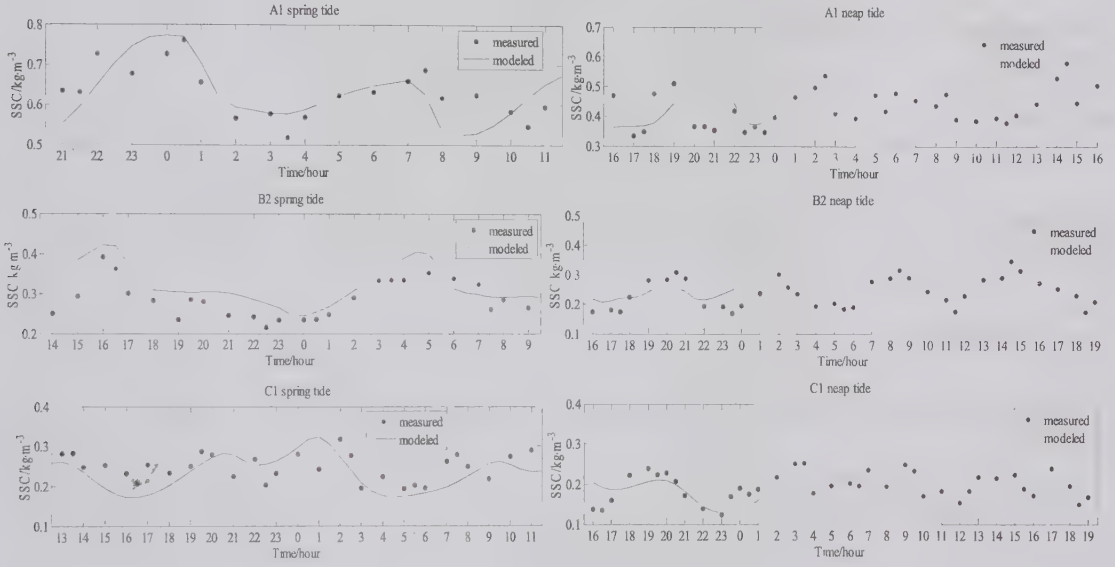

Fig. 5 Calibration of SSCs.

3.2 Model results of tidal currents in the SYSRSR

The simulated flood and ebb tidal current vectors during spring tide in the SYSRSR region are shown in Fig.6. During the flood tide, as the water level rises, tidal currents converge to Jianggang from north, northeast, east and southeast directions generally along the sand ridges. During the ebb tide, currents diverge offward from Jianggang in the fan-shape with a central angle of 150°. The current field during the neap tide is similar to that during the flood tide, but the velocities are lower (the figures are not shown). In general, the tidal current in the SYSRSR field manifests a convergent-divergent pattern in the 150°-fan-shape with the apex at Jianggang.

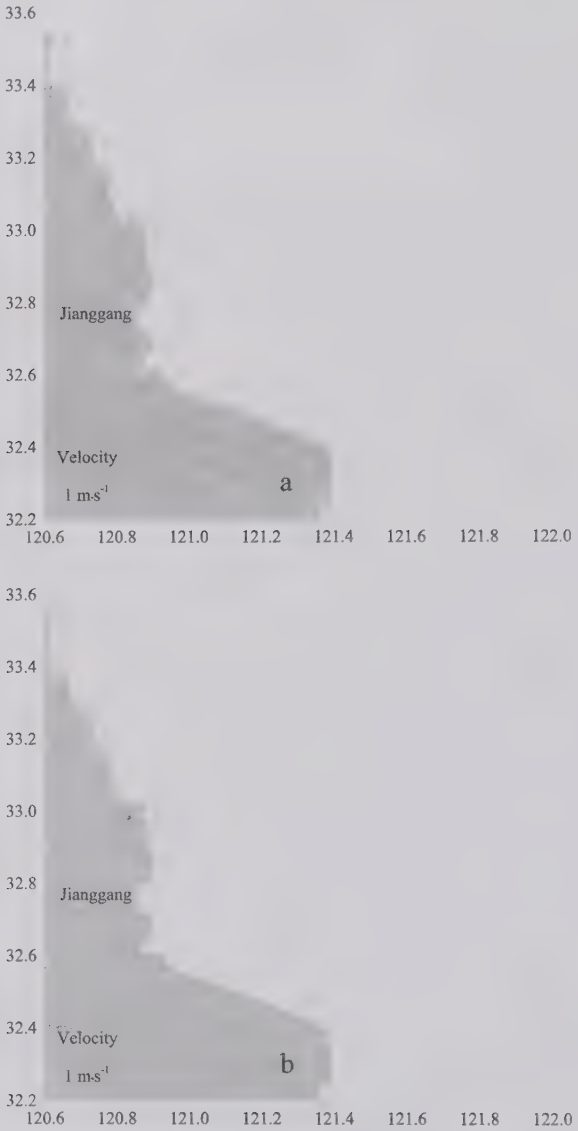

Fig. 6 Simulated current vectors during the spring tide for SYSRSR: (a) flood, (b) ebb

3.3 Model results of SSCs in the SYSRSR

Fig. 7 shows the simulated tidal-averaged SSCs in the SYSRSR field. The highest SSC is located at the northeast area off Jianggang with the maximum of 1.2 $kg \cdot m^{-3}$. Sufficient sediments are supplied by the abandoned Yellow River delta through the Xiyang water channel (Huang et al., 2011) and they deposit on the east of Jianggang (Zhu and Chang, 1997; Ni et al., 2013). The high SSCs are situated at the south end of Xiyang channel. The strong hydrodynamics there make the sediments easy to suspend and form

high SSCs. As a whole, considering Tiaozini as a boundary line, the modelled SSCs in the north are much higher than those in the south. This feature coincides with the observations (Yang et al., 2010; Xing et al., 2012). Researchers used several methods, like artificial neural network (Yang et al., 2010), remote sensing (Xing et al., 2010), numerical model (Huang et al., 2011), to study the distributions of suspended sediments in the SYSRSR, and these researches showed the similar results with ours.

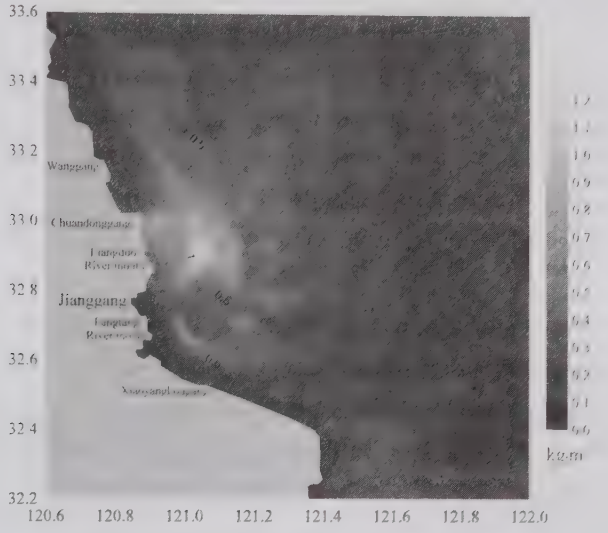

Fig. 7 Simulated tidal-averaged SSCs

3.4 The influence on hydrodynamics by reclamation and artificial island projects

The influences on hydrodynamics by the artificial projects are not obvious in the whole SYSRSR region but notable around the project areas. As the study area is large and the topography and coasts are complicated, the time of flood or ebb is not simultaneous in different regions. In this section, the 3-hourly simulated results during a semi-diurnal tidal period, which represent flood slack, maximum ebb, ebb slack and maximum flood, are used to illustrate the variations of water levels and currents after the artificial projects. The results are shown in Fig. 8 and Fig. 9.

During flood slack (in Fig. 8a and Fig. 9a), water levels are high in the whole SYSRSR area. The highest water level is located at the southeast of the Fangtang River mouth, and the lowest water level is located at the north. Before the projects, tidal currents are weak anywhere. After the projects, water levels show a similar pattern in most of the area to that before, but obvious gradients of water levels arise beside Dongsha in east-west direction and induce strong currents with maximum over 1 m/s on the northwest of Dongsha and in the narrow channel between Gaoni and Dongsha.

During maximum ebb (in Fig. 8b and Fig. 9b), before the projects, the relative high water levels are located off the Fangtang River mouth, while relative low water levels are located at the out sea. The ebb currents flow seaward with a radial pattern in the fan-shape. After the projects, not like the fan-shaped pattern before, the current pattern is dominated by two nearly separated tidal paths. The southern currents flow eastward through the Huangshayang channel following barotropic gradients, and the speeds are larger than that before. When the currents flow to the southeast of Tiaozini, a subsection turns to the north and flows through the channel between Tiaozini and Gaoni. The northern currents flow northward through the Xiyang water channel, and a little portion flows to the east through the channel between Gaoni and Dongsha, then turns to the northeast following the isobaths.

During ebb slack (in Fig.8c and Fig.9c), low water levels occupy the whole region. Before the projects, the highest water levels are located at Jianggang and the Fangtang River mouth, and the relative low water levels are located at the Xiyang and Huangshayang channels. The currents are weak in the most of the area, but those in the Xiyang and Huangshayang channels are relative strong with the maximum about 1 $m \cdot s^{-1}$. After the projects, the water levels and currents are almost the same with those before, except the water levels north to Tiaozini and south to Gaoni are a bit lower than that before.

During maximum flood (in Fig. 8d and Fig. 9d), before the projects, the lowest water level is located off Jianggang, and the highest water level is located at the northwest. Flood currents converge to Jianggang from the east, northeast, north and northwest directions radially. After the projects, the lowest water level moves to the Fangtang River mouth. The waters flooding from the northeast are blocked by Dongsha, and the highest water level is located at the east side of Dongsha as the result of water accumulation. The currents off the east side of Dongsha are much weaker than those before the projects, because the gradients of the water levels are much smaller. These currents flow around the northern Dongsha, then turn southward into the Xiyang channel. The waters flooding from the east are blocked by Gaoni and flow into the Huangshayang channel in the south. A portion of the water moves around the southern margin of Gaoni and turns to the north into the channel between Tiaozini and Gaoni. These waters encounter the waters from the Xiyang channel, so the current speeds in the channel are small. But the water levels at the north of Tiaozini arise quickly than those at the south, so the waters from the north will finally flow to the Fangtang River mouth through the channel between Tiaozini and Gaoni, together with the water in the south.

In general, changes mainly take place during the maximum flood and maximum ebb. When the projects are finished, the artificial constructions will separate the water in the

area, and redistribute the water levels. The fan-shaped current pattern will be replaced by two separated currents paths.

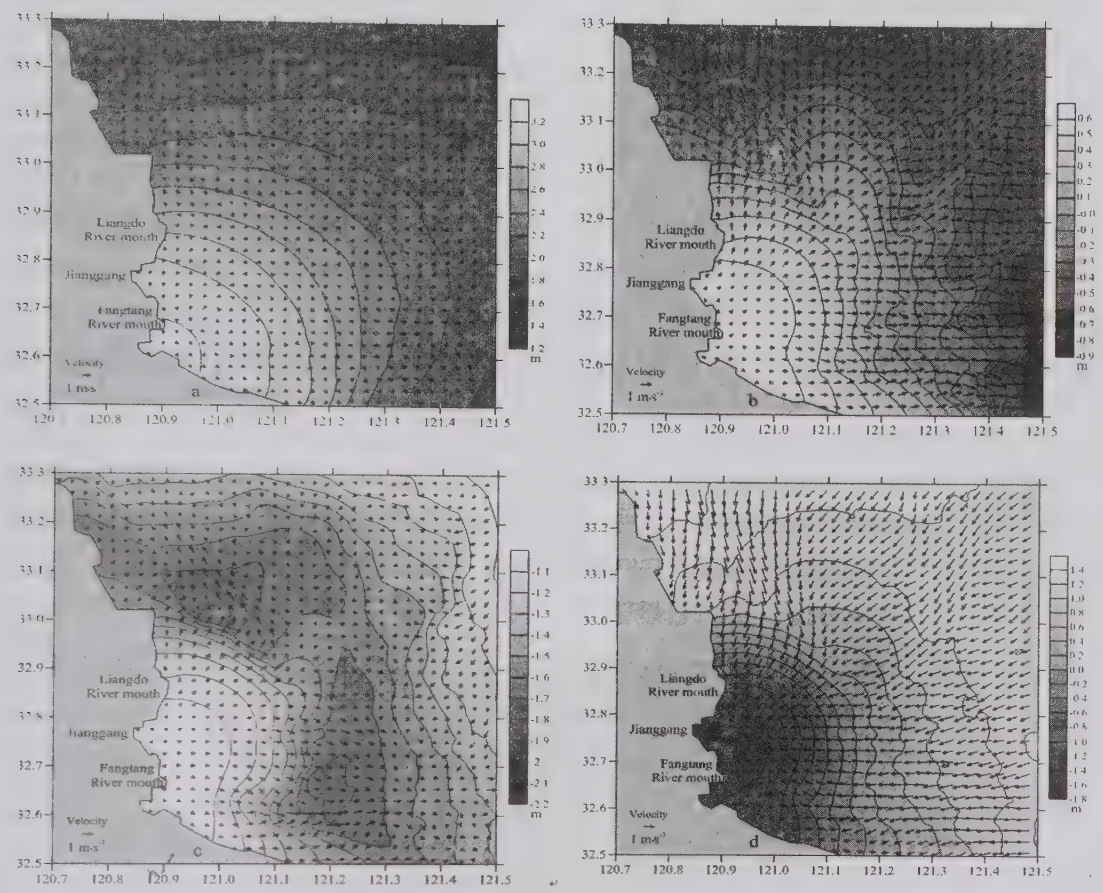

Fig. 8 Water level isolines and current vectors before the projects: (a) flood slack, (b) maximum ebb, (c) ebb slack, and (d) maximum flood

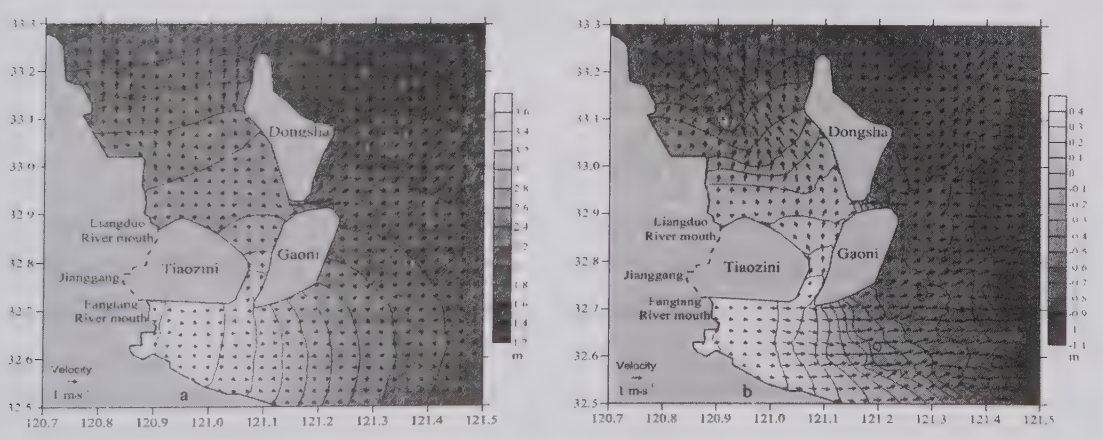

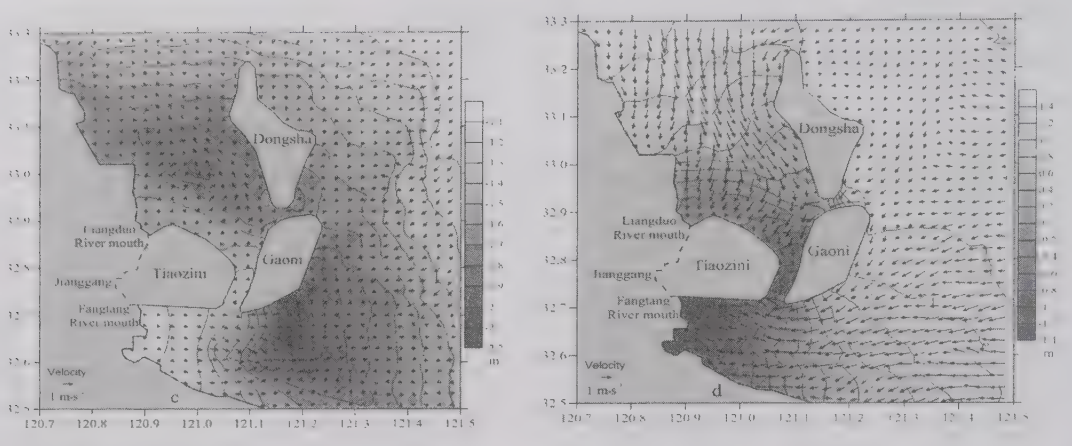

Fig. 9 Water level isolines and current vectors after the projects: (a) flood slack, (b) maximum ebb, (c) ebb slack, and (d) maximum flood

Fig. 10 shows the differences of tidal averaged current speeds before and after the projects. The changes mainly take place around the projects. As the results of blocking by reclamation and artificial islands, waters converge to the water channels. So the current speeds around the artificial constructions reduce, while those in the channels arise.

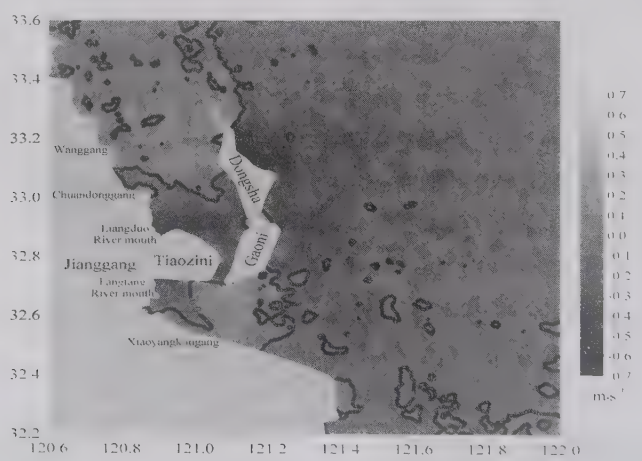

Fig. 10 Differences of the tidal-averaged current speeds before and after the projects

3.5 The influence on SSCs by reclamation and artificial island projects

As illustrated in Fig. 11, the variations of tidal averaged SSCs before and after the projects show a similar pattern to the current speed changes in Fig.10. The SSC and current speed exhibit positive correlation as mentioned by Wu et al. (2007). They found that the SSCs in the SYSRSR region were mainly decided by the tidal current speeds based on in situ surveys. Noticeable SSC increase can be found at the northwest of

Dongsha and the south of Gaoni. SSCs decrease at the east and southwest of Dongsha, as well as the southwest and north of Tiaozini. The SSCs in the channel between Dongsha and Gaoni do not increase as the currents do, because the SSCs in the surrounding waters decrease obviously.

Besides tidal current speeds, the wave may be another factor to influence SSCs in sea waters. But in this paper, waves are not considered in the model based on several reasons. First, the data used to validate the model were investigated in spring 2010, during which the waves were weak. Second, waves propagating from out sea to the SYSRSR region are blocked by sand ridges. Because of wave refraction and breaking, the wave energy loses and the wave height reduces rapidly. The wave heights in the project regions are really small (Wang, 2002). Third, the waves in the SYSRSR area are dominated by winds which change seasonally. When considering the seasonal winds, the seasonal variations of suspended sediment transport on the open boundaries, e.g. the seasonal changes of the amount and SSC of the Changjiang Diluted Water, as well as barotropic and baroclinic circulations which may be not small compared with the tidal residual currents, should also be considered. These issues are beyond the studies in the present paper. Actually, numerical model experiments conducted by Xing et al. (2012) indicated that the wave was not a significant factor to impact the SSC in the SYSRSR field.

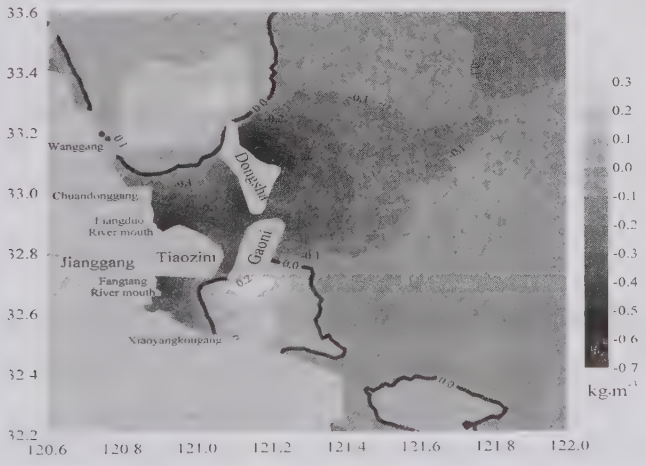

Fig. 11 Differences of the tidal-averaged SSCs before and after the projects

4 Conclusions

The SYSRSR field is the place where the progressive tidal wave system propagating from the East China Sea encounters with the rotational tidal wave system approaching from the South Yellow Sea. It is characterized by large tidal rang and strong tidal currents.

In this paper, the two-dimensional hydrodynamic model, MIKE21, was applied to simulate water levels, tidal currents, and SSCs in the SYSRSR region. Then the variations of the tidal currents and SSCs caused by the reclamation projects were simulated.

It is shown by the results that the dynamics of the entire SYSRSR field is not affected severely by the projects, but the currents around the project areas change a lot. After the artificial constructions are built, the flood currents, which used to converge from the northern and northeastern out sea to Jianggang through the channels of Kushuiyang, Caomishuyang and Pingtuyang, are blocked by the artificial islands of Dongsha and Gaoni. The currents flow around the islands and converge into the two channels of Xiyang and Huangshayang. The ebb currents also need to flow around the islands and back into out sea. Currents in the two channels strengthen after the projects, while those at the east of the islands weaken. The currents in the northeast-southwest directions decrease obviously after the projects, so the current pattern cannot be considered as a fan-shaped radial system, but a system is constituted by two nearly separated tidal paths. The northern path is the Xiyang water channel in north-south direction, and the southern path is the Huangshayang water channel in east-west direction. The apex of the radial current system which used to be at Jianggang moves south to the Fangtang River mouth.

The variations of SSCs after the projects coincide with those of currents. SSCs increase on the northwest of Dongsha and the south of Gaoni, while those decrease on the south and north of Tiaozini as well as the east and southwest of Dongsha. In the present SSC simulation, the tide is the only factor considered, and the seasonally varied waves and circulations will be included in the model in the further study.

References

[1] DHI. MIKE 21 flow model hydrodynamic module scientific documentation. Danish Hydraulic Institute, 2009.

[2] Huang Huiming, Wang Yigang, Shangjin, et al. Distribution and transport characteristics of suspended sediment in winter water areas of radial sand ridges in northern Jiangsu Province [J]. Journal of Hohai University, 2011, 39(2): 201 - 205.

[3] Li Congxian, Zhang Jiaqiang, Fan Daidu, et al. Holocene regression and the tidal radial sand ridge system formation in the Jiangsu Coastal zone, east China [J]. Marine Geology, 2001, 173: 97 - 120.

[4] Liu Tao. Modern sedimentary environment research on the radial sand ridges off Jiangsu coast [J]. Qingdao: Institute of Oceanography Chinese Academy of Sciences, 2011, 135

[5] Pan Jin, Ding Xianrong, Kang Yanyan et al. An inversion method of suspended sediment concentration at radial sand ridges [J]. Geospatial Information, 2013, 11(2): 82 - 87.

[6] Ni Wenfei, Wang Yaping, Zou Xinqing, et al. Study on the sediment dynamics and stability of the Kushuiyang tidal channel at radial sand ridges in the southern Yellow Sea [J]. Marine Science Bulletin, 2013, 32(6): 668 - 677.

[7] Wu Dean. Hydrodynamic studies to the tidal current and suspended sediments in the channels of Jiangsu Radial Sand Ridges [D]. Nanjing: Nanjing Normal University, 2004, 120.

[8] Wu Dean, Zhang Renshun, Yan Yixin, et al. The study on sediment carrying capacity of the tidal channels in Jiangsu radial sand ridge sea area [J]. Journal of Hydrodynamics, 2007, 22(3): 371 - 379.

[9] Xing Fei, Wang Yaping, Gao Jianhua, et al. Seasonal distributions of the concentrations of suspended sediment along Jiangsu Coastal Sea [J]. Oceanologia et Limnologia Sinica, 41(3): 459 - 468.

[10] Xing Fei, Wang Yaping, Wang Harry V. Tidal hydrodynamics and fine-grained sediment transport on the radial sand ridge system in the southern Yellow Sea [J]. Marine Geology, 2012, 291 - 294: 192 - 210.

[11] Yang Yaozhong, Feng Weibing. Numerical study on distribution of suspended sediment over radial sand ridge field on continental shelf of South Yellow Sea [J]. Journal of Waterway and Harbor, 2010, 31(3): 157 - 163.

[12] Zhu Yurong, Chang Ruifang. Explanation of the origin of radial sand ridges in the southern Yellow Sea with numerical simulation results of tidal currents [J]. Journal of Ocean University of Qingdao, 1997, 27(2): 218 - 224.

人工岛工程对南黄海辐射沙脊群海域潮流泥沙影响研究

赵 强[1,2]，何琴燕[1]，杨耀芳[1]，黄秀清[1]

（1. 国家海洋局宁波海洋环境监测中心站 浙江 宁波 315040；2. 中国海洋大学物理海洋实验室 山东 青岛 266003）

摘 要：本文采用 MIKE21 二维水动力模型模拟了南黄海辐射沙脊群海域的潮流形态和含沙量，模拟结果与实测数据基本一致。在此基础上，模拟计算了围填海工程后辐射沙脊群海域的潮流和含沙量变化。结果显示工程对潮流和含沙量的影响主要出现在工程区附近。围填海工程使原本以弶港为中心呈扇形辐聚、辐散的潮流格局有所改变，形成东沙岛西侧南北向和高泥岛南侧东西向的两条潮流通道，并在一定程度上分割了条子泥南北两侧的水体。工程后含沙量的变化与平均流速的变化基本一致，在流速变大的东沙岛西北侧和高泥岛南侧海域，含沙量显著升高；在流速变小的条子泥南北两侧、东沙岛东侧及西南侧，含沙量显著降低。

关键词：辐射沙脊；围填海；潮流；含沙量；数值模型

Digital Ocean Information Framework of China and its application in the international marine cooperation

YU Ting[1, 3], DENG Zeng-an[1, 2], SHI Sui-xiang[1, 2]

1. *National Marine Data and Information Service, Tianjin* 300171, *China;*

2. *Key Laboratory of Digital Ocean, State Oceanic Administration, Tianjin* 300171, *China;*

3. *Ocean University of China, Qingdao* 266100, *Shandong province, China*

Abstract: Digital Ocean Information Framework (DOIF) has been proposed by China in 2011 based on the achievements of the comprehensive offshore oceanic surveys supported by Chinese Offshore Investigation and Assessment Program, whose code name is 908. All observations from the surveys have been integrated and managed by DOIF. DOIF is capable of supporting the decision of making process for the sustainable use of marine resources in coastal regions of China, providing useful information and added value products as well as services for the improved management of the coastal areas in China with high business impact on the targeted groups as public authorities and commercial operators (e.g. managers, fishermen, shipping companies). The future vision of DOIF in the international marine data and information exchange and service at Western Pacific region is presented in this paper.

Keywords: digital ocean, ocean observing system, integrated data management, decision making

Introduction

China is a developing country with emerging blue-ocean economy. The coastline of Chinese mainland covers approximately 18,000 km from the Yalu River at the north to the Beilun River at the south. Forty percent of the population is living in coastal areas. Ocean is playing an important role in Chinese modern society. The benefits in the food supply, transportation, recreational activities, and national security, brought by ocean and seas to China cannot be underestimated. During enjoying the splendor of the ocean, we realize the needs to better understand it and the responsibilities to protect it from the accumulating consequences of human activity. Now, China's ocean observation activities and maritime affairs have already entered a new era, which is an era of integrated development and management.

Received on Dec. 10, 2014

Corresponding author: Julia_yu_nmdis@163.com

In view of the importance of the ocean territory, it is our responsibilities to ensure its long term sustainable use of the ocean and its resources. This requires a scientific basis of monitoring, modeling and understanding of the marine environment. Observational data are the fundamental basis of understanding the oceans. Well-organized ocean scientific observations carried out by Chinese oceanography community could be traced back to 1950's. However, these activities were often scattered and discontinuous in the time and space due to many reasons. Lack of continuous funding is definitely one of them. To align the existing observation abilities and integrate the observational data and information at a national level, State Oceanic Administration (SOA) of China has organized a comprehensive Offshore Investigation and Assessment Program (referred as 908) during the past years. For the effective management of the integrated data and information, and the sustainable development of the ocean observing system, Digital Ocean Information Framework (DOIF) has been proposed under the support of 908 Program (National Marine Data and Information Service, 2011). DOIF is a very important task of the China's Marine Informationization Program. It has been developed with considerable consultations and sharing ideas with government, oceanography communities, environmental agencies, universities, private sectors and other public users on how to ensure the conservation and sustainable development of our precious natural marine assets. In other words, DOIF is designed as an information platform that serves multiple users.

This paper introduces the structure of DOIF and the perspective of DOIF's applicability in supporting the integrated marine management, marine economy development, marine environmental protection and marine rights and interests safeguard. The structure of this paper is organized as follows. The concept of marine informationization program in China is given in section 2. The basic structure and functions of DOIF are presented in section 3. The future vision of applying DOIF in international cooperation and the associated data exchange are given in section 4. Finally, the summary and discussion is presented in section 5.

1 Marine Informationlization Program of China

Marine Informationlization Program of China is a program under the coordination and guidance of Chinese government to gradually establish a national marine information system that consists of the following parts: marine information source (observation), information transmission and service network, information technology, information standards and policies, information management mechanism, IT intelligence, etc. It is aiming at ensuring the streamlined marine data collection, processing and analysis, management and services toward a path of sustainable and healthy development, through

the use of increasingly sophisticated marine information technology. The success of this program requires the integrated planning, well-defined effective implementation mechanism, and social needs driven public services.

The goal of Marine Informationlization Program is to build an integrated platform that involves operational marine data acquisition, standardized data management and visualization, intelligent assessment, scientific decision-making and social needs oriented services. It employs all the related information techniques to realize marine data and information assembly and public sharing, while keeping the interoperability with existing data systems at regional and local level. It supports ocean-related decision-making at different levels by providing scientific, effective, and convenient services for marine economy, marine management, marine environmental protection, marine disaster prevention and mitigation, and safeguard of maritime rights and interests.

Originated from the concept of the Digital Earth, Digital Ocean is an important approach to achieve China's Marine Informationlization Program. It mainly refers to marine virtual visualization system for effectively understanding, exploring and protecting ocean. By using cutting-edge geospatial, information and network technologies, Digital Ocean integrates the comprehensive, real-time, continuous marine physical, chemical, biological, and geological data and information collected by satellite, remote sensing aircraft, ship, investigation vessel, submarine sensors, as well as the marine management information, such as marine rights and interests, into a "super computer system" (Liu et al., 2009).

With the basis of national information infrastructure and marine spatial database, Digital Ocean shows the real ocean states by analyzing the real oceanic phenomenon and processes through digitalizing and visualizing the environmental information. With the aid of virtual simulation technologies, Digital Ocean gives the direct view of the realities and processes happened at seabed, ocean interior, sea surface, islands and the coastal zone, helping the sustainable development of marine observing systems. For example, Digital Ocean could shorten the warning time and improve the forecasting accuracy for Typhoon forecasting and warning. Once the sensor system detects abnormal ocean data, it can automatically estimate the route of the typhoon, wind speed and wave speed, affecting areas, and potential economic loss. With three-dimensional (3D) visualization model, users will be able to see the virtual images – typhoon's formation at the tropical oceans, moving route, and possible landing location – thus greatly help disaster prevention and mitigation.

2 Digital Ocean Information Framework (DOIF)

908 Program was initialized in 2006 and finished in 2012. It includes offshore oceanic

investigations and surveys, and the development of DOIF that is used to integrate, manage and disseminate the derived ocean observation data and information. A total of 295 projects under this program have been implemented and a large number of research achievements have been put into practical use. DOIF mainly includes the following components: Digital Ocean information infrastructure, marine information acquisition system, marine data processing and management system, China Digital Ocean Prototype System.

2.1 Digital Ocean information infrastructure

Digital Ocean information infrastructure mainly refers to the hardware and software environment required for operational running of DOIF, including related marine standards, computer hardware and software facilities, data transmit network and system, and security system, et al.

Developing the Digital Ocean standards is the first step toward a standardized system. It will ensure the consistency and synergies between the various construction tasks. Digital Ocean Standard is defined as the uniform specification or provision for repetitive items and concepts in the digital ocean development. It is based on the science, technology, and best practices, aiming at getting the best order, and the cost-effective benefit. Various standards released in an agreed manner will form a comprehensive document system for the purpose of guiding and coordinating the practices under DOIF. Through the adoption of these standards, the interoperability of platforms would be ensured. The quality, compatibility and coherence of the data from multiple sources, are assured by the adoption of standardized methodologies for data processing, and high-level quality control, laying a strong foundation for the later production of value added product.

Digital Ocean Data Center is the core to support the regular operation of the DOIF. It has the capacities of massive data processing and storage, fault tolerance and incident recovery, high-speed data exchange. The responsibility of Data Center includes data rescue, collection and assembly, quality control, and long-term archival of data and metadata from observing activities conducted by Chinese organizations and international related marine programmes.

Marine information exchange and service network is one of the critical information infrastructures of DOIF. The interaction of operational systems at all levels and real-time data exchange between them will be realized through the broadband marine information exchange and service network, supporting real-time transmission of the ocean data and images.

Marine information security system is designed to protect information system and information networks against all types of threats, disturbance and destruction. Computer operating systems, various security protocols, security mechanisms (digital signatures, message authentication, data encryption, etc.), disaster recovery systems and offsite data backup center are all within the scope of its construction.

2.2 Marine Information Acquisition System

As the foundation of DOIF, the data acquisition system maintains the vitality of data stream. Currently, China's three-dimensional ocean observation system, which monitors the marine environment in real time, is mainly consisting of five parts, the space-based, airborne, land (onshore) based, ship-based and data buoy observation platforms. Multiple observing instruments and platforms such as sateilite, monitoring (surveillance) aircraft, coastal station, drifter and mooring buoy, and vessel, have been integrated to form the operational marine data and information acquisition system with appropriate observing density, reasonable monitoring elements and real-time transmission ability.

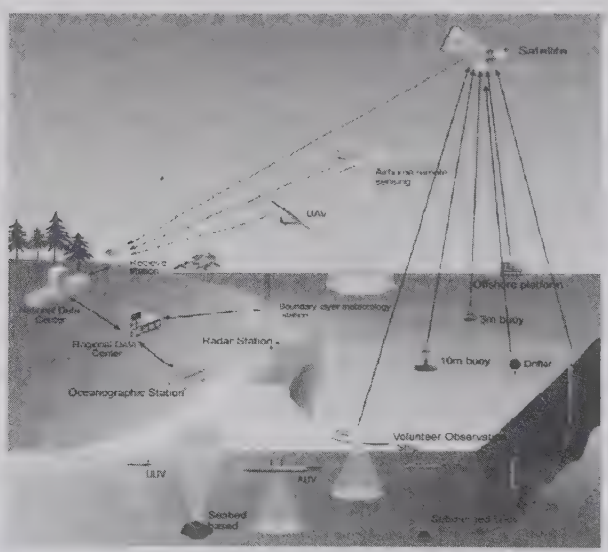

Fig. 1 Schematic map of the integrated ocean observation system in China

Remote sensing images and data obtained by satellite greatly improve our understanding to global and regional oceans. Combined with in-situ observation, the remote sensing fills the gap of large scale ocean observations. By assimilating the remote sensing data together with field observations, global marine environmental forecasting by numerical models has been also improved.

Airplanes and balloons are important airborne observing platforms. They are usually equipped with multiple instruments and sensors such as CCD, microwave radiometer,

ultraviolet/infrared scanner or multispectral scanners, side-looking radar, laser radar, etc. Airborne remote sensing data possess advantage of timeliness and high resolution, thus are of key importance in marine emergency response and specific target real-time monitoring.

Fixed shore-based marine ocean observing system consists of coastal oceanographic stations, HF radar stations, tidal gauges, etc., supporting the real-time monitoring of national coastal seas and islands. The long time series observation data obtained by it is also of significance to the climate study.

Ships and investigation vessels are of vital value for collecting the data in the world ocean, especially in the remote open oceans. Ship-based observations can be divided into many categories, including fixed, hanging, lowered, dragging and disposable deployment. Multidisciplinary parameters of physical oceanography, biology, chemistry, geology, and geomagnetism can be obtained.

Establishment of sea and seabed based marine monitoring data acquisition system which involves floats, drifters, mooring buoys, and other underwater observation equipment, is another goal of improving the existing integrated ocean data acquisition system. Floats and buoys are primary component of the three-dimensional ocean monitoring system. They have the all-weather, long-term, continuous features that remote sensing, vessels and other means of monitoring cannot replace.

By integrating the ocean surface and undersea instrument and facilities in coastal waters and open oceans, the framework plans to strengthen the 3D monitoring network over the coastal seas in China and adjacent seas, for obtaining the long-term, continuous operational data from multidiscipline, such as physical oceanography, marine meteorology, chemistry, and biology, as well as the real-time emergency event monitoring data.

2.3 Marine data processing and management system

With the advancement of ocean observing technology, we are facing the challenge brought by different data derived from multiple means and various sensors. Moreover, the data from the traditional instrument often have discrete distribution in space and discontinuousness in time. How to carry out standardized data processing and management is a serious problem faced by both users and data managers. Therefore, the needs for establishing marine data information processing and management system for multi-channel sources using standardized and uniform data processing standards are becoming increasingly obvious and of growing concerns.

High level oceanographic data processing and quality control is essential for DOIF to provide high-quality information service. Automatic quality control procedures and visual checks are carried out on data obtained under the requirements of international and national programs. In particular, for essential ocean and climate variables that are of great concerns, expert inspections are conducted. Suitable procedures, standards and best practices will be followed for data quality and management. Optimization criteria and methods are being proposed to solve the difficulty of multi-source, discrete, discontinuous spatial and temporal distribution faced in the process of data analysis and application (Wang et al., 2008).

The growing needs of the scientific research institutions and the general public for marine data and information exert an unprecedented challenge for strengthening the obtaining of massive basic marine data and information. The ocean data products integrated in DOIF are designed to synthesize multidisciplinary data relevant to the essential environmental variables that are of major interests in ocean and sea state monitoring and ecosystem health. These standardized products of statistical analysis, forecasting and other specialized information mainly including:

- basic marine geography products (seabed topography);
- marine environment products (sea surface temperature, waves, currents, tides, wind field);
- marine disaster numerical forecast products (typhoon, waves, storm surges, tsunamis, sea ice, sea fog, red tide, oil spills);
- air-sea interaction process forecasting products (long-term forecasts of El Nino and La Nina events, long-term prediction of sea level rise);
- sea-land interaction prediction products (coastal erosion, estuarine terrain silting, and land reclamation).

2.4 China Digital Ocean Prototype System (CDOPS)

With the support of high-performance computers and advanced visualization device, realizing holographic digital reproduction and prediction of seafloor, water, sea surface and coast, and the visualization of ocean processes and phenomena, is one of the objectives of China Digital Ocean. Thus the 3D visualization, virtual reality and simulation, interoperable technology are all in the scope of DOIF.

For meeting the needs of marine environment and disaster prediction, forecasting and early warning, maritime interests safeguard, and marine resource survey,

management and development, China Digital Ocean Prototype System (Zhang et al., 2011), a unique portal interconnecting the interoperable node platforms, was developed as an application system of DOIF. All the functions of DOIF can be realized by CDOPS in an on-line (internet) manner. Initially, CDOPS was developed for the purpose of integrating, managing, displaying, as well as disseminating marine data and metadata within China (Deng et al. 2013). Large and diverse ocean datasets deriving from marine in-situ monitoring, surveillance, investigation, and operational observation, are integrated into the digital ocean databases with standardized formats and quality. The on-line access to in-situ data, metadata and products is provided. It is also a marine information service platform aiming at disseminating the common knowledge about ocean and sea to the public. CDOPS is an advanced 3D visualization system, allowing users to search, browse, analyze and manage the ocean data and information that have been integrated into CDOPS. Currently, Decision Making Oriented Models such as marine environmental assessment and analysis model, marine disaster assessment and prevention model, marine resources analysis, evaluation and utilization model, etc., are being developed and will be incorporated into CDOPS in the future.

3 The future vision of DOIF in the international ocean cooperation

According to the National Marine Development Strategy, DOIF is no longer just a scientific research program or pilot project. It is an operational system which is anticipated to provide practical service at national level, with the emphasis on integrated ocean management. For a long time in the future, advanced technology together with effectiveness and reliability is the objectives it will pursue.

In the meantime, DOIF attaches great importance to the international data exchange and scientific and technological cooperation. A Regional Ocean Visualization Subsystem (ROVS) will be developed to serve as a capacity building activity in ocean data and information management and service in the Western Pacific region (WEATPAC). This subsystem will be built on the basis of existing CDOPS. As a step forward to facilitate the collaboration and cooperation among countries in the Western Pacific region, it will provide a 3D globe visualization system for integrating, managing and displaying marine data and information through IODE Ocean Data and Information Network for the Western Pacific Region (ODINWESTPAC) (Yu et al., 2014).

ROVS is designed as a GIS (Geographic Information System)-based 3D globe visualization platform, accompanied by a menu bar on the side. The globe is used for visualization and the menu bar provides functions of data/information searching, indexing

and browsing. Oceanographic, meteorological, biological, and chemical data that have geographic information/spatial coordinates observations from moored buoys, tidal stations, Argos, drifters, ships, and satellites, can be integrated/uploaded into this system. Moreover, some information without spatial coordinates such as marine experts, marine libraries, national and regional marine projects will also be included.

As the coordinator of ODINWESTPAC, National Marine Data and Information Service will be responsible for system maintenance and data management. Member states of IOC/WESTPAC will have the authority to upload their own data and information onto ROVS. In turn, users will be able to access to those loaded data either in a visual (figure or animation) or a numeric (text or table) way. All the data and information products including figures and animations generated by ROVS can be freely download.

We believe that aiming at serving the urgent needs for marine data, information and products, ROVS will be a platform for promoting the cooperation in data collecting, processing, management and service at regional level.

4 Discussion and summary

With people's gradually awakening consciousness on the importance of marine utilization and protection, the public demand for ocean related data and information is in the fast growth. However, we must realize that the current level of marine information technology is relatively low nowadays. There is a long way to go for us in many areas of marine resource management, scientific endeavor and industry practices. China is eager to learn from the world leaders of ocean management through international cooperation. Domestically, with the implementation of long-term strategy of DOIF, we try to demonstrate our determination and on-going effort by implementing a coherent, strategic planning and management framework capable of dealing with the complex issues confronting the sustainable development of our oceans. Chinese marine programs will definitely enjoy I greater development. The key to the success of DOIF is the presence of CDOPS, which is capable of delivering real-time, delayed-mode, and historical data for in-situ and remotely-sensed physical, chemical and biological observations, as well as, model-generated outputs, including forecasts, to users and capable of delivering all forms of information to and from secure archive facilities.

The construction of DOIF must follow the needs of National Marine Development Strategy. Through continuously integrating all kinds of marine basic data, extending information content, expanding outreach services, the goal is gradually achieved, including the multidimensional dynamic digital marine technology systems and application systems

that cover Chinese domestic water, territorial waters, contiguous zone, exclusive economic zone, continental shelf, open oceans and polar oceans. The comprehensive services provided by DOIF include the aspects of marine scientific decision-making, rapid emergency response, marine economy development, marine resources utilization, marine ecology and environment protection, maritime rights and interests safeguarding, et al.

At present, DOIF of China is still in its infancy stage. For the healthy, sustainable and stable development of DOIF, we need to make efforts in the following aspects. First, with the continuously growing amount of information and improvement of DOIF's functions, software and hardware facilities and other infrastructure need to be maintained and updated, and security measures need to be strengthened, to ensure the robustness and efficiency of system operation and protect security of national digital information. Second, the its development requires a sound organizational structure. Coordination by the government and cooperation between stakeholders are in much need. Third, DOIF is a highly syntheses of oceanography, marine-meteorology, geography, space science, computer science and information technology. It involves the cutting edge science and technology which are advancing with each passing day. Thus in the process of implementing CODF, we must keep track of the progress of science and technology in related fields domestic and abroad. Cultivation of high-level intelligent and personnel knowledge structure optimization and quick updates will be crucial.

The principle of integrated management and sustainable development runs through the DOIF. A healthy and productive marine environment obviously benefits all the countries that make a living from its resources. Support from agencies and institutes who contribute data, information, ideas and techniques will greatly promote the healthy development of the Western Pacific Ocean. Thus, the future of DOIF will also focus on its role in the regional ocean cooperation in the Western Pacific. DOIF is planning to serve as a capacity building platform in ocean data, metadata, product and information management and service, for promoting the cooperation among WESTPAC member/member states as well as the collaboration with other international data projects.

Acknowledgements

Digital Ocean Information Framework is supported by Chinese 908 Program. We would like to record our appreciation of the constructive contributions that have been made by all members of the Research Team of the China Digital Ocean Prototype System in the past years. We are very grateful for the encouragement and suggestions from our colleagues Prof. Lin Shaohua, Dr. Jiang Xiaoyi and Ms. Qi Dongmei.

References

[1] Deng Zengan, Ting Yu, Xiaoyi Jiang, Suixiang Shi, Jiye Jin, Linchong Kang and Feng Zhang, 2013: Bohai Sea oil spill model: a numerical case study, Marine Geophysical Research. 34: 115-125. DOI 10.1007/s11001-013-9180-x

[2] National Marine Data and Information Service, 2011: Technical report of China Digital Ocean Information Framework.

[3] Liu Jin, Jiang Xiaoyi, and Li Sihai, 2009: Research on the model building of water and 3d-dimensional visualization in Digital Ocean, Marine Science Bulletin, 2009-04

[4] Wang Xiaomin, Zhang Xin, Chi Tianhe, 2008: Digital ocean oriented data processing and information service systems Control Conference, CCC 2008. 27th, 653 – 656.

[5] Zhang Xin, Wen Dong, Sihai Li, Jiancheng Luo & Tianhe Chi 2011: China Digital Ocean Prototype System, International Journal of Digital Earth, 4:3, 211-222. DOI: 10.1080/17538947.2010.512367

[6] Yu Ting, Qi Dongmei, Chen Manchun, and Deng Zengan, 2014: The vision of China Digital Ocean under the framework of Marine Climate Data System (MCDS). Marine Science Bulletin, 2014, 33(Sup. 1), 51-55.]

中国数字海洋信息框架在国际海洋合作中的应用

于 婷[1,3], 邓增安[1,2], 石绥祥[1,2]

（1. 国家海洋信息中心，天津 300171；2. 国家海洋局 数字海洋重点实验室，天津 300171；
3. 中国海洋大学, 山东 青岛 266100）

摘 要：中国已于 2011 年，在“我国近海海洋综合调查与评价”专项的基础上，建立了数字海洋信息基础框架（DOIF）。本文系统介绍了能够集成管理所有观测数据的 DOIF。DOIF 可以为中国沿海海洋资源可持续管理提供决策支持，为中国近海综合管理提供有效信息、附加价值产品和服务，服务对象覆盖政府部门和私营团体（例如：海洋管理人员、渔民、航运公司等），最后，还展望了 DOIF 在西太区域国际海洋数据和信息服务领域的应用前景。

关键词：中国数字海洋，海洋观测系统，综合数据管理，决策

Marine Science Bulletin

Marine Science Bulletin publishes papers on marine science and technology including physical oceanography, chemical oceanography, marine biology, marine geology, environmental oceanography, estuarine & coastal sciences, marine technology, digital ocean, coastal zone management, ocean engineering, marine economics, etc., and aims to promote international academic exchange.

Editor-in-Chief: SHI Sui-xiang (石绥祥)
Associate Editor-in-Chief: XIANG Wen-xi (相文玺) XUE Hui-feng (薛惠芬)
Executive Editor: QIU Wen-jing (邱文静) DONG Yi (董 艺) LI Xiao-guang (李晓光)
YUAN Ze-yi (袁泽轶)
English proofed by: WANG Qi (王 琦)

Semi-annually (started in 1999, sum 33)
Publication date: May 15th and Oct. 15th

Marine Science Bulletin **(Vol. 17, No. 1, May 2015)**

Responsible Institution:
State Oceanic Administration of China
Sponsored by:
National Marine Data and Information Service
Edited by:
Office of Marine Science Bulletin (English edition)
Printed by:
Printery of National Marine Date and Information Service

Published by:
Office of Marine Science Bulletin (English edition)
E-mail: msb@mail.nmdis.gov.cn
Tel: (022) 24011287
Address: 93 Liuwei Rd., Hedong District, Tianjin 300171, China

---

ISSN1000-9620
CN12-1271/N

Price: $ 30.00 / ￥40.00 Per year